SURFACE-INITIATED RING-OPENING METATHESIS POLYMERIZATION: A VERSATILE ROUTE TO PRODUCE NOVEL MATERIALS AND BIOMIMETIC COATINGS

By

Carlos Andres Escobar

Dissertation
Submitted to the Faculty of the
Graduate School of Vanderbilt University
in partial fulfillment of the requirements
for the degree of

DOCTOR OF PHILOSOPHY
in
Chemical Engineering

May, 2014
Nashville, Tennessee

Approved:
Professor G. Kane Jennings
Professor Scott A. Guelcher
Professor Eva Harth
Professor Paul E. Laibinis

To Silvia, Shebis, and our beloved families.

ACKNOWLEDGMENTS

Ever since my graduation from college, I always dreamt of becoming a Ph.D. in Chemical Engineering. I thank you God for blessing me with such an opportunity. I could not have asked for a better role model, advisor, and mentor to guide me through this journey: thank you Professor Kane Jennings! I am proud and honored to work for a person with such great intellectual capabilities and personal integrity. I appreciate your non-stop “beating”, continuous advice, support, patience, and friendship, not only on academic and professional issues, but also on personal matters. I want to express my deepest gratitude and respect for the members of my committee: Dr. Paul Laibinis, Dr. Scott Guelcher, and Dr. Eva Harth. Their insight, advice, and guidance greatly strengthened my research work and experience.

The privilege of becoming part of the Jennings Lab was a truly rewarding experience. Support, advice, guidance, and friendship, above all, were the common denominators of Dr. Christopher Faulkner, Dr. Peter Ciesielski, Dr. Brandon Booth, Dr. Juan Tuberquia, Dr. Steven Vilt, Darlene Gunther, Siyuan Yang, and Jarrid Ristau. Thank you all for your willingness to share your thoughts, ideas, and helpful discussions. I also had the privilege to work with enthusiastic, intelligent, and hard-working undergraduate students, including: Noel Zulklifli, Matthew Spellings, Kathryn Maxwell, Bella Mahfuz, and Tyler Cooksey. I greatly appreciate their valuable ideas and contributions to this research work.

I thank all the faculty members in the Chemical and Biomolecular Engineering Department for sharing their experience and knowledge. I learned so much from them. I appreciate Dr. Bridget Rogers and Dr. Robert Harl for the use of the ellipsometer and their insight with respect to x-ray photoelectron spectroscopy and Rutherford backscattering spectrometry, and Dr. Rizia Bardhan for the use of the glove box. I appreciate all the generous help offered by Mary Gilleran and Rae Uson regarding administrative and non-administrative matters, and that of Mark Holmes in mechanical ones.

I want to thank other Vanderbilt community members for their help during this research: Dr. Jonathan Ertelt for providing the superhydrophobic leaves used in this work, Dr. Jonathan Jarvis for providing the diamond pyramid field emitter arrays, Dr. Sharon Weiss and Dr. Yang Jiao for providing the Klarite substrates, Dr. Jennifer Gaddy for sharing her “fixing protocol”, Dr. David Cliffel for the use of the optical microscope, the VINSE personnel for enabling me to use its facilities, and Robin Midget for bringing the evaporator “back to life” one more than time and his invaluable insight on how to fix it.

I am grateful about all the good friends I have met during my stay in Nashville, they have made Silvia, Shebis, and I feel as if we were surrounded by our own family. Special thanks to Juan, Angela, JuaniS, Margarita, Jason, Stijn, Rob, and Neil.

I have a special appreciation for the Mejía González family for being there when most need, and for keeping an eye on us. We definitely enjoyed all of your visits to Nashville. Education is the best legacy that any parents can offer to their off-springs, or so believe mine. By setting their own sheer example of academic achievement, no matter how old you are, they have shown my sister and me that one can always reach farther as long as one is willing to do so. For all your love, support, and advice I thank you very much. I am most grateful to my wife Silvia, who has continuously and tirelessly taken care of Shebis and me. I greatly appreciate your unconditional love, support, patience, and advice. Both your eyes and smile, along with those of Shebis’, are my greatest inspiration.

Finally, I would like to thank the U.S. Department of Energy and the National Science Foundation for the funding support of this research by grants ER46239 and CBET-1134509, respectively.

TABLE OF CONTENTS

Page

Chapter

Appendix

LIST OF TABLES

LIST OF FIGURES

LIST OF SCHEMES

CHAPTER I

INTRODUCTION

Engineering the interfacial properties of materials and surfaces plays a key role in numerous research areas of science and technology, including microelectronics,[1] tribology,[2] separations,[3] solar energy conversion,[4] and coatings.[5] In these and other fields, adaptability is the common denominator and the driving force behind such fine-tuning. In other words, the modification or functionalization of substrates serves the purpose of making them fit for a specific application. For instance, the functionalization of the surface of a membrane could either minimize undesired interactions, which may reduce performance (e.g., membrane fouling), or introduce additional interactions to improve selectivity. Another example is that of forming films exhibiting ultralow surface energy on the surface of substrates to change their wettability characteristics or provide protection. In connection with the latter example, fluorinated materials, namely partially fluorinated ones, experience great commercial demand.[6] By contrast to fully fluorinated materials, partial fluorination offers advantages in terms of cost and synthetic flexibility, and in some cases, performance.[7]

Among several film-deposition methods, a surface-initiated polymerization (SIP) represents a versatile approach to grow polymer films.[8] SIP techniques, also known as “grafting from” methods, foster the growth of surface-bound polymer films directly from initiator groups that are chemically coupled to a self-assembled monolayer (SAM).[8] A SAM is a highly ordered, single-molecule thick film that fundamentally alters the properties of a surface and is created by the spontaneous adsorption of molecular constituents from solution onto an appropriate substrate.[9] SIP takes advantage of the salient benefits provided by SAMs, including chemical diversity regarding “anchor groups” and “functional groups”, and the ability to vary the chain length of the adsorbates, which translates into control over film length scales, usually in the range of 2 – 30 Å.[10,11] In addition, SIP offers excellent control over film thickness and chemical composition as different types of monomers are amenable to polymerization by these methods.[8,12,13] Common examples of self-assembly and SIP applications include formation of monolayer films on metallic and non-metallic substrates, preparation of polymer brushes and block copolymers, and functionalization of nanoparticles.[10,14-17] By contrast to traditional film-deposition methods such as spin-coating or dip-coating, SIP provides a chemical interaction between the polymer and the surface, which translates into more robust coatings.[13]

Although SIP techniques have been frequently employed to modify the surface properties of a wide variety of planar and non-planar substrates,[8,18] investigations reporting their use as versatile techniques for modifying internal porosity or creating microtextured coatings are scarce. The former would impact membrane processing, and the latter would enable straightforward fabrication of superhydrophobic coatings. While methods do exist to produce superhydrophobic, rough surfaces, such processes often imply multiple elaborate steps.[19,20] By contrast, SIP methods involve minimal processing steps. Surface-initiated atom-transfer radical polymerization (SI-ATRP) has been the prevalent technique for the surface functionalization of porous architectures and supports, mainly because of the commercial availability of a large variety of functional monomers and its highly controllable polymerization nature.[3,21] However, there is an alternate surface-initiated technique to modify such porous structures, referred to as surface-initiated ring-opening metathesis polymerization (SI-ROMP),[22-24] that has received less treatment in literature regarding this application in spite of exhibiting desirable advantages such as faster polymerization rates, even at room temperature in ambient conditions, tolerance toward functional groups, preparation of high molecular weight polymers, and preservation of the olefin functionality in the resulting polymer.[22,23,25,26] A vast chemical diversity of monomers has been successfully polymerized using ROMP, including norbornenes, azonorbornenes, cyclooctenes, and cyclooctadienes.[22,24,27] In a similar manner to other SIP approaches, SI-ROMP has been performed on several substrates (Au, Si, SiO_2/Si, and cellulose fibers) as well as on many surface topographies.[1,22,25,28] Examples of the versatility and flexibility provided by this technique include the modification of micrometer-sized silica particles for chromatographic applications by Buchmeiser et al.,[25] the functionalization of nanostructures by SI-ROMP as described by Liu et al. and Watson et al.,[29,30] the fabrication of a polymer dielectric layer exhibiting low capacitance (3 $nF \cdot cm^{-2}$) and a thickness of 1200 nm by Rutenberg et al.,[1] and the formation of partially fluorinated films with exceptional low critical surface tensions (9 – 18 $mN \cdot m^{-1}$) on gold substrates by Faulkner et al.[31]

This dissertation describes the fabrication and characterization of new materials and interfaces by employing SI-ROMP to grow partially fluorinated coatings, prepared from 5-(perfluoro-n-alkyl)norbornenes (NBFn), where n represents the number of carbon atoms present in the fluorocarbon side chain, e.g., 4, 6, 8, and 10, with critical surface tensions as low as 9 mN/m to (1) alter nanoporous materials, (2) create thick and robust coatings, and (3) produce microtextured coatings that exhibit superhydrophobicity. Although SIP methods have been used by others[3,32] and us[31,33] for the deposition of partially fluorinated films, the ability to grow these films with thicknesses above a few micrometers with controlled textures or within nanoporous materials has not been demonstrated prior to this work.

The first aspect of my research, described in Chapter IV, advances the interfacial polymer chemistry to prepare uniquely layered membranes. This work investigates the use of SI-ROMP to produce fluorocarbon-containing polymer films that grow within, throughout, and between nanoporous materials, and to study the influence of polymerization time and sulfonation levels of the polymer backbone on wettability and the transport of simple ions. For example, I use surface chemistry (thiols and silanes) in conjunction with the SI-ROMP of 5-(perfluorohexyl)norbornene to fabricate composite fluorocarbon membranes that exhibit high resistance to the transport of ions, as measured by electrochemical impedance spectroscopy (EIS). EIS measurements also show that ion transport through the composite membrane is substantially enhanced after sulfonation. In addition, the fluorinated nature of the polymer film renders the membrane selective toward ions with similar chemical properties. Assessing the surface properties with water and hexadecane contact angle measurements shows that the surface of the membrane is both highly hydrophobic and oleophobic, consistent with a predominant perfluoromethyl surface composition.

Chapter V describes the fabrication of protective coatings with enhanced thicknesses and barrier properties. Fluorinated and partially fluorinated polymers attract great technological interest because of their unique physicochemical properties, including excellent chemical resistance, high thermal stability, repellence towards water and oils, superior outdoor durability, and exceptional mechanical and thermal properties.[34] Therefore, the ability to combine the many practical benefits of SIP with new approaches to enable the routine production of coatings with thickness greater than 1 μm could have a profound impact in the area of specialty coatings. To this end, I have combined two versatile SIP techniques, namely, surface-initiated atom-transfer polymerization (SI-ATRP) and SI-ROMP, in the preparation of exceptionally thick, partially fluorinated polymer films prepared from NBFn monomers. SI-ATRP is used to grow a macroinitiator and SI-ROMP to produce the final coating. I investigated the effect of side chain length, polymerization time, monomer concentration, and temperature on the kinetics of film growth. Furthermore, by tuning the type of chemistry employed, the growth of such films can be extended to a wide variety of substrates. Results show that this polymerization approach promotes the growth of thick, dense partially fluorinated coatings that are highly hydrophobic and oleophobic. Remarkably, the growth rate and the resistance against ion transport of these coatings are among the fastest and highest, respectively, ever reported for SIP films.

The third aspect of my research, which focuses on the development of a versatile replication process termed micromolding surface-initiated polymerization (μMSIP), is described in Chapters VI and VII. Chapter VI provides a detailed description of the process, including its advantages and limitations, which in principle, is used to reproduce the surface topography of synthetic substrates onto solid supports. Briefly, μMSIP consists of molding the structure of target surfaces with hard polydimethylsiloxane (h-PDMS), filling such a mold with pure (neat) monomer and subsequently exposing it to a SI-ROMP-active substrate to perform a confined polymerization, which results in polymer growth that conforms to the features in the h-PDMS mold. μMSIP enables the formation of polymer films exhibiting either high-relief or recessed topographies. I investigated the effect of initiation approach, e.g., monolayer or macroinitiator, on the height (monomer conversion) of the resulting surface features. I also examined the effect of other process variables, such as polymerization time and temperature, on the final height of the features. SEM and AFM characterization shows that the resulting films are uniform in quality and exhibit homogeneous surface structures across large areas. Furthermore, μMSIP allows the modulation or fine-tuning of the height of the final polymer surface features and facilitates the preparation of generationally textured films.

Recently, nature and its remarkable designs have provided endless sources of inspiration for researchers who are seeking ideas to address specific challenges. Accordingly, in Chapter VII I extend the use of μMSIP to fabricate surface-bound polymer coatings that reproduce the surface topography of superhydrophobic leaves onto solid supports. Replication of such highly evolved and functional surface architectures offers many potential applications including self-cleaning surfaces,[35-37] corrosion resistance,[38-40] water repellency,[19,41,42] and drag reduction.[43] This approach provides versatility in that it introduces a wide variety of chemical compositions available in materials chemistry, including partially fluorinated polymers with ultralow critical surface tensions. The novelty of this technique as compared to other replication techniques in the family of soft lithography is that μMSIP produces robust, microtextured polymeric coatings bound to a solid surface. μMSIP aims at producing novel biomimetic coatings that stabilize the superhydrophobic state to impact a wide variety of applications.

Finally, Chapter VIII summarizes the major findings of this research work and proposes future work regarding the possible SI-ROMP of ionic liquids for the production of membrane materials and the use of μMSIP to achieve superoleophobic surfaces.

References

(1) Rutenberg, I. M.; Scherman, O. A.; Grubbs, R. H.; Jiang, W.; Garfunkel, E.; Bao, Z. Synthesis of Polymer Dielectric Layers for Organic Thin Film Transistors via Surface-Initiated Ring-Opening Metathesis Polymerization. *J. Am. Chem. Soc.* **2004,** 126, 4062-4063.

(2) Booth, B. D.; Vilt, S. G.; Lewis, J. B.; Rivera, J. L.; Buehler, E. A.; McCabe, C.; Jennings, G. K. Tribological Durability of Silane Monolayers on Silicon. *Langmuir* **2011,** 27, 5909-5917.

(3) Balachandra, A. M.; Baker, G. L.; Bruening, M. L. Preparation of Composite Membranes by Atom Transfer Radical Polymerization Initiated from a Porous Support. *J. Membr. Sci.* **2003,** 227, 1-14.

(4) Ciesielski, P. N.; Scott, A. M.; Faulkner, C. J.; Berron, B. J.; Cliffel, D. E.; Jennings, G. K. Functionalized Nanoporous Gold Leaf Electrode Films for the Immobilization of Photosystem I. *ACS Nano* **2008,** 2, 2465-2472.

(5) Lee, S.-W.; Laibinis, P. E. Protein-Resistant Coatings for Glass and Metal Oxide Surfaces Derived from Oligo(ethylene glycol)-Terminated Alkyltrichlorosilanes. *Biomaterials* **1998,** 19, 1669-1675.

(6) Steed, J. M. *U.S. Fluorocabon Industry Economic Analysis*, www.alliancepolicy.org, 2013.

(7) David, W. G.; Charlie, W. S. Fluorinated Coatings and Films: Motivation and Significance. In *Fluorinated Surfaces, Coatings, and Films*; American Chemical Society: **2001**; Vol. 787, p 1-14.

(8) Jennings, G. K.; Brantley, E. L. Physicochemical Properties of Surface-Initiated Polymer Films in the Modification and Processing of Materials. *Adv. Mater.* **2004,** 16, 1983-1994.

(9) Porter, M. D.; Bright, T. B.; Allara, D. L.; Chidsey, C. E. D. Spontaneously Organized Molecular Assemblies. 4. Structural Characterization of Normal-Alkyl Thiol Monolayers on Gold by Optical Ellipsometry, Infrared-Spectroscopy, and Electrochemistry. *Journal of the American Chemical Society* **1987,** 109, 3559-3568.

(10) Bain, C. D.; Troughton, E. B.; Tao, Y. T.; Evall, J.; Whitesides, G. M.; Nuzzo, R. G. Formation of Monolayer Films by the Spontaneous Assembly of Organic Thiols from Solution onto Gold. *J. Am. Chem. Soc.* **1989,** 111, 321-335.

(11) Witucki, G. L. A Silane Primer - Chemistry and Applications of Alkoxysilanes. *Journal of Coatings Technology* **1993,** 65, 57-60.

(12) Advincula, R. Polymer Brushes by Anionic and Cationic Surface-Initiated Polymerization (SIP). In *Surface-Initiated Polymerization I*; Jordan, R., Ed. **2006**; Vol. 197, p 107-136.

(13) Bhat, R. R.; Tomlinson, M. R.; Wu, T.; Genzer, J. Surface-Grafted Polymer Gradients: Formation, Characterization, and Applications. *Surface- Initiated Polymerization II* **2006,** 198, 51-124.

(14) Brzoska, J. B.; Azouz, I. B.; Rondelez, F. Silanization of Solid Substrates: A Step Toward Reproducibility. *Langmuir* **1994,** 10, 4367-4373.

(15) Ayres, N. Polymer Brushes: Applications in Biomaterials and Nanotechnology. *Polym. Chem.* **2010,** 1, 769-777.

(16) Neoh, K. G.; Kang, E. T. Functionalization of Inorganic Nanoparticles with Polymers for Stealth Biomedical Applications. *Polymer Chemistry* **2011,** 2, 747-759.

(17) Barbey, R.; Lavanant, L.; Paripovic, D.; Schüwer, N.; Sugnaux, C.; Tugulu, S.; Klok, H.-A. Polymer Brushes via Surface-Initiated Controlled Radical Polymerization: Synthesis, Characterization, Properties, and Applications. *Chem. Rev.* **2009,** 109, 5437-5527.

(18) Kaufmann, T.; Ravoo, B. J. Stamps, Inks and Substrates: Polymers in Microcontact Printing. *Polymer Chemistry* **2010,** 1, 371-387.

(19) Lee, Y.; Park, S. H.; Kim, K. B.; Lee, J. K. Fabrication of Hierarchical Structures on a Polymer Surface to Mimic Natural Superhydrophobic Surfaces. *Advanced Materials* **2007,** 19, 2330-2335.

(20) Zhu, L.; Xiu, Y.; Xu, J.; Tamirisa, P. A.; Hess, D. W.; Wong, C.-P. Superhydrophobicity on Two-Tier Rough Surfaces Fabricated by Controlled Growth of Aligned Carbon Nanotube Arrays Coated with Fluorocarbon. *Langmuir* **2005,** 21, 11208-11212.

(21) Ulbricht, M. Advanced Functional Polymer Membranes. *Polymer* **2006,** 47, 2217-2262.

(22) Leitgeb, A.; Wappel, J.; Slugovc, C. The ROMP Toolbox Upgraded. *Polymer* **2010,** 51, 2927-2946.

(23) Bielawski, C. W.; Grubbs, R. H. Living Ring-Opening Metathesis Polymerization. *Prog. Polym. Sci.* **2007,** 32, 1-29.

(24) Slugovc, C. The Ring Opening Metathesis Polymerisation Toolbox. *Macromol. Rapid Commun.* **2004,** 25, 1283-1297.

(25) Buchmeiser, M. R. Metathesis Polymerization to and from Surfaces. In *Surface-Initiated Polymerization I*; Jordan, R., Ed.; Springer-Verlag Berlin: Berlin, **2006**; Vol. 197, p 137-171.

(26) Sutthasupa, S.; Shiotsuki, M.; Sanda, F. Recent Advances in Ring-Opening Metathesis Polymerization, and Application to Synthesis of Functional Materials. *Polym. J.* **2010,** 42, 905-915.

(27) Lerum, M. F. Z.; Chen, W. Surface-Initiated Ring-Opening Metathesis Polymerization in the Vapor Phase: An Efficient Method for Grafting Cyclic Olefins with Low Strain Energies. *Langmuir* **2011,** 27, 5403-5409.

(28) Carlsson, L.; Malmstrom, E.; Carlmark, A. Surface-Initiated Ring-Opening Metathesis Polymerisation from Cellulose Fibres. *Polym. Chem.* **2012,** 3, 727-733.

(29) Liu, X.; Basu, A. Olefin Metathesis on Nanostructures. *Journal of Organometallic Chemistry* **2006,** 691, 5148-5154.

(30) Watson, K. J.; Zhu, J.; Nguyen, S. T.; Mirkin, C. A. Hybrid Nanoparticles with Block Copolymer Shell Structures. *Journal of the American Chemical Society* **1998,** 121, 462-463.

(31) Faulkner, C. J.; Fischer, R. E.; Jennings, G. K. Surface-Initiated Polymerization of 5-(Perfluoro-n-alkyl)norbornenes from Gold Substrates. *Macromolecules* **2010,** 43, 1203-1209.

(32) Ye, Q.; Wang, X.; Li, S.; Zhou, F. Surface-Initiated Ring-Opening Metathesis Polymerization of Pentadecafluorooctyl-5-norbornene-2-carboxylate from Variable Substrates Modified with Sticky Biomimic Initiator. *Macromolecules* **2010,** 43, 5554-5560.

(33) Brantley, E. L.; Jennings, G. K. Fluorinated Polymer Films from Acylation of ATRP Surface-Initiated Poly(hydroxyethyl methacrylate). *Macromolecules* **2004,** 37, 1476-1483.

(34) Hansen, N. M. L.; Jankova, K.; Hvilsted, S. Fluoropolymer Materials and Architectures Prepared by Controlled Radical Polymerizations. *Eur. Polym. J.* **2007,** 43, 255-293.

(35) Furstner, R.; Barthlott, W.; Neinhuis, C.; Walzel, P. Wetting and Self-Cleaning Properties of Artificial Superhydrophobic Surfaces. *Langmuir* **2005,** 21, 956-961.

(36) Wu, Z.; Xu, Q.; Wang, J.; Ma, J. Preparation of Large Area Double-walled Carbon Nanotube Macro-films with Self-cleaning Properties. *Journal of Materials Science & Technology* **2009,** 26, 20-26.

(37) Barthlott, W.; Neinhuis, C. Purity of the Sacred Lotus, or Escape from Contamination in Biological Surfaces *Planta* **1997,** 202, 1-8.

(38) Tuberquia, J. C.; Nizamidin, N.; Jennings, G. K. Effect of Superhydrophobicity on the Barrier Properties of Polymethylene Films. *Langmuir* **2010,** 26, 14039-14046.

(39) Liu, T.; Chen, S.; Cheng, S.; Tian, J.; Chang, X.; Yin, Y. Corrosion Behavior of Super-Hydrophobic Surface on Copper in Seawater. *Electrochimica Acta* **2007,** 52, 8003-8007.

(40) Zhang, F.; Zhao, L.; Chen, H.; Xu, S.; Evans, D. G.; Duan, X. Corrosion Resistance of Superhydrophobic Layered Double Hydroxide Films on Aluminum. **2008,** 47, 2466-2469.

(41) Lee, S.-M.; Lee, H. S.; Kim, D. S.; Kwon, T. H. Fabrication of Hydrophobic Films Replicated from Plant Leaves in Nature. *Surface and Coatings Technology* **2006,** 201, 553-559.

(42) Sun, M. H.; Luo, C. X.; Xu, L. P.; Ji, H.; Qi, O. Y.; Yu, D. P.; Chen, Y. Artificial Lotus Leaf by Nanocasting. *Langmuir* **2005,** 21, 8978-8981.

(43) Rothstein, J. P. Slip on Superhydrophobic Surfaces. *Annual Review of Fluid Mechanics* **2010,** 42, 89-109.

CHAPTER II

BACKGROUND

Surface-Initiated Polymerization (SIP)

Long-established film-deposition methods such as dip-coating and spin-casting create physisorbed polymer films that exhibit non-covalent interactions (van der Waals forces or hydrogen bonding) with the surface.[1,2] Such weak adhesion limits the performance of the films and renders them unstable against external factors such as solvents, high temperatures, and mechanical forces.[1,3] To surmount this deficiency, it is essential to establish a chemical bond between the polymer and the surface.[1-4] A versatile route to do so is to use a surface-initiated polymerization (SIP). By contrast to traditional methods, an SIP offers the capability of tailoring the surface properties of solid substrates while exhibiting various advantages, including chemical coupling between the surface and the polymer chains, conformal and uniform coating of surfaces exhibiting planar and non-planar architectures, and effective control over composition, film thickness, and grafting density.[2] These practical benefits have allowed SIP to functionalize or modify fine particles,[1,5] porous supports,[6,7] and a wide variety of substrates, including organic polymers, silicon oxide, alumina, and gold.[4,7,8] In order to be functional, SIP requires the immobilization of an initiating species onto the surface before polymerization, which is usually attained by self-assembly techniques.[1,9] Subsequent exposure of the activated substrate to an appropriate monomer solution promotes polymerization directly from the surface.[10] There are many classes of SIP, as defined by their reaction mechanism for propagation,[2] including surface-initiated ring-opening polymerization (SI-ROMP),[11] surface-initiated atom-transfer radical polymerization (SI-ATRP),[9] radical polymerization,[12] anionic polymerization,[10] cationic polymerization,[10] and ring-opening polymerization (ROP).[13]

Surface-Initiated Ring-Opening Metathesis Polymerization

Intense research has established SI-ROMP as a useful and versatile technique for synthesizing polymers with tunable molecular weights, shapes, and functionalities[11,14,15] with attractive biological, electronic, and mechanical properties.[14,16,17] SI-ROMP is a chain growth polymerization, its reaction mechanism is based on olefin metathesis (metal-mediated carbon-carbon double bond exchange process), and the thermodynamic driving force of the system is the relief of ring strain.[5,11,15,16] Initiation occurs when a metal alkylidene complex (initiator) coordinates with the double bond of a cyclic olefin. Subsequent [2 + 2]-cycloaddition generates a metallacyclobutane intermediate, which forms a growing polymer chain.[14] Such an intermediate undergoes a cycloreversion reaction to generate a new metal alkylidene.[16] The propagation stage comprises the repetition of the above mention steps until polymerization ceases, i.e., no monomer is left, a reaction equilibrium is reached, or termination reactions occur.[14] Common monomers used in SI-ROMP are cyclic olefins exhibiting appreciable strain energy (>5 kcal/mol) such as cyclobutene, cyclopentene, and norbornene, including its functional derivatives.[11,14,15] Examples of termination reactions include intermolecular chain-transfer and intramolecular chain-transfer (also known as “backbiting”).[11,14] In the former, the active end of a growing polymer chain can react with a double bond of a different polymer chain. In the latter, the active initiator located at the terminus of the chain reacts with itself to produce a cyclic species and a polymer chain of reduced molecular weight.[16] Chain transfer reactions constitute a shortcoming in the polymerization of monomers with lower energy strain.[15] Recently, Lerum et al.,[18] reported a vapor-phase ROMP approach to polymerize cyclic olefins with low strain energies. By adopting such an approach, they were able to suppress chain transfer reactions at the vapor-solid interface, and therefore, achieve an enhancement in polymerization. The study showed that a minimal strain energy of 2.2 kcal/mol is necessary to achieve polymerization of these monomers. The development of well-defined ruthenium-based catalysts has fostered ROMP.[19,20] Although catalysts based on other transition metals such as molybdenum, titanium, tantalum, and tungsten have proven to be useful for ROMP, each one having its own advantages and disadvantages, ruthenium catalysts exhibit particular properties such as thermal stability, high activity, and tolerance toward polar functional groups that render them more attractive for ROMP.[14,16,18] SI-ROMP has been used to functionalize several substrates including Au,[17,21,22] SiO_2/Si,[23,24] alumina,[7] and carbon paper.[25]

Fluorinated and Partially Fluorinated Polymer films

In general, fluropolymers are attractive and versatile materials as a consequence of their unique, relevant physicochemical properties, including low critical surface energy, chemical inertness, low dielectric constant, low flammability, low refractive index, and weather resistance.[26] Such exclusive properties are attributed to the C-F bonding, which exhibits weak intermolecular forces, low reactivity, low surface free energy, and a large bonding energy.[27] Consequently, these materials have been applied as protective paints and coatings,[26,28,29] in membrane separations,[6,7] as hydrophobic surfaces,[21,30], and in microelectronics.[26,31] Furthermore, a recent economic analysis of the fluorocarbon industry in the United States estimated that the market segment corresponding to fluoropolymers is worth $ 2.72 billion.[32]

In spite of their advantages, fluoropolymers exhibit certain limitations that undermine their widespread use, namely high expense and difficult processing problems (e.g., poor solubility, not easily cured, high temperatures).[26,27] Perfluoropolymers, those comprised solely of carbon and fluorine, e.g., polytetrafluoroethylene (PTFE), specifically, bear these shortcomings. To circumvent these issues, scientists have resorted to partially fluorinated polymers. Unlike their all-fluorocarbon counterparts, partially fluorinated materials offer advantages in terms of cost and synthetic flexibility, and in some cases, performance.[26,27,33] In connection with the latter, fluorinated species tend to segregate from other chemical species, and if allowed, usually migrate or partition to the air-film interface, thus yielding ultralow surface energy surfaces.[27,33] For example, the critical surface energy (γ_C) of PTFE, whose chains are comprised of $–CF_2–$ groups, is 18 mN/m, whereas that of a partially fluorinated polymers exhibiting segregated CF_3-terminated groups at the outermost portion of the surface, is 9 mN/m.[33] This means that, for certain applications, desirable fluoropolymer surface-properties may be achieved without the need for bulk fluorination.[27,34]

A key factor when working with ultralow surface energy polymers is the identification of appropriate techniques for the fabrication of film structures.[34] Methods for deposition of such films include conventional solution-based procedures such as spin-coating or solution casting,[27,35,36] chemical vapor deposition,[27,37] chemical adsorption,[38] and surface-initiated polymerizations.[21,39,40] The latter are not common, and among these, surface-initiated atom transfer radical polymerization (SI-ATRP) has been the prevalent technique used for the direct growth of partially fluorinated films from fluorinated monomers.[40-42] However, studies performed by several research groups[40-44] show that films produced by this technique achieve low thicknesses, usually in the range from 20 to 100 nm. For some applications, such as protective coatings, such films are too thin to offer the requisite protection and robustness.[27] Therefore, combining the advantages of SIP techniques with new approaches that enable the routine preparation of coatings with thickness greater than 1 μm could have a large impact on the area of specialty coatings.

Surface-Initiated Atom-Transfer Radical Polymerization and Macroinitiation Approaches

Surface-initiated ATRP is widely used because it enables the preparation of a wide range of polymer films with diverse chemical functionality and controlled thickness from both flat and curved surfaces, and porous substrates.[45,46] Another advantage is that many films prepared by means of SI-ATRP may undergo post-polymerization reactions for further derivatization.[47,48] The polymerization mechanism of ATRP has been thoroughly described by Matyjaszewski and co-workers.[49-51] High grafting density is necessary for the formation of thick surface-initiated polymer films.[52] Furthermore, this characteristic has a direct effect on other significant properties of polymer films, such as robustness,[53] friction,[54] wettability,[55] and biological interactions.[56] Consequently, researches have resorted to the use of macrointiators as a tool to enhance grafting density.[57] This approach has been intensively applied, in particular, in the formation of polymer films by SI-ATRP. For example, Liu et al.[58] deposited an anchoring polymer layer consisting of poly(glycidyl methacrylate) onto silicon wafers followed by exposure to bromoacetic acid vapor to create a macroinitiator for subsequent SI-ATRP. By contrast to a self-assembled monolayer (SAM) of ATRP initiators, the initiator surface density achieved by the macroinitiation approach increased by a factor of ~ 13 (~ 40•nm^{-2} for the macroinitiator vs. ~ 3•nm^{-2} for the SAM). Wang and co-workers[59] used a macroinitiation approach to coat attapulgite nanofibrillar clay with a well-defined star polymer exhibiting a hydrophilic core and a hydrophobic shell. Briefly, a hyperbranched aliphatic polyester was grown onto attapulgite by exposing it to γ-aminopropyltriethoxysilane and subsequently performing a one-pot polycondensation of the AB$_2$-type monomer 2,2.bis(hydroxymethyl)propionic acid. The resulting hydroxyl-rich hyperbranched polyester was then exposed to a bromoacetylation process to introduce bromoacetic ester groups, and therefore, produce the macrointiator for subsequent SI-ATRP of methyl methacrylate. Other examples of alternative chemical routes for the synthesis and formation of macroinitiators onto various substrates, followed by SI-ATRP, include the acidic oxidation of carbon spheres followed by exposure to thionyl chloride, glycol, and a bromide-containing ATRP species,[60] the sterification of the hydroxyl groups present in dried starch granules by bromoacetylbromide,[61] and the use of SI-ATRP-grown poly(methylmethacrylate) brushes from silicon wafers as reinitiation sites.[62] In addition, the adsorption of polyelectrolyte macroinitiators onto differents substrates constitutes a relatively recent alternative to enhance the grafting density as well.[52,57,63,64]

In this thesis, I will combine two SIP techniques, namely SI-ATRP and SI-ROMP, to prepare surface-bound, thick, partially fluorinated polymer films from 5-(perfluoro-n-alkyl)norbornene monomers. ATRP will be used to grow a macroinitiator and SI-ROMP to produce the final coatings.

SIP and Composite Membranes

During the past 3 decades research efforts have utilized innovative fabrication methods, including interfacial polymerization, plasma polymerization, reactive surface treatment, and solution coating to form composite membranes.[6,65] Such membranes are highly valued because of their physicochemical features, including high mass transport rates, mechanical stability, and strength. In general, these consist of a thin, selective layer sustained by a much thicker and permeable microporous substrate. This configuration allows composite membranes to provide higher fluxes with greater selectivity than those provided by homogeneous membranes.[65,66] Porous supports from which polymer materials have been grown include alumina,[6,67] cellulose,[68] and PDMS.[69] SIP has been used in the synthesis of the thin selective skin of these membranes.[6,67] These modifications create functional membranes with potential use in gas or liquid separations,[6,70] nanofiltration,[70] pervaporation,[67] protein adsorption,[70] catalytic membranes,[70] and in the creation of proton conducting platforms.[71] For example, Balachandra et al.,[6] used SI-ATRP to modify porous alumina membranes with poly(ethylene glycol dimethacrylate) (PEGDMA) to form a selective, cross-linked skin. They compared the performance in gas separation of this film to that of a linear polymer film, poly(2-hydroxyethyl methacrylate) (PHEMA), and found that cross-linked PEGDMA films exhibit higher selectivity than those of linear PHEMA ones. The CO_2/CH_4 selectivity of PEGDMA and PHEMA were ~20 and ~0.6, respectively. In a similar manner, Grajales et al.,[72] modified porous alumina substrates with polymer brushes made of poly(ethylene glycol) (PEG), and also with copolymer films of poly(ethylene glycol methyl ether methacrylate) (PEGMEMA) exhibiting short and long PEG chains, to study the effects of monomer composition on the selectivity of CO_2. Results showed that copolymerization of the PEGMEMA monomers forms films that are stable and exhibit a CO_2/H_2 selectivity of ~12, and do not crystalize, therefore, avoiding any reduction in the flux of the membrane. Recently, Yameen et al.,[71,73,74] have worked on the fabrication of composite membranes with proton conducting channels. Their approach consisted of using SI-ATRP to incorporate polyelectrolyte brushes (poly(3-sulfopropylmethacrylate)[71], copolymers of sulfopropylmethacrylate (SPM) and monomethoxy oligo(ethylene glycol) methacrylate (MeOEGMA), polySPM-co-MeOEGMA,[73] and poly(2-acrylamide-2-methylpropane sulfonic acid) (polyAMPS)[74]) onto the surface of porous silicon substrates. Notable results of these investigations include proton conductivities in the range of 1×10^{-2} S/cm[71] and proton-conducting channels with finely tuned physicochemical characteristics.[73]

This thesis will investigate the use of SI-ROMP to produce fluorocarbon-containing polymer films that grow within, throughout, and between nanoporous materials, and to study the influence of polymerization time and sulfonation levels of the polymer backbone on wettability and the transport of simple ions.

Soft Lithography

Whitesides and co-workers developed a set of non-photolithographic techniques, known as “Soft Lithography”, as an alternative option to long-established techniques, such as photolithography, to fabricate microstructures and microsystems.[75] These techniques are based on the printing of SAMs and molding of organic polymers.[75] Soft lithography employs soft materials, e.g., poly(dimethylsiloxane) (PDMS), that may not exhibit the same physical properties of traditional rigid materials such as silicon, but offer advantages such as the capability to mold small-scale substrates with high fidelity, chemical inertness, transparency, durability, and low cost among others.[76] These techniques include microcontact printing (μCP), micromolding in capillaries (MIMIC), microtransfer molding (μTM), and replica molding (REM).[77]

μCP is a technique used for the fabrication of micro- and nanostructured surfaces.[78,79] This method involves the use of an elastomeric PDMS stamp with a relief pattern on its surface to deliver adsorbate molecules (“ink”) onto determined areas of both planar and non-planar substrates to form well-defined regions exhibiting different physical and chemical properties.[80] Pioneering work involving μCP in conjunction with SIP (ROP and ATRP) methods to grow polymer brushes from an active self-assembled monolayer (SAM) in order to amplify the SAM into a macromolecular film and mask defects formed within the monolayer and improve barrier properties against dry etchants was performed by Husemann et al.,[81] and Shah et al.[82] Recently, Zotti et al.,[83] and Chen et al.,[84] used this combination of techniques to pattern conductive polymers and complex poly(N-isopropylacrilamide) brush microstructures, respectively.

In the case of MIMIC, a PDMS replica exhibiting recessed channels is placed in contact with a substrate, and filled with a prepolymer by means of capillary action. Subsequent exposure to traditional curing conditions, such as heat or light, enables curing of the polymer.[85,86] In μTM, the patterned PDMS mold is filled with a prepolymer and placed in contact with the surface of a substrate, and subsequent heating or UV light is applied to cure the prepolymer. Afterwards, the PDMS mold is removed leaving behind a patterned microstructure on the surface.[76,77] In REM, an ultraviolet or thermally curable polymer is cast onto an elastomeric mold (PDMS) exhibiting a patterned relief structure on its surface. As a result, a hand-held polymeric material is obtained.[87]

Soft lithography is a versatile technique capable of fabricating microstructures and microsystems in polymers on different types of substrates. However, these processes (MIMIC, μTM, and REM) create either "physisorbed" or hand-held materials that are not truly bound to the solid surfaces. In general, microstructures such as microtransformers, microcoils, diffraction gratings, channels for microfluidic devices, patterns of spin crossover nanoparticles, and polymer brushes, among others, have been generated using these techniques.[76,77,86,88,89]

In this thesis, I will combine soft lithography and SIP techniques to develop a process termed micromolding surface-initiated polymerization (μMSIP) to provide partially fluorinated, surface-bound polymer films with microscale surface texture.

Superhydrophobicity and Plant Leaves

Hydrophobicity refers to a weak interaction between some types of matter and water. Materials displaying this property exhibit a low surface energy. The enhancement of such a quality, achieved by the combination of hydrophobicity and surface roughness is known as superhydrophobicity.[90,91] To better understand this behavior we must take into account the contact angle (θ) of a drop placed on a surface by means of a syringe. This angle is a qualitative assessment of the interactions between the solid surface and the liquid drop. When the drop advances across the surface as a result of liquid being added to it, θ is defined as advancing (θ_A). If the drop recedes across the surface, i.e., liquid being withdrawn, θ is defined as receding (θ_R). Both θ_A and θ_R are characteristic of the surface chemistry and topography.[92] In addition, these processes may exhibit different activation energies, and therefore, they are not the reverse of one another; the difference between θ_A and θ_R, known as contact angle hysteresis, is a reflection of such asymmetry.[90,92] Surfaces must meet two criteria in order to be considered as superhydrophobic, namely, exhibit $\theta_A > 150°$ and a hysteresis $< 10°$.[90,93] The wetting behavior of superhydrophobic surfaces can be analyzed from the perspective of two states: the Wenzel state and the Cassie state, which is the true superhydrophobic state.[91,94,95] If a liquid is in the Wenzel state, the liquid follows the contours of the entire solid surface area, which introduces a roughness factor (r) that takes into account the heterogeneous topography of the substrate.[91,93,94]

$$r = \frac{actual\ area\ of\ interface}{geometric\ area} \tag{2.1}$$

The Wenzel model relates the contact angle of rough surfaces θ_W to that of a smooth surface θ_{smooth} by

$$cos\theta_W = r\ cos\theta_{smooth} \tag{2.2}$$

Unlike the Wenzel state, the Cassie state is defined by the liquid sitting atop the surface roughness, suggesting the presence of an air interlayer trapped between the surface and the contacting aqueous phase.[95,96] Accordingly, the composite interface consists of liquid-solid, liquid-air, and solid-air interfaces. The apparent contact angle θ_C is estimated by equation (2.3)

$$cos\theta_C = \chi_s cos\theta_s + \chi_{air} cos\theta_{air} \tag{2.3}$$

Taking into account that the contact angle of the liquid in air (θ_{air} = 180°), and that $\chi_s + \chi_{air} = 1$, equation (2.3) becomes

$$cos\theta_C = \chi_s(cos\theta_s + 1) - 1 \tag{2.3a}$$

where χ_s and χ_{air} are the fractions of the surface area in contact with the liquid and air, respectively. Individual application, or combination, of fabrication methods and surface chemistry has been used to obtain superhydrophobic surfaces.[91,97] Some examples include photolithography,[92] etching,[98] soft lithography,[99] silane chemistry,[91,92] and casting or phase separation of hydrophobic polymers.[100,101]

Nature provides a vast array of superhydrophobic surfaces,[91,102] including the termite wing, water strider, duck feathers, and hundreds of species of plants.[103] The detailed investigation performed by Neinhuis and Barthlott[104] on the micromorphological characteristics of a large number of plant species exhibiting water-repellant surfaces provides valuable insight on how the combination of a strongly structured relief, comprised of convex or papillose epidermal cells, and hydrophobic chemical compounds such as epicuticular waxes has a profound effect on the superhydrophobic behavior of plant leaves. An elaborate description on the functions and the morphologies of these waxes and how their 2- and 3-D structures, exhibiting dimensions between hundreds of nanometers to several micrometers, influence wettability, self-cleaning, and light reflection on the surface of leaves was done by Koch et al.[105] Superhydrophobicity in plants provides a self-cleaning role, which intrinsically, can be assumed as a self-defense mechanism.

In this connection, dust particles are removed from the surface of the leaves by rain, fog or dew, and adhesion of pathogenic organisms, e.g., fungi and bacteria, is minimized.[104] Wagner et al.,[106] hypothesized that certain morphologies present on the surface of plant leaves are better adapted to non-wetting. By adding water/methanol mixtures, i.e., decreasing the surface tension of the liquid, certain leaves can repel mixtures containing up to 75% methanol. In this sense, leaves lacking papillose epidermal cells were more prone to wetting than those exhibiting more protuberant papillose. Interestingly, results from confocal microscopy and atomic force microscopy on the surface structures suggest that a greater number of smaller papillae perform better, in terms of low wettability, than larger but less abundant papillae.[106]

Mimicking Natural Surfaces

The superhydrophobic character and self-cleaning capability demonstrated by a large number of plant leaves are the driving forces behind numerous attempts of using these biological structures as templates for the fabrication of superhydrophobic surfaces.[91,99,103] Methods to mimic these surfaces include soft lithography,[99] lithography of silicon wafers,[103] UV-nanoimprint lithography,[107] etching,[108] and membrane casting.[100] Sun et al.,[99] described a nanocasting process to fabricate an artificial lotus leaf exhibiting the same contact angle (160°) of a natural leaf. Briefly, PDMS was cast onto a natural leaf, and after curing and peeling off the mold, PDMS was once again cast onto this negative replica, thus, creating a positive replica of the natural leaf. Scanning electron microscopy images showed that the morphology and intricate nanostructures of the natural leaf were present in the positive replica. Lee et al.,[108] used a three-step process to mimic natural superhydrophobic surfaces. First, photolithography was used to create well-defined microstructure patterns onto aluminum sheets. Second, the aluminum sheets were etched to form circular patterns resembling those found on water-repellent leaves. Third, anodization of the aluminum sheets was performed in order to generate hierarchical structures. Melting and subsequent cooling of high-density polyethylene (HDPE) onto the replication template resulted in a polymer exhibiting nanostructures onto the micrometer-sized features. Contact angles as high as 159° were obtained using this approach. Superhydrophobicity and self-cleaning are not exclusive of plant leaves. As mentioned above, these properties are also found in other biological systems, e.g., termites and cicadas. Arthropods, for example, exhibit a piliferous exterior consisting of inclined hairs that protrude from their cuticles.[100] Such structures have demonstrated resistance towards the impact of water drops, promote locomotion on the surface of water, and maintain a layer of entrapped air when submerged.[100] Hsu et al.,[100] were able to fabricate artificial hairy surfaces by means of pressurized membrane casting. In this template process, a hydrophobic polymer was placed on top of a porous membrane and flowed through the pores by means of high pressure and temperature. As a result, hair-like, protruding microstructures having the tip roughly parallel to the surface were obtained. Contact angles over 170° with low hysteresis were observed on these surfaces. In summary, efforts to replicate superhydrophobic and self-cleaning surfaces have been largely successful. However, the resulting products are hand-held, peel-away materials. Superhydrophobic surfaces have potential applications as self-cleaning surfaces,[103,109] water-repellent textiles,[109] ice-resistant coatings,[101] interfacial slip,[110] and anti-fouling interfaces.[111]

In this thesis, I will extend μMSIP to fabricate partially fluorinated, surface-bound polymer films that reproduce the surface topography of superhydrophobic leaves onto solid supports.

References

(1) Tsujii, Y.; Ohno, K.; Yamamoto, S.; Goto, A.; Fukuda, T. Structure and Properties of High-Density Polymer Brushes Prepared by Surface-Initiated Living Radical Polymerization. *Surface-Initiated Polymerization I* **2006,** 197, 1-45.

(2) Jennings, G. K.; Brantley, E. L. Physicochemical Properties of Surface-Initiated Polymer Films in the Modification and Processing of Materials. *Adv. Mater.* **2004,** 16, 1983-1994.

(3) Bhat, R. R.; Tomlinson, M. R.; Wu, T.; Genzer, J. Surface-Grafted Polymer Gradients: Formation, Characterization, and Applications. In *Surface-Initiated Polymerization II* **2006**; Vol. 198, p 51-124.

(4) Dyer, D. J. Photoinitiated Synthesis of Grafted Polymers. In *Surface-Initiated Polymerization I*; Jordan, R., Ed. **2006**; Vol. 197, p 47-65.

(5) Buchmeiser, M. R. Metathesis Polymerization to and from Surfaces. In *Surface-Initiated Polymerization I*; Jordan, R., Ed.; Springer-Verlag Berlin: Berlin, **2006**; Vol. 197, p 137-171.

(6) Balachandra, A. M.; Baker, G. L.; Bruening, M. L. Preparation of Composite Membranes by Atom Transfer Radical Polymerization Initiated from a Porous Support. *J. Membr. Sci.* **2003,** 227, 1-14.

(7) Escobar, C. A.; Zulkifli, A. R.; Faulkner, C. J.; Trzeciak, A.; Jennings, G. K. Composite Fluorocarbon Membranes by Surface-Initiated Polymerization from Nanoporous Gold-Coated Alumina. *ACS Appl. Mater. Interfaces* **2012,** 4, 906-915.

(8) Ruckenstein, E.; Li, Z. F. Surface Modification and Functionalization through the Self-Assembled Monolayer and Graft Polymerization. *Advances in Colloid and Interface Science* **2005,** 113, 43-63.

(9) Brittain, W. J.; Boyes, S. G.; Granville, A. M.; Baum, M.; Mirous, B. K.; Akgun, B.; Zhao, B.; Blickle, C.; Foster, M. D. Surface Rearrangement of Diblock Copolymer Brushes - Stimuli Responsive Films. In *Surface- Initiated Polymerization II*; Jordan, R., Ed. **2006**; Vol. 198, p 125-147.

(10) Advincula, R. Polymer Brushes by Anionic and Cationic Surface-Initiated Polymerization (SIP). In *Surface-Initiated Polymerization I*; Jordan, R., Ed. **2006**; Vol. 197, p 107-136.

(11) Slugovc, C. The Ring Opening Metathesis Polymerisation Toolbox. *Macromol. Rapid Commun.* **2004,** 25, 1283-1297.

(12) Huang, W.; Skanth; Baker, G. L.; Bruening, M. L. Surface-Initiated Thermal Radical Polymerization on Gold. *Langmuir* **2001,** 17, 1731-1736.

(13) Jordan, R.; West, N.; Ulman, A.; Chou, Y.-M.; Nuyken, O. Nanocomposites by Surface-Initiated Living Cationic Polymerization of 2-Oxazolines on Functionalized Gold Nanoparticles. *Macromolecules* **2001,** 34, 1606-1611.

(14) Bielawski, C. W.; Grubbs, R. H. Living Ring-Opening Metathesis Polymerization. *Prog. Polym. Sci.* **2007,** 32, 1-29.

(15) Leitgeb, A.; Wappel, J.; Slugovc, C. The ROMP Toolbox Upgraded. *Polymer* **2010,** 51, 2927-2946.

(16) Sutthasupa, S.; Shiotsuki, M.; Sanda, F. Recent Advances in Ring-Opening Metathesis Polymerization, and Application to Synthesis of Functional Materials. *Polym. J.* **2010,** 42, 905-915.

(17) Rutenberg, I. M.; Scherman, O. A.; Grubbs, R. H.; Jiang, W.; Garfunkel, E.; Bao, Z. Synthesis of Polymer Dielectric Layers for Organic Thin Film Transistors via Surface-Initiated Ring-Opening Metathesis Polymerization. *J. Am. Chem. Soc.* **2004,** 126, 4062-4063.

(18) Lerum, M. F. Z.; Chen, W. Surface-Initiated Ring-Opening Metathesis Polymerization in the Vapor Phase: An Efficient Method for Grafting Cyclic Olefins with Low Strain Energies. *Langmuir* **2011,** 27, 5403-5409.

(19) Bielawski, C. W.; Grubbs, R. H. Highly Efficient Ring-Opening Metathesis Polymerization (ROMP) Using New Ruthenium Catalysts Containing N-Heterocyclic Carbene Ligands. *Angew. Chem.* **2000,** 39, 2903 - 2906.

(20) Novak, B. M.; Risse, W.; Grubbs, R. H. The Development of Well-Defined Catalysts for Ring-Opening Olefin Metathesis Polymerizations (ROMP). *Adv. Polym. Sci.* **1992,** 102, 47-72.

(21) Faulkner, C. J.; Fischer, R. E.; Jennings, G. K. Surface-Initiated Polymerization of 5-(Perfluoro-n-alkyl)norbornenes from Gold Substrates. *Macromolecules* **2010,** 43, 1203-1209.

(22) Berron, B. J.; Graybill, E. P.; Jennings, G. K. Growth and Structure of Surface-Initiated Poly(n-alkylnorbornene) Films. *Langmuir* **2007,** 23, 11651-11655.

(23) Jeon, N. L.; Choi, I. S.; Whitesides, G. M.; Kim, N. Y.; Laibinis, P. E.; Harada, Y.; Finnie, K. R.; Girolami, G. S.; Nuzzo, R. G. Patterned Polymer Growth on Silicon Surfaces Using

Microcontact Printing and Surface-Initiated Polymerization. *Applied Physics Letters* **1999,** 75, 4201-4203.

(24) Jordi, M. A.; Seery, T. A. P. Quantitative Determination of the Chemical Composition of Silica−Poly(norbornene) Nanocomposites. *Journal of the American Chemical Society* **2005,** 127, 4416-4422.

(25) Faulkner, C. J.; Payne, P. A.; Jennings, G. K. Surface-Initiated Ring-Opening Metathesis Polymerization of 5-(perfluorohexyl)norbornene on Carbon Paper Electrodes. *J. Colloid Interface Sci.* **2010,** 351, 248-253.

(26) Ameduri, B. From Vinylidene Fluoride (VDF) to the Applications of VDF-Containing Polymers and Copolymers: Recent Developments and Future Trends. *Chem. Rev.* **2009,** 109, 6632-6686.

(27) David, W. G.; Charlie, W. S. Fluorinated Coatings and Films: Motivation and Significance. In *Fluorinated Surfaces, Coatings, and Films*; American Chemical Society: **2001**; Vol. 787, p 1-14.

(28) Delucchi, M.; Turri, S.; Barbucci, A.; Bassi, M.; Novelli, S.; Cerisola, G. Fluoropolyether Coatings: Relationships of Electrochemical Impedance Spectroscopy Measurements, Barrier Properties, and Polymer Structure. *J. Polym. Sci., Part B: Polym. Phys.* **2002,** 40, 52 - 64.

(29) Sorensen, P. A.; Kiil, S.; Dam-Johansen, K.; Weinell, C. E. Anticorrosive Coatings: A Review. *J. Coat. Technol. Res.* **2009,** 6, 135-176.

(30) Ye, Q.; Wang, X.; Li, S.; Zhou, F. Surface-Initiated Ring-Opening Metathesis Polymerization of Pentadecafluorooctyl-5-norbornene-2-carboxylate from Variable Substrates Modified with Sticky Biomimic Initiator. *Macromolecules* **2010,** 43, 5554-5560.

(31) Volksen, W.; Miller, R. D.; Dubois, G. Low Dielectric Constant Materials. *Chem. Rev.* **2009,** 110, 56-110.

(32) Steed, J. M. *U.S. Fluorocabon Industry Economic Analysis*, www.alliancepolicy.org, **2013**.

(33) Anton, D. Surface-Fluorinated Coatings. *Adv. Mater.* **1998,** 10, 1197-1205.

(34) Tsibouklis, J.; Nevell, T. G. Ultra-Low Surface Energy Polymers: The Molecular Design Requirements. *Adv. Mater.* **2003,** 15, 647-650.

(35) Genzer, J.; Sivaniah, E.; Kramer, E. J.; Wang, J.; Körner, H.; Xiang, M.; Char, K.; Ober, C. K.; DeKoven, B. M.; Bubeck, R. A.; Chaudhury, M. K.; Sambasivan, S.; Fischer, D. A. The Orientation of Semifluorinated Alkanes Attached to Polymers at the Surface of Polymer Films. *Macromolecules* **2000,** 33, 1882-1887.

(36) van Ravenstein, L.; Ming, W.; van de Grampel, R. D.; van der Linde, R.; de With, G.; Loontjens, T.; Thüne, P. C.; Niemantsverdriet, J. W. Low Surface Energy Polymeric Films from Novel Fluorinated Blocked Isocyanates. *Macromolecules* **2003,** 37, 408-413.

(37) Elkasabi, Y.; Nandivada, H.; Chen, H.-Y.; Bhaskar, S.; D'Arcy, J.; Bondarenko, L.; Lahann, J. Partially Fluorinated Poly-p-xylylenes Synthesized by CVD Polymerization. **2009,** 15, 142-149.

(38) Zenasni, O.; Jamison, A. C.; Lee, T. R. The Impact of Fluorination on the Structure and Properties of Self-Assembled Monolayer Films. *Soft Matter* **2013,** 9, 6356-6370.

(39) Jung, D.-H.; Park, I. J.; Choi, Y. K.; Lee, S.-B.; Park, H. S.; Rühe, J. Perfluorinated Polymer Monolayers on Porous Silica for Materials with Super Liquid Repellent Properties. *Langmuir* **2002,** 18, 6133-6139.

(40) Granville, A. M.; Boyes, S. G.; Akgun, B.; Foster, M. D.; Brittain, W. J. Synthesis and Characterization of Stimuli-Responsive Semifluorinated Polymer Brushes Prepared by Atom Transfer Radical Polymerization. *Macromolecules* **2004,** 37, 2790-2796.

(41) Chen, R.; Feng, W.; Zhu, S.; Botton, G.; Ong, B.; Wu, Y. Surface-Initiated Atom Transfer Radical Polymerization Grafting of Poly(2,2,2-trifluoroethyl methacrylate) from Flat Silicon Wafer Surfaces. *Journal of Polymer Science Part A: Polymer Chemistry* **2006,** 44, 1252-1262.

(42) Yamaguchi, H.; Kikuchi, M.; Kobayashi, M.; Ogawa, H.; Masunaga, H.; Sakata, O.; Takahara, A. Influence of Molecular Weight Dispersity of Poly{2-(perfluorooctyl)ethyl acrylate} Brushes on Their Molecular Aggregation States and Wetting Behavior. *Macromolecules* **2012,** 45, 1509-1516.

(43) Chen, R.; Zhu, S.; Maclaughlin, S. Grafting Acrylic Polymers from Flat Nickel and Copper Surfaces by Surface-Initiated Atom Transfer Radical Polymerization. *Langmuir* **2008,** 24, 6889-6896.

(44) Wu, Y.; Huang, Y.; Ma, H. A Facile Method for Permanent and Functional Surface Modification of Poly(dimethylsiloxane). *Journal of the American Chemical Society* **2007,** 129, 7226-7227.

(45) Olivier, A.; Meyer, F.; Raquez, J.-M.; Damman, P.; Dubois, P. Surface-Initiated Controlled Polymerization as a Convenient Method for Designing Functional Polymer Brushes: From Self-Assembled Monolayers to Patterned Surfaces. *Prog. Polym. Sci.* **2012,** 37, 157-181.

(46) Barbey, R.; Lavanant, L.; Paripovic, D.; Schüwer, N.; Sugnaux, C.; Tugulu, S.; Klok, H.-A. Polymer Brushes via Surface-Initiated Controlled Radical Polymerization: Synthesis, Characterization, Properties, and Applications. *Chem. Rev.* **2009,** 109, 5437-5527.

(47) Brantley, E. L.; Holmes, T. C.; Jennings, G. K. Modification of ATRP Surface-Initiated Poly(hydroxyethyl methacrylate) Films with Hydrocarbon Side Chains. *J. Phys. Chem. B* **2004,** 108, 16077-16084.

(48) Huang, W.; Kim, J.-B.; Bruening, M. L.; Baker, G. L. Functionalization of Surfaces by Water-Accelerated Atom-Transfer Radical Polymerization of Hydroxyethyl Methacrylate and Subsequent Derivatization. *Macromolecules* **2002,** 35, 1175-1179.

(49) Matyjaszewski, K.; Shipp, D. A.; Wang, J.-L.; Grimaud, T.; Patten, T. E. Utilizing Halide Exchange To Improve Control of Atom Transfer Radical Polymerization. *Macromolecules* **1998,** 31, 6836-6840.

(50) Matyjaszewski, K.; Patten, T. E.; Xia, J. Controlled/"Living" Radical Polymerization. Kinetics of the Homogeneous Atom Transfer Radical Polymerization of Styrene. *Journal of the American Chemical Society* **1997,** 119, 674-680.

(51) Pyun, J.; Kowalewski, T.; Matyjaszewski, K. Synthesis of Polymer Brushes Using Atom Transfer Radical Polymerization. *Macromol. Rapid Commun.* **2003,** 24, 1043 - 1059.

(52) Edmondson, S.; Vo, C.-D.; Armes, S. P.; Unali, G.-F.; Weir, M. P. Layer-by-Layer Deposition of Polyelectrolyte Macroinitiators for Enhanced Initiator Density in Surface-Initiated ATRP. *Langmuir* **2008,** 24, 7208-7215.

(53) Kobayashi, M.; Terayama, Y.; Hosaka, N.; Kaido, M.; Suzuki, A.; Yamada, N.; Torikai, N.; Ishihara, K.; Takahara, A. Friction behavior of high-density poly(2-methacryloyloxyethyl phosphorylcholine) brush in aqueous media. *Soft Matter* **2007,** 3, 740-746.

(54) Klein, J. Shear, friction, and lubrication forces between polymer-bearing surfaces. *Annu. Rev. Mater. Sci.* **1996,** 26, 581-612.

(55) Brittain, W. J.; Minko, S. A structural definition of polymer brushes. *J. Polym. Sci., Part A: Polym. Chem.* **2007,** 45, 3505 - 3512.

(56) Mei, Y.; Elliott, J. T.; Smith, J. R.; Langenbach, K. J.; Wu, T.; Xu, C.; Beers, K. L.; Amis, E. J.; Henderson, L. Gradient substrate assembly for quantifying cellular response to biomaterials. *J. Biomed. Mater. Res., Part A* **2006,** 79A, 974 - 988.

(57) Edmondson, S.; Armes, S. P. Synthesis of surface-initiated polymer brushes using macro-initiators. *Polym Int* **2009,** 58, 307 - 316.

(58) Liu, Y.; Klep, V.; Zdyrko, B.; Luzinov, I. Polymer Grafting via ATRP Initiated from Macroinitiator Synthesized on Surface. *Langmuir* **2004,** 20, 6710-6718.

(59) Liu, P.; Wang, T. Preparation of Well-Defined Star Polymer from Hyperbranched Macroinitiator Based Attapulgite by Surface-Initiated Atom Transfer Radical Polymerization Technique. *Ind. Eng. Chem. Res.* **2006,** 46, 97-102.

(60) Jin, Y. Z.; Gao, C.; Kroto, H. W.; Maekawa, T. Polymer-Grafted Carbon Spheres by Surface-Initiated Atom Transfer Radical Polymerization. *Macromol. Rapid Commun.* **2005,** 26, 1133 - 1139.

(61) Liu, P.; Su, Z. Surface-initiated atom transfer radical polymerization (SI-ATRP) of n-butyl acrylate from starch granules. *Carbohydr. Polym.* **2005,** 62, 159-163.

(62) Tomlinson, M. R.; Efimenko, K.; Genzer, J. Study of Kinetics and Macroinitiator Efficiency in Surface-Initiated Atom-Transfer Radical Polymerization. *Macromolecules* **2006,** 39, 9049-9056.

(63) Edmondson, S.; Vo, C.-D.; Armes, S. P.; Unali, G.-F. Surface Polymerization from Planar Surfaces by Atom Transfer Radical Polymerization Using Polyelectrolytic Macroinitiators. *Macromolecules* **2007,** 40, 5271-5278.

(64) Jain, P.; Dai, J.; Grajales, S.; Saha, S.; Baker, G. L.; Bruening, M. L. Completely Aqueous Procedure for the Growth of Polymer Brushes on Polymeric Substrates. *Langmuir* **2007,** 23, 11360-11365.

(65) Baker, R. *Membrane Technology and Applications*; McGraw-Hill: New York, **2002**, p 2.

(66) Seader, J. D.; Henley, E. J. *Separation Process Principles*; John Wiley & Sons, Inc., **2006**, p 493.

(67) Sun, L.; Baker, G. L.; Bruening, M. L. Polymer Brush Membranes for Pervaporation of Organic Solvents from Water. *Macromolecules* **2005,** 38, 2307-2314.

(68) Singh, N.; Chen, Z.; Tomer, N.; Wickramasinghe, S. R.; Soice, N.; Husson, S. M. Modification of Regenerated Cellulose Ultrafiltration Membranes by Surface-Initiated Atom Transfer Radical Polymerization. *Journal of Membrane Science* **2008,** 311, 225-234.

(69) Xiao, D.; Zhang, H.; Wirth, M. Chemical Modification of the Surface of Poly(dimethylsiloxane) by Atom-Transfer Radical Polymerization of Acrylamide. *Langmuir* **2002,** 18, 9971-9976.

(70) Bruening, M. L.; Dotzauer, D. M.; Jain, P.; Ouyang, L.; Baker, G. L. Creation of Functional Membranes Using Polyelectrolyte Multilayers and Polymer Brushes. *Langmuir* **2008,** 24, 7663-7673.

(71) Yameen, B.; Kaltbeitzel, A.; Langner, A.; Duran, H.; Mueller, F.; Goesele, U.; Azzaroni, O.; Knoll, W. Facile Large-Scale Fabrication of Proton Conducting Channels. *Journal of the American Chemical Society* **2008,** 130, 13140-13144.

(72) Grajales, S. T.; Dong, X.; Zheng, Y.; Baker, G. L.; Bruening, M. L. Effects of Monomer Composition on CO2−Selective Polymer Brush Membranes. *Chemistry of Materials* **2010,** 22, 4026-4033.

(73) Yameen, B.; Kaltbeitzel, A.; Langer, A.; Müller, F.; Gösele, U.; Knoll, W.; Azzaroni, O. Highly Proton-Conducting Self-Humidifying Microchannels Generated by Copolymer Brushes on a Scaffold. **2009,** 48, 3124-3128.

(74) Yameen, B.; Kaltbeitzel, A.; Glasser, G.; Langner, A.; Mueller, F.; Goesele, U.; Knoll, W.; Azzaroni, O. Hybrid Polymer-Silicon Proton Conducting Membranes via a Pore-Filling Surface-Initiated Polymerization Approach. *Acs Applied Materials & Interfaces* **2010,** 2, 279-287.

(75) Manz, A.; Becker, H.; Qin, D.; Xia, Y.; Rogers, J.; Jackman, R.; Zhao, X.-M.; Whitesides, G. Microfabrication, Microstructures and Microsystems. In *Microsystem Technology in Chemistry and Life Science*; Springer Berlin / Heidelberg: **1998**; Vol. 194, p 1-20.

(76) Xia, Y. N.; Whitesides, G. M. Soft Lithography. *Annu. Rev. Mater. Sci.* **1998,** 28, 153-184.

(77) Zhao, X.-M.; Xia, Y.; Whitesides, G. M. Soft Lithographic Methods for Nano-Fabrication. *Journal of Materials Chemistry* **1997,** 7, 1069-1074.

(78) Kaufmann, T.; Ravoo, B. J. Stamps, Inks and Substrates: Polymers in Microcontact Printing. *Polymer Chemistry* **2010,** 1, 371-387.

(79) Kumar, A.; Whitesides, G. M. Features of Gold Having Micrometer to Centemeter Dimensions Can Be Formed Through a Combination of Stamping with an Elastomeric Stamp and an Alkanethiol Ink Followed by Chemical Etching. *Applied Physics Letters* **1993,** 63, 2002-2004.

(80) Kumar, A.; Biebuyck, H. A.; Whitesides, G. M. Patterning Self-Assembled Monolayers - Applications in Materials Science. *Langmuir* **1994,** 10, 1498-1511.

(81) Husemann, M.; Mecerreyes, D.; Hawker, C. J.; Hedrick, J. L.; Shah, R.; Abbott, N. L. Surface-Initiated Polymerization for Amplification of Self-Assembled Monolayers Patterned by Microcontact Printing. **1999,** 38, 647 - 649.

(82) Shah, R. R.; Merreceyes, D.; Husemann, M.; Rees, I.; Abbott, N. L.; Hawker, C. J.; Hedrick, J. L. Using Atom Transfer Radical Polymerization To Amplify Monolayers of Initiators Patterned by Microcontact Printing into Polymer Brushes for Pattern Transfer. *Macromolecules* **2000,** 33, 597-605.

(83) Zotti, G.; Vercelli, B.; Berlin, A. Monolayers and Multilayers of Conjugated Polymers as Nanosized Electronic Components. *Accounts of Chemical Research* **2008,** 41, 1098-1109.

(84) Chen, T.; Jordan, R.; Zauscher, S. Extending Micro-Contact Printing for Patterning Complex Polymer Brush Microstructures. *Polymer* **2011,** 52, 2461-2467.

(85) Kim, E.; Xia, Y. N.; Whitesides, G. M. Polymer Microstructures Formed by Molding in Capillaries. *Nature* **1995,** 376, 581-584.

(86) Cavallini, M.; Bergenti, I.; Milita, S.; Ruani, G.; Salitros, I.; Qu, Z.-R.; Chandrasekar, R.; Ruben, M. Micro- and Nanopatterning of Spin-Transition Compounds into Logical Structures. **2008,** 47, 8596-8600.

(87) Xia, Y. N.; Kim, E.; Zhao, X. M.; Rogers, J. A.; Prentiss, M.; Whitesides, G. M. Complex Optical Surfaces Formed by Replica Molding Against Elastomeric Masters. *Science* **1996,** 273, 347-349.

(88) Whitesides, G. M.; Ostuni, E.; Takayama, S.; Jiang, X. Y.; Ingber, D. E. Soft Lithography in Biology and Biochemistry. *Annu. Rev. Biomed. Eng.* **2001,** 3, 335-373.

(89) Thibault, C.; MolnaÌ• r, G. b.; Salmon, L.; Bousseksou, A.; Vieu, C. Soft Lithographic Patterning of Spin Crossover Nanoparticles. *Langmuir* **2009,** 26, 1557-1560.

(90) Nosonovsky, M.; Bhushan, B. Superhydrophobic Surfaces and Emerging Applications: Non-Adhesion, Energy, Green Engineering. *Current Opinion in Colloid & Interface Science* **2009,** 14, 270-280.

(91) Roach, P.; Shirtcliffe, N. J.; Newton, M. I. Progess in Superhydrophobic Surface Development. *Soft Matter* **2008,** 4, 224-240.

(92) Gao, L.; McCarthy, T. J. Contact Angle Hysteresis Explained. *Langmuir* **2006,** 22, 6234-6237.

(93) Tuberquia, J. C.; Nizamidin, N.; Harl, R. R.; Albert, J.; Hunter, J.; Rogers, B. R.; Jennings, G. K. Surface-Initiated Polymerization of Superhydrophobic Polymethylene. *J. Am. Chem. Soc.* **2010,** 132, 5725-5734.

(94) Wenzel, R. N. Resistance of Solid Surfaces to Wetting by Water. *Industrial & Engineering Chemistry* **1936,** 28, 988-994.

(95) Cassie, A. B. D.; Baxter, S. Wettability of Porous Surfaces. *Transactions of the Faraday Society* **1944,** 40, 546-551.

(96) Tuberquia, J. C.; Nizamidin, N.; Jennings, G. K. Effect of Superhydrophobicity on the Barrier Properties of Polymethylene Films. *Langmuir* **2010,** 26, 14039-14046.

(97) Feng, J.; Huang, M.; Qian, X. Fabrication of Polyethylene Superhydrophobic Surfaces by Stretching-Controlled Micromolding. *Macromolecular Materials and Engineering* **2009,** 294, 295-300.

(98) Qian, B.; Shen, Z. Fabrication of Superhydrophobic Surfaces by Dislocation-Selective Chemical Etching on Aluminum, Copper, and Zinc Substrates. *Langmuir* **2005,** 21, 9007-9009.

(99) Sun, M. H.; Luo, C. X.; Xu, L. P.; Ji, H.; Qi, O. Y.; Yu, D. P.; Chen, Y. Artificial Lotus Leaf by Nanocasting. *Langmuir* **2005,** 21, 8978-8981.

(100) Hsu, S.-H.; Sigmund, W. M. Artificial Hairy Surfaces with a Nearly Perfect Hydrophobic Response. *Langmuir* **2010,** 26, 1504-1506.

(101) He, M.; Wang, J.; Li, H.; Jin, X.; Wang, J.; Liu, B.; Song, Y. Super-Hydrophobic Film Retards Frost Formation. *Soft Matter* **2010,** 6, 2396-2399.

(102) Watson, G. S.; Cribb, B. W.; Watson, J. A. How Micro/Nanoarchitecture Facilitates Anti-Wetting: An Elegant Hierarchical Design on the Termite Wing. *ACS Nano* **2010,** 4, 129-136.

(103) Furstner, R.; Barthlott, W.; Neinhuis, C.; Walzel, P. Wetting and Self-Cleaning Properties of Artificial Superhydrophobic Surfaces. *Langmuir* **2005,** 21, 956-961.

(104) Neinhuis, C.; Barthlott, W. Characterization and Distribution of Water-Repellent, Self-Cleaning Plant Surfaces. *Ann. Bot.* **1997,** 79, 667-677.

(105) Koch, K.; Ensikat, H.-J. The Hydrophobic Coatings of Plant Surfaces: Epicuticular Wax Crystals and their Morphologies, Crystallinity and Molecular Self-Assembly. *Micron* **2008,** 39, 759-772.

(106) Wagner, P.; Fürstner, R.; Barthlott, W.; Neinhuis, C. Quantitative Assessment to the Structural Basis of Water Repellency in Natural and Technical Surfaces. *Journal of Experimental Botany* **2003,** 54, 1295-1303.

(107) Lee, S.-M.; Lee, H. S.; Kim, D. S.; Kwon, T. H. Fabrication of Hydrophobic Films Replicated from Plant Leaves in Nature. *Surface and Coatings Technology* **2006,** 201, 553-559.

(108) Lee, Y.; Park, S. H.; Kim, K. B.; Lee, J. K. Fabrication of Hierarchical Structures on a Polymer Surface to Mimic Natural Superhydrophobic Surfaces. *Advanced Materials* **2007,** 19, 2330-2335.

(109) Wu, Z.; Xu, Q.; Wang, J.; Ma, J. Preparation of Large Area Double-walled Carbon Nanotube Macro-films with Self-cleaning Properties. *Journal of Materials Science & Technology* **2009,** 26, 20-26.

(110) Rothstein, J. P. Slip on Superhydrophobic Surfaces. *Annual Review of Fluid Mechanics* **2010,** 42, 89-109.

(111) Nimittrakoolchai, O.-U.; Supothina, S. Deposition of Organic-Based Superhydrophobic Films for Anti-Adhesion and Self-Cleaning Applications. *Journal of the European Ceramic Society* **2008,** 28, 947-952.

CHAPTER III

EXPERIMENTAL PROCEDURES AND CHARACTERIZATION METHODS

Experimental Procedures

Materials

Monarch 12 Karat White Gold Leaf (49 wt.-% gold and 51 wt.-% silver, 100 nm thick) was purchased from Fineartstore.com. Whatman AnodiscTM porous alumina membranes of 25 mm in diameter (including annular ring) with porosity over 50% by volume and 20 nm diameter surface pores were obtained from Fisher and used as a support for the nanoporous gold leaf. Gold shot (99.99%) was obtained from J&J Materials, and silicon (100) wafers were purchased from WRS Materials. Chrome-plated tungsten rods were obtained from R.D. Mathis. Deionized water (16.7 MΩ) was purified with a Modu-Pure filtration (Continental Water Systems Corporation) system and used for rinsing. Ethanol (200 proof) was obtained from AAPER and used as received. Nitrogen gas was obtained from AL compressed gases. Concentrated nitric and sulfuric acids, hexane (99%), methylene chloride (DCM) (99%), acetic anhydride (99.2%), sodium acetate (99.4%), sodium sulfate (Na_2SO_4), and sodium chloride were purchased from Fisher. 4-Mercapto-1-butanol (97%), Grubbs catalyst 2nd generation (1, 3-Bis-(2, 4, 6-trimethylphenyl)-2-(imidazolidinylidene) (dichlorophenylmethylene) (tricyclohexylphosphine) ruthenium), sodium trifluoroacetate (98%), Copper(I) chloride (CuCl) (99.995+%), Copper(II) bromide ($CuBr_2$) (99.999%), 2,2'-bipyridine (bpy, 99+%), N,N-dimethylformamide (DMF, 99.9%), 2-hydroxyethyl methacrylate (HEMA, >99%), 1H,1H,2H-perfluoro-1-hexene (99%), 1H,1H,2H-perfluoro-1-octene (99%), 1H,1H,2H-perfluoro-1-decene (99%), hydroquinone, potassium ferricyanide (III) ($K_3Fe(CN)_6$), and potassium ferrocyanide (II) ($K_4Fe(CN)_6{\bullet}3H_2O$) were acquired from Sigma-Aldrich. 1H,1H,2H-Perfluoro-1-dodecene (97%) was purchased from Matrix Scientific. The following chemicals were obtained from Acros Organics: (3-mercaptopropyl) trimethoxysilane (85%), trans-3,6-endomethylene-1,2,3,6-tetrahydrophthaloyl chloride ($NB(COCl)_2$ or NBDAC) (97%), methylene chloride, extra dry (DCM) (99.9%) and n-hexadecane (99%). The syntheses of 5-(perfluoro-n-alkyl)norbornenes, the initiator-terminated disulfide, ($(BrC(CH_3)_2COO(CH_2)_{11}S)_2$), and undec-10-ene-thiol are described elsewhere.[1-5] Tridecafluoro-1, 1, 2, 2-tetrahydrooctyl-1-trichlorosilane (TFOCS) was purchased from UCT Specialties. (7–8% vinylmethylsiloxane)-(dimethylsiloxane) copolymer, 1, 3, 5, 7-tetramethylcyclotetrasiloxane, platinum divinyltetramethyldisiloxane, and (25–35% methylhydrosiloxane)-(dimethylsiloxane) were purchased from Gelest, Inc. Tetraethoxysilane (99.9%) was purchased from Alfa Aesar. Dow Corning Sylgard® 184 Silicon Elastomer Kit was obtained from Ellsworth Adhesives. Glass slide mounted Klarite® substrates (Surface Enhanced Raman Spectroscopy substrates), exhibiting inverted pyramids topography, were obtained from Renishaw Diagnostics. Diamond pyramid field emitter arrays (DFEA) were generously provided by the department of Physics and Astronomy at Vanderbilt University. Scotch double-sided adhesive tape was purchased from a hardware store. Leaves from *Aristolochia esperanzae* were acquired from the Vanderbilt University Green House. Leaves from *Trifolium repens* were acquired from plants growing locally in the wild.

Preparation of Gold Substrates

Silicon wafers were cleaned with ethanol and water and dried in a nitrogen stream. Subsequently, the wafers were placed inside a CVC-PSM66 evaporator in order to sequentially evaporate 100 Å and 1250 Å of chromium and gold, respectively, onto the wafers using an evaporation rate of 1 – 2 Å/s at a base pressure of $< 4 \times 10^{-6}$ Torr. After the evaporation process, wafers were cut into samples of 1.2 cm × 3.5 cm in size.

Characterization Methods

Contact Angles

Contact angles of probe liquids on a surface provide a qualitative assessment of the composition at the outer half nanometer of the surface.[6] When a liquid drop is in contact with a solid surface in static equilibrium with its vapor, the drop may form a contact angle, θ, with the surface. θ is related to the interfacial tensions of the solid-vapor (γ_{SV}), solid-liquid (γ_{SL}), and liquid-vapor (γ_{LV}) interfaces through Young's Equation:[7]

$$cos\theta = \frac{\gamma_{SV} - \gamma_{SL}}{\gamma_{LV}} \tag{3.1}$$

The contact angle is measured by placing a drop (~5µL) of the probe fluid onto the surface by means of a syringe. The tip of the syringe remains inside the drop as the advancing and receding angles are measured. Water (H_2O) and hexadecane (HD) are generally used as contacting liquids to probe the relative hydrophilicity/hydrophobicity and oleophilicity/oleophobicity of a surface, respectively. H_2O will exhibit high contact angles if hydrophobic groups are present at the surface. HD has a greater sensitivity to specific chemical groups, especially in distinguishing hydrocarbon groups from fluorocarbon groups.[8,9] For example, a surface dominated either by $–CH_2–$, $–CH_3$ or $–CF_3$ groups will exhibit contact angle values of 0°, 48° or 83°, respectively.[10] Chapter II offers a more detailed description of contact angles, hysteresis, and wetting states. In

Chapters IV through VII, contact angles are used to qualitatively assess the wetting properties of the surfaces from which pNBFn films were grown.

Advancing water and hexadecane contact angle measurements were made using a Rame-Hart contact angle goniometer equipped with a microliter syringe. The tip of the syringe was kept inside the liquid drop as the measurements were taken on two sides of ~5 μL drops. Reported values and errors represent the average and standard deviation, respectively, of at least 3 independently prepared samples.

Scanning Electron Microscopy (SEM)

SEM provides high resolution images (down to ~5 nm in length scale) that provide topographical as well as compositional information about material surfaces. In SEM, surfaces are bombarded with electrons with a specified energy. Secondary and backscattered electrons are collected to form an image of the surface. Secondary electrons are those ejected from the sample due to inelastic collisions with source electrons, most from within the first few nanometers of the material. These secondary electrons usually have less than 50 eV of energy.[11] Backscattered electrons are source electrons that collide with nuclei with little loss of energy and are reflected "back". Backscattered electrons usually have energies greater than 50 eV.[11] The energy of backscattered electrons is proportional to the size of the nuclei they interact with; therefore, the brightness of the image can be correlated to the composition of the sample surface. SEM is used in Chapter IV to investigate the morphology of porous substrates and track the extent of growth of pNBF6 films within such substrates. In Chapter V, SEM is used to explore the surface topography of monolayer- and macroinitiated polymer films. In Chapters VI and VII, SEM is used to study the surface topography of artificial and natural (plant leaves) substrates as well as the surface topography of microtextured pNBF8 films.

Electron micrographs of the different substrates were taken with a Hitachi S-4200 or with a Quanta 250 scanning electron microscope using an accelerating voltage of 10 kV. All samples were gold-sputtered (~ 2 nm in thickness) before taking the images. The MetaMorph Offline version 7.7.0.0 image analysis software was used to analyze the images (Molecular Devices, Downington, PA).

Electrochemical Impedance Spectroscopy (EIS)

EIS is a non-destructive method used to determine the barrier properties of thin films.[12] In EIS, a sinusoidal potential perturbation is applied around an equilibrium potential, current is collected as a function of frequency of the sinusoidal perturbation, and the results can be fit by an equivalent circuit model containing resistances and capacitances to provide physical, quantitative meaning to the data. The following equation is used to determine the impedance (Z):[12]

$$Z = \frac{E_{(t)}}{I_{(t)}} = \frac{E_0 \cos(\omega t)}{I_0 \cos(\omega t - \phi)} = Z_0 \frac{\cos(\omega t)}{\cos(\omega t - \phi)} \tag{3.2}$$

where $E(t)$ is the applied potential at time t, $I(t)$ is the resulting current at time t, E_0 is the amplitude of the potential, ω is the radial frequency (equals $2\pi f$, where f is the frequency in Hz), I_0 is the amplitude of the current, ϕ is the phase shift of the output signal, and Z_0 is the magnitude of the impedance. From these equations, the impedance of a system can be characterized by a magnitude and a phase shift.

The magnitude of Z is given by:

$$|Z|^2 = (Z_{Re})^2 + (Z_{Im})^2 \tag{3.3}$$

where

$$Z_{Re} = R \tag{3.4}$$

and

$$Z_{Im} = \frac{1}{j\omega C} \tag{3.5}$$

where R is resistance, C is capacitance, and $j^2 = -1$.

A popular presentation method for impedance data is the Bode magnitude plot in which log |Z| is plotted as a function of log frequency. When a coating behaves as an ideal capacitor, the Bode magnitude plot shows a straight line with a slope of -1 and the phase angle is –90° . When the film behaves as a pure resistor, |Z| is insensitive to frequency and the resistance due to solution and charge transfer is denoted as flat lines at high and low frequency, respectively. In this case, $\phi = 0°$.

In Chapters IV and V, EIS is used to investigate the ion transport properties of the pNBF6 coated NPGL-alumina membranes and to test the barrier properties of monolayer- and macroinitiated pNBF8 films, respectively. In Chapter IV, EIS was performed with a Gamry Instruments CMS300 impedance system interfaced to a personal computer. The frequency of a 5 mV rms AC voltage was varied from 10^4 to 10^{-1} Hz, using 10 points per decade. Equivalent circuit models were used to fit the experimental spectra using the Gamry E-Chem Analyst software package. In Chapter IV, a U-tube permeation cell was used similar to that shown by Bai et al.[13] The fabricated membrane was mounted between two half U–tubes. A gold substrate counter electrode and a Ag/AgCl/saturated KCl reference electrode were placed in one half of the U-tube whereas a gold substrate working electrode was placed in the other half. Three electrolytes, all with a 0.1 M concentration were employed, namely, sodium acetate (NaAc), sodium trifluoroacetate (NaTFA), and sodium chloride (NaCl). All the experiments were performed by using 100 mL of solution or 50 mL in each half U-tube. The membranes were exposed to each salt solution for approximately 10 min before each run, and reported impedance spectra were acquired once the spectrum exhibited no appreciable change with time. The salts were run in random order. The reported impedance values and their error ranges are based on standard deviations for runs on three independent sample preparations.

In Chapter V, EIS was performed with a Gamry Instruments reference 600 potentiostat system interfaced to a personal computer. The frequency of a 5 mV rms AC voltage was varied from 10^4 to 10^{-1} Hz, using 10 points per decade. An equivalent circuit model containing a solution resistance in series with a parallel combination of coating resistance and coating capacitance, modified with a Warburg impedance component to account for the impedance response observed for uncoated metallic surfaces,[9] was used to fit the experimental spectra using the Gamry E-Chem Analyst software package. A flat-cell limited the testing area to only 1 cm^2 of each sample. The electrochemical cell consisted of an aqueous solution of 1 mM $K_3Fe(CN)_6$, 1 mM $K_4Fe(CN)_6 \cdot 3H_2O$, and 0.1 M Na_2SO_4 with a Ag/AgCl/saturated KCl reference electrode, a gold substrate counter electrode, and a gold substrate coated with the pNBF8 film to be tested as the working electrode.

Profilometry

In Chapter V, profilometry is used to determine the thickness of monolayer- and macroinitiated films in the 0.2 to 15 µm range with a high aspect ratio tip design to characterize aspect ratios as high as 10:1. Based in the contact stylus profilometry technique, thicknesses are measured by profiling the surface with a stylus tip on a line that crosses a bare substrate to film step. As the tip follows the contour of the surface, the vertical displacement of the stylus attached to a cantilever proportionally translates into a transducer's voltage output that enables the determination of the thickness after appropriate calibration.[14]

The thickness of the polymer films was measured with a Veeco Dektak 150 Stylus Profilometer. The samples were manually scratched[15] and measurements were performed over a distance of 1000 µm using a Stylus with a 12.5 µm radius, applying 5 mg of force, and employing the hills and valleys detection mode. The scan results were plane-fitted using the software of the instrument. Reported values and errors represent the average and standard deviation, respectively, of at least 3 independently prepared samples.

Spectroscopic Ellipsometry

Ellipsometry is a non-invasive and non-destructive photon detection technique used to measure the thickness and refractive index of single films, layer stacks, and substrate materials with very high sensitivity.[16] This method can measure film thickness in the range from 0.1 nm to 100 µm, depending on the spectral range used for the analysis and the homogeneity of the films.[16]

Thickness < 1 μm can be determined with a high sensitivity, usually in the Angstrom scale. In ellipsometry, linear polarized light in a specified wavelength range is reflected from a sample surface and changed, by reflection, into elliptically polarized light. Both the phase angle (Δ) and amplitude (Ψ) of the reflected light are collected by a detector, and information about the properties of the sample are contained in the complex ratio, ρ, of the Fresnel coefficients of reflection of the parallel (r_p) and perpendicular (r_s) incident plane polarized electrical field vectors.[16]

$$\rho = \frac{r_p}{r_s} \tag{3.6}$$

The fundamental equation of ellipsometry describes the connection between the measured amplitude (Ψ) and phase angle (Δ) quantities and the sample properties contained in the coefficient of reflection ρ:

$$\rho = tan\Psi e^{i}\Delta \tag{3.7}$$

To acquire quantitative information, model layers representing the film on the surface are used to fit theory to the measured data. A simple, effective model for thin organic films is the Cauchy equation:

$$n = A + \frac{B}{\lambda^2} + \frac{C}{\lambda^4} + \cdots \tag{3.8}$$

where *n* is the film refractive index, *A*, *B*, and *C* are model fit parameters, and λ is the wavelength of incident light. The terms on the right-hand side of Equation 3.8 are optimized according to a minimization of the mean square error to fit to the experimental spectra and enable estimation of both *n* and the thickness of the film.[17] The Cauchy model assumes a film to be optically transparent and uniform in thickness.

A J.A.Woollam M-2000DI variable angle spectroscopic ellipsometer was used to measure film thicknesses less than 100 nm (Chapter V). The thickness of films was determined using a two-parameter Cauchy model (the Cauchy model does not adequately describe the data for thick pNBFn films as the films become opaque). Thicknesses were fit to data taken at 75° from the surface normal over wavelengths from 400 to 700 nm, using a refractive index of 1.5[18] and 1.38[3,19] for PHEMA and pNBFn films, respectively. Optical constants of the underlying gold used in the preparation of each sample were taken prior to polymer film deposition and used as a baseline for thickness measurements. The reported average thickness and standard deviation for PHEMA films are based on 80 different samples produced in 5 different batches. The reported thickness values and errors for pNBFn films represent the averages and standard deviations, respectively, from at least three different films.

Atomic Force Microscopy (AFM)

Atomic force microscopy (AFM) is a scanning probe technique used to image the topography of a surface.[20] To measure the topography of a surface, AFM relies on the detection of the deflections of a tiny cantilever holding a sharp tip when scanning the surface. Currently, cantilevers are made of Si, Si_3N_4, or SiO_2 and tips are made of Si_3N_4 or SiO_2. Attractive and repulsive forces come to play when a tip approaches the sample surface. However, repulsive forces which are extremely short range in nature are responsible for atomic resolution.[20] When scanning the surface, the AFM can use the partial influence of the repulsive force from the sample to vibrate (tapping mode) or remain static and make contact with the sample surface (contact mode). To eliminate potential damage to the surface due to lateral forces (i.e. scraping) across the sample and improve lateral resolution, soft polymeric materials are usually operated in tapping mode.[21] In Chapter VI, AFM is used to probe the surface topography of the master substrates, h-PDMS molds, and textured polymer films.

Reflectance Absorption Infrared Spectroscopy (RAIRS)

Reflectance absorption infrared spectroscopy (RAIRS) is a non-destructive, vibrational spectroscopic method used to identify and characterize the chemical composition and structure of molecules and thin films.[22] RAIRS involves a single external reflection of an IR beam at a reflective substrate that is coated by an organic film. The reflected light creates an electric field normal to the substrate. Vibrational spectra are used as characteristic fingerprints for adsorbate molecules, adsorption configurations, and structures.[22] Substrates can be metallic or non-metallic and should not produce absorption bands in the spectral range of interest. Peak positions and intensities in the RAIRS spectrum can provide compositional, orientational, and structural information on the polymer films. Molecular groups within the polymer film absorb the IR radiation to yield absorbance peaks in the spectrum with intensities that depend on the concentration of those groups within the films and the orientation of their transition dipole moments relative to the electric field.[23] In this thesis, RAIRS is used to study the compositional changes of PHEMA films (Chapter V) after the acylation and polymerization steps. Table 3.1 lists the absorption bands of the different chemical groups present in the organic films shown in this thesis. Detailed discussion about these can be found in Chapter V.

A Varian 3100 FT-IR Excalibur Series infrared spectrometer, equipped with a liquid-nitrogen-cooled, narrow-band MCT detector, was used to perform RAIRS. The incident angle of the p-polarized light was set at 80° from the surface normal. The instrument was run in single reflection mode and equipped with a universal sampling accessory. The spectral resolution was 2 cm^{-1}. A deuterated dodecanethiol-d_{25} self-assembled monolayer on gold was used as the background, and each spectrum was accumulated over 1000 scans.

Table 3.1. Positions of the absorption bands of the different vibrational modes present in the organic films shown in this thesis.[23,24]

Wavenumber (cm^{-1})	**Chemical Group**	**Description**
3200 – 3650	–OH	Stretching vibrations
2800 – 3050	C–H	Stretching vibrations of CH_2 and CH_3 groups
1732	C=O	Stretching vibrations
1483	CH_2	In-plane bending vibrations
1367	CH_2	Twisting and rocking vibrations
1300 – 1400	CF_2	Stretching vibrations (parallel to the chain)
1100 – 1300	CF_2	Stretching vibrations (perpendicular to the chain)
1079	C–O–C	Stretching vibrations

X-ray Photoelectron Spectroscopy (XPS)

XPS is a technique used to investigate the chemical composition of surfaces.[25] XPS measures the kinetic energy and number of escaping electrons from a surface as the material is irradiated with x-rays in ultra-high vacuum conditions. In these conditions, the composition, chemical state, and electronic state of the material are determined for the outermost ~10 nm of the interface.[25,26] Experimental results are reported in counts per second as a function of binding energy. In this context, the binding energy (E_B) and the kinetic energy (E_K) are related by the following relationship

$$E_K = hv - E_B - \Phi \tag{3.9}$$

where hv is the energy of the incident photons and Φ is the work function of the spectrometer.[26] Data were analyzed using CasaXPS data analysis software to calculate the atomic percentages using the peak area and elemental sensitivity factors. In Chapter V, XPS is used to examine the surface composition of PHEMA before and after the acylation and activation steps to quantify the extent of conversion of the hydroxyl groups of PHEMA as well as the degree of attachment of initiator species to the modified-PHEMA films.

XPS was conducted on a Physical Electronics (PHI) VersaProbe 5000 equipped with a monochromatic Al Kα x-ray source. A 200 μm, 50 W X-ray beam was rastered over a 800 x 200 μm analysis area. Electrons were collected at 45° from sample parallel at a pass energy of 11.85 eV for the high resolution data comparing the chemistry on the samples. Angle resolved XPS (ARXPS) spectra were acquired at take off angles of 15° to 90° from the sample parallel using a pass energy of 57.8 eV. Charge neutralization was accomplished using 1.1 eV electrons and 10 eV Ar^+ ions.

Rutherford Backscattering Spectroscopy (RBS)

RBS is an ion detection technique used for quantitative analysis of composition, thickness, and depth profiles of thin solid films or solid samples near the surface region.[27]

Detection limits range from a few parts per million (ppm) for heavy elements to a few percent for light elements, with typical depth resolution on the order of 20–30 nm.[28] In RBS, which is based on collisions between atomic nuclei, a beam of monoenergetic ions, usually H^+ or He^+ of typical energy 0.5 to 2.5 MeV, is used to bombard a target, and the energy of the backscattered ions is recorded with an energy sensitive detector and analyzed .[27,28] The energy of the backscattered particle, which is influenced by the loss of energy due to the transfer of momentum to the stationary target atom and the loss of energy due to transmission through the sample material, determines the mass of the target atom.[27,28] Quantification of elemental concentrations by RBS depends upon the scattering cross section of the element of interest and the stopping cross section of the sample matrix, both of which have been measured and tabulated.[28] In Chapter V, RBS is used to measure the areal concentration (atoms•cm^{-2}) of Ru in the modified-PHEMA films after exposure to a Grubbs catalyst solution.

RBS was conducted on beam line 6SDH at Vanderbilt University, using a NEC tandem pelletron accelerator equipped with an Alphatross ion source. 3.5 MeV Helium (He^{++}) particles irradiated the sample at an incident angle of 180° to the sample normal, and the backscattered particles were detected at an incident scattering angle of 160°. The detector was calibrated with a Bismuth (Bi^{209}) implanted (100) boron-doped silicon wafer, implanted to 5×10^{15} atoms•cm^{-2} at 30 KeV. A total charge of 5μC was collected on all samples.

References

(1) Tuberquia, J. C.; Nizamidin, N.; Harl, R. R.; Albert, J.; Hunter, J.; Rogers, B. R.; Jennings, G. K. Surface-Initiated Polymerization of Superhydrophobic Polymethylene. *J. Am. Chem. Soc.* **2010,** 132, 5725-5734.

(2) Peanasky, J. S.; McCarley, R. L. Surface-Confined Monomers on Electrode Surfaces. 4. Electrochemical and Spectroscopic Characterization of Undec-10-Ene-1-Thiol Self-Assembled Monolayers on Au. *Langmuir* **1998,** 14, 113-123.

(3) Faulkner, C. J.; Fischer, R. E.; Jennings, G. K. Surface-Initiated Polymerization of 5-(Perfluoro-n-alkyl)norbornenes from Gold Substrates. *Macromolecules* **2010,** 43, 1203-1209.

(4) Perez, E.; Laval, J. P.; Bon, M.; Rico, I.; Lattes, A. Synthesis of Bicyclo [2· 2· 1] Hept-2-Enes with Mono and Disubstituted Long Perfluorinated Chains CnF2n+1 (n = 4,6,8,10) Investigation of Association in Solution by 19F NMR Study of Polymerization Via a Metathetic Reaction. *J. Fluorine Chem.* **1988,** 39, 173-196.

(5) Shah, R. R.; Merreceyes, D.; Husemann, M.; Rees, I.; Abbott, N. L.; Hawker, C. J.; Hedrick, J. L. Using Atom Transfer Radical Polymerization To Amplify Monolayers of Initiators Patterned by Microcontact Printing into Polymer Brushes for Pattern Transfer. *Macromolecules* **2000,** 33, 597-605.

(6) Laibinis, P. E.; Bain, C. D.; Nuzzo, R. G.; Whitesides, G. M. Structure and Wetting Properties of .omega.-Alkoxy-n-alkanethiolate Monolayers on Gold and Silver. *The Journal of Physical Chemistry* **1995,** 99, 7663-7676.

(7) Zisman W, A. Relation of the Equilibrium Contact Angle to Liquid and Solid Constitution. In *Contact Angle, Wettability, and Adhesion*; American Chemical Society: **1964**; Vol. 43, p 1-51.

(8) Berron, B. J.; Graybill, E. P.; Jennings, G. K. Growth and Structure of Surface-Initiated Poly(n-alkylnorbornene) Films. *Langmuir* **2007,** 23, 11651-11655.

(9) Brantley, E. L.; Jennings, G. K. Fluorinated Polymer Films from Acylation of ATRP Surface-Initiated Poly(hydroxyethyl methacrylate). *Macromolecules* **2004,** 37, 1476-1483.

(10) Bain, C. D.; Troughton, E. B.; Tao, Y. T.; Evall, J.; Whitesides, G. M.; Nuzzo, R. G. Formation of Monolayer Films by the Spontaneous Assembly of Organic Thiols from Solution onto Gold. *J. Am. Chem. Soc.* **1989,** 111, 321-335.

(11) Bindell, J. B. 2.2 - SEM: Scanning Electron Microscopy. In *Encyclopedia of Materials Characterization*; Brundle, C. R., Evans, C. A., Wilson, S., Eds.; Butterworth-Heinemann: Boston, **1992**, p 70-84.

(12) Gamry Instruments, I. CMS 100 Electrochemical Measurement System Software Installation Manual, Warminster, PA, **1998**.

(13) Bai, D.; Elliott, S. M.; Jennings, G. K. pH-Responsive Membrane Skins by Surface-Catalyzed Polymerization. *Chemistry of Materials* **2006,** 18, 5167-5169.

(14) Wood, J. W.; Redin, R. D. A Simple Profilometer for Film Thickness Measurement. *Review of Scientific Instruments* **1993,** 64, 2405-2406.

(15) Manaka, T.; Ohta, H.; Iwamoto, M.; Fukuzawa, M. Electrostatic Properties of Polyethylene LB Films on Metal Electrodes. *Colloids and Surfaces A: Physicochemical and Engineering Aspects* **2005,** 257–258, 287-290.

(16) Gruska, B.; Röseler, A. Photon Detection. In *Surface and Thin Film Analysis*; Wiley-VCH Verlag GmbH: **2002**, p 265 - 274.

(17) Woollam, J. A.; Bungay, C.; Hilfiker, J.; Tiwald, T. VUV and IR Spectroellipsometric Studies of Polymer Surfaces. *Nuclear Instruments & Methods in Physics Research Section B-Beam Interactions with Materials and Atoms* **2003,** 208, 35-39.

(18) Brantley, E. L.; Holmes, T. C.; Jennings, G. K. Blocklike Fluorocarbon and Hydrocarbon Copolymer Films via Surface-Initiated ATRP and Postpolymerization Reactions. *Macromolecules* **2005,** 38, 9730-9734.

(19) Seehof, N.; Grutke, S.; Risse, W. Selective Reaction with Exo-Isomers in Ring-Opening Olefin Metathesis Polymerization (ROMP) of Fluoroalkyl-Substituted Norbornene Derivatives. *Macromolecules* **1993,** 26, 695-700.

(20) Friedbacher, G. Scanning Probe Microscopy. In *Surface and Thin Film Analysis*; Wiley-VCH Verlag GmbH: **2002**, p 276 - 290.

(21) Seo, Y.; Jhe, W. Atomic Force Microscopy and Spectroscopy. *Reports on Progress in Physics* **2008,** 71, 016101.

(22) Hinrichs, K. Photon Detection. In *Surface and Thin Film Analysis*; Wiley-VCH Verlag GmbH: **2002**, p 249 - 254.

(23) Yadav, L. D. S. *Organic Spectroscopy*; Springer, **2005**.

(24) Perova, T. S.; Vij, J. K.; Xu, H. Fourier Transform Infrared Study of Poly(2-hydroxyethyl methacrylate) PHEMA. *Colloid Polym. Sci.* **1997,** 275, 323-332.

(25) Brundle, C. R. 5.1 - XPS: X-Ray Photoelectron Spectroscopy. In *Encyclopedia of Materials Characterization*; Brundle, C. R., Evans, C. A., Wilson, S., Eds.; Butterworth-Heinemann: Boston, **1992**, p 282-299.

(26) Briggs, D.; Seah, P. *Practical Surface Analysis: Auger and X-ray photoelectron spectroscopy*; Wiley, **1990**.

(27) Palmetshofer, L. Ion Detection. In *Surface and Thin Film Analysis*; Wiley-VCH Verlag GmbH: **2002**, p 141 - 149.

(28) Baumann, S. M. 9.1 - RBS: Rutherford Backscattering Spectrometry. In *Encyclopedia of Materials Characterization*; Brundle, C. R., Evans, C. A., Wilson, S., Eds.; Butterworth-Heinemann: Boston, **1992**, p 476-487.

CHAPTER IV

COMPOSITE FLUOROCARBON MEMBRANES BY SURFACE-INITIATED POLYMERIZATION FROM NANOPOROUS GOLD-COATED ALUMINA

Adapted with permission from Escobar, C. A.; Zulkifli, A. R.; Faulkner, C. J.; Trzeciak, A.; Jennings, G. K. Composite Fluorocarbon Membranes by Surface-Initiated Polymerization from Nanoporous Gold-Coated Alumina. ACS Applied Materials & Interfaces 2012, 4, 906-915. Copyright 2012 American Chemical Society.

Introduction

Membrane technology has experienced great progress since 1963 when Loeb and Sourirajan introduced an anisotropic, defect-free, high-flux, osmotic membrane.[1] During the past three decades, research efforts have utilized innovative fabrication methods, including interfacial polymerization, plasma polymerization, and reactive surface treatment to fabricate high-performance, defect-free anisotropic membranes.[2] Composite membranes, a class of anisotropic membranes, are highly valued because of their physicochemical features, including high mass transport rates, mechanical stability, and strength. This type of membrane consists of a thin, selective layer sustained by a much thicker and permeable microporous substrate. Such a layered configuration allows composite membranes to provide higher fluxes with greater selectivity than those provided by homogeneous membranes.[1-3]

Despite the fact that most commercially available membranes are polymer-based, there is an increasing interest in producing membranes with less traditional materials.[2] The use of inorganic materials in the fabrication of anisotropic membranes is an example of such a trend. For instance, ceramic membranes, besides providing mechanical support and inherent porosity, provide the chemical inertness and thermal stability that some pharmaceutical and food microfiltration applications demand.[2] Particularly, alumina is an example of a versatile inorganic nanoporous material that has been used as a membrane. Porous alumina substrates have been widely studied and can be found in applications such as electrochemical storage and production,[4] templates for the synthesis of nanomaterials,[5] supports for thin polymer skins,[6-8] modified substrates for the filtration of biological molecules,[9] or as templates for nanocomposites.[10]

In this chapter, I show that porous metallic materials such as nanoporous gold leaf (NPGL) may also be used as tailorable membrane interfaces when mounted atop nanoporous alumina membranes. NPGL is an ultrathin, metallic, mesoporous structure synthesized by means of a chemical etching process called dealloying.[11] In this process, Ag is selectively dissolved from a commercially available Ag/Au alloy exposed to corrosive media as the Au matrix is coarsened into a porous structure. NPGL offers various advantages, including low-cost and ease of fabrication, chemical stability, control over pore size, high conductivity, thinness, high surface-to-volume ratio, and ease of surface functionalization.[11,12] These characteristics motivate the use of NPGL in a composite membrane in order to achieve higher fluxes and selectivity. For instance, the thickness of NPGL is only ~100 nm to provide a highly controlled ultrathin skin. In addition, the strong interaction between gold surfaces and thiols enables the chemical modification of the NPGL surface. Accordingly, the selectivity of NPGL may be tailored to specific needs as there are many thiol-compatible functional groups for growing polymers from pore walls to modify the chemical composition of the pore space. The aforementioned features provide NPGL with versatility for use, not only as the active skin of a composite membrane, but also for applications such as solar energy conversion,[12] sensing,[13,14] catalysis,[15,16] and electrochemistry.[15,17]

Nanoporous alumina and NPGL exhibit suitable physicochemical characteristics to be used in the design and construction of a composite membrane. For example, the former is sufficiently strong to provide the necessary mechanical support and permeable enough to allow free flow of the permeated species, whereas the latter could act as a selective skin when appropriately functionalized. Nanoporous alumina has been used in conjunction with several transition metals, e.g., Pt, Cu, Co, and Au, in previous studies in order to construct arrays of nano fuel cells, nanowires, nanoparticles, catalytic membranes, and nanoporous composites with tunable optical properties.[10,18-22] However, to the best of my knowledge, this is the first reported attempt to bind nanoporous alumina with NPGL to fabricate a composite membrane.

The work in this chapter describes the versatile fabrication and characterization of a novel anisotropic membrane (Figure 4.1). I use a surface-initiated polymerization (SIP) to grow a fluorocarbon-rich film within, atop, and between NPGL-coated nanoporous alumina to create a composite membrane where the selective polymer can be grown throughout the membrane or within either the NPGL or alumina sections, providing a tailorability of the membrane composition.

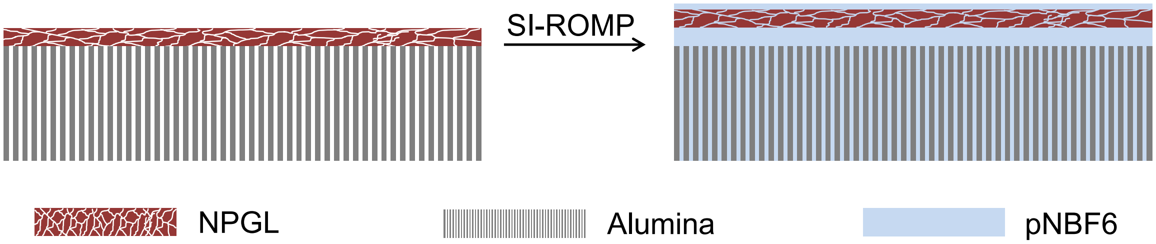

Figure 4.1. Schematic of membrane composition before and after the polymerization process.

I employ surface-initiated ring-opening metathesis polymerization (SI–ROMP), which offers rapid kinetics at room temperature and a high level of control over thickness and composition.[23,24] Examples of the versatility and flexibility provided by this technique include the modification of micrometer-sized silica particles for chromatographic applications,[25] the fabrication of a polymer dielectric layer exhibiting low capacitance and a thickness of over 1 μm,[26] and the formation of partially fluorinated films with exceptionally low critical surface tensions.[27] The polymer film in this composite membrane consists of poly(perfluorohexyl norbornene) (pNBF6), which exhibits ultralow critical surface tension and outstanding barrier properties[27] and can be grown rapidly from planar[27] and non-planar[28] supports via SI–ROMP. To provide charge transport to the membrane, sulfonation of the pNBF6 film was performed here with acetyl sulfate in order to introduce sulfonic acid and hydroxyl groups in the backbone of the polymer film and promote ion transport through the membrane.[29,30] Results from this work confirm successful integration of the pNBF6 throughout the membrane or as a selective skin initiated only from the NPGL layer.

The overall aim of this work consists of fabricating and characterizing new materials and interfaces by employing SI-ROMP within nanoporous architectures to create composite membranes. Specifically, this work aims at investigating the use of SI-ROMP to produce fluorocarbon-containing polymer films that grow within, throughout, and between nanoporous architectures, and to study the influence of polymerization time and sulfonation levels of the polymer backbone on wettability and the transport of simple ions. This SI-ROMP process provides a versatile approach to prepare uniquely layered membranes. Although surface-initiated methods have been frequently employed to modify the surface properties of a wide variety of planar and non-planar substrates, investigations reporting their use as versatile techniques for modifying internal porosity are scarce.

Experimental Methods

Fabrication of the Composite Membrane

Functionalization of the Alumina Membrane

The alumina membranes were functionalized by exposing them to a 5 mM solution of (3-mercaptopropyl)-trimethoxysilane (MPTS) in hexane at 60 °C. In order to avoid shrinkage and distortion of the annular polypropylene ring of the membranes during functionalization, these were tightly fastened using binder clips between two polycarbonate disks. A circular shape, identical in size to that of the membrane, was cut from one of the disks to allow exposure of the membrane to the silane solution. After 1 h, samples were withdrawn, rinsed with hexane, and dried in a stream of nitrogen.

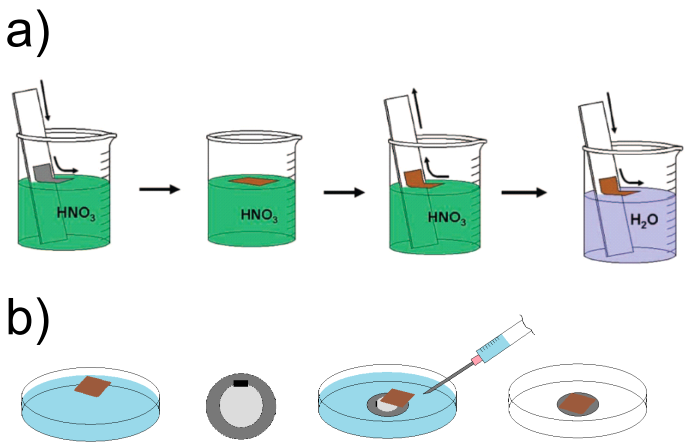

Figure 4.2. a) Schematic of the gold leaf dealloying process. Silver is removed from the gold film while in the nitric acid to create a porous structure. b) NPGL alumina assembly. The water is gently removed from the container to allow settling of the NPGL atop the alumina.

Fabrication of NPGL

Figure 4.2 shows the process to fabricate NPGL and attach it to the alumina support.[11] Briefly, square white gold leaf samples of approximately 24 x 24 mm in size were cut to ensure complete coverage of the alumina membrane. Afterwards, each sample was placed on a glass microscope slide and transferred to a glass beaker containing concentrated nitric acid. The glass slide was gently dipped into the acid at an angle approximately 20° from the surface normal, allowing the gold leaf to float on the nitric acid-air interface. As soon as the sample floated freely, the glass slide was carefully removed. After a dealloying period of 4 h, the gold leaf was removed from the acid by immersing the glass slide into the beaker, at the angle previously described, and placing it underneath the NPGL and carefully removing it. As the glass slide was withdrawn, the NPGL adhered to the surface of the glass slide. Subsequently, the NPGL was transferred to a container with deionized water for rinsing. Once again, the glass slide was carefully dipped into the deionized water container allowing the NPGL to float freely. Figure 4.3a shows a scanning electron microscopy (SEM) image of NPGL after 4 h in nitric acid and rinsing in deionized water, as described above. Rather than having a homogeneous morphology, NPGL exhibits a coarsened type of mesh with different pore sizes that generally range from 50 to 100 nm.

Alumina Membrane and NPGL Assembly

In this procedure the rinsed NPGL was transferred to a shallow glass dish containing deionized water (see Figure 4.2b). Next, the premodified alumina membrane was fixed to a polycarbonate disk by means of a small piece of double-sided tape. The disk was immersed and placed at the bottom of the dish and positioned underneath the floating NPGL. Subsequently, water was drained from the dish by means of a syringe. Simultaneously, the position of the

NPGL was maintained directly above the alumina membrane by gently creating waves on the surface of the water with the tip of the syringe. As the water level diminished, the NPGL slowly settled on top of the functionalized membrane. Binding of the two porous substrates was achieved by means of the terminal thiol groups of the alkoxysilane that was used to premodify the alumina membrane. Finally, the new two-layered structure was removed from the dish, detached from the polycarbonate disk, and gently dried in a stream of nitrogen. When an NPGL film was placed atop an unfunctionalized membrane, it did not endure rinsing or drying, as it began to peel away.

The morphology of the resulting assembly was investigated using SEM. Figure 4.3b illustrates a plan-view of an NPGL film attached to the alumina membrane. The NPGL was purposely cut in such a way that the two domains were shown. On the left side of the image, the heterogeneous ligament network and the porous structure of NPGL can be clearly seen. On the right, the heterogeneous geometry and size of the pores and the high pore density of alumina can be discerned.

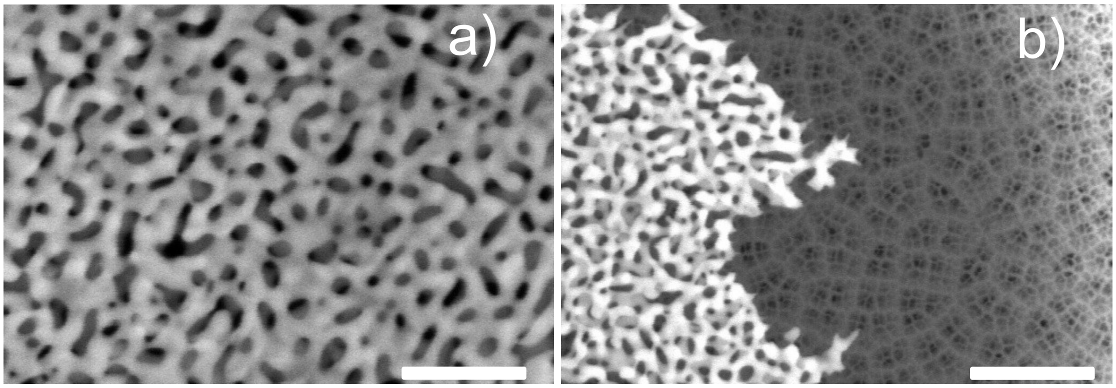

Figure 4.3. a) Scanning electron micrograph of NPGL after 4 h of dealloying. The scale bar indicates 500 nm. b) SEM NPGL atop a functionalized alumina membrane. This sample was intentionally adapted in order to show both the NPGL and the alumina. The scale bar indicates 750 nm.

Growth of the Poly(perfluorohexyl)norbornene Film on NPGL-Coated Alumina

The versatility of the polymerization process allows two polymerization approaches. The first procedure is outlined in Figure 4.4 and is similar to the process successfully used by our group in previous studies.[27,29,31] Briefly, the NPGL-coated alumina was exposed to a 1 mM ethanolic solution of 4–mercapto–1–butanol for at least 1 h to create a hydroxyl-terminated self-assembled monolayer (SAM) on the NPGL surface. Samples were rinsed in ethanol and gently dried in a stream of nitrogen. Subsequent exposure of the SAM-decorated NPGL-coated alumina membrane to a 5 mM solution of trans-3,6-endomethylene-1,2,3,6-tetrahydrophthaloyl chloride in DCM for 30 min results in the coupling of norbornenyl groups to both the underlying hydroxyl monolayer via ester linkages, and to hydroxyl groups on the alumina surface. Samples were rinsed with DCM and ethanol and dried in a stream of nitrogen. Upon exposure of the norbornenyl decorated surfaces to a 5 mM solution of Grubbs second-generation catalyst in DCM for 10 min, the entire membrane structure becomes active for SI–ROMP as a consequence of the immobilization of the initiator. Samples were rinsed in DCM and immediately exposed to a 0.05 M solution of 5-(perfluorohexyl) norbornene in DCM, resulting in the growth of partially fluorinated polymer films from both NPGL and alumina surfaces. Samples were rinsed with DCM, ethanol, water, and dried in a stream of nitrogen. Note that this procedure may also be used to selectively grow polymer films from the surface of alumina by eliminating the deposition of the hydroxyl-terminated SAM.

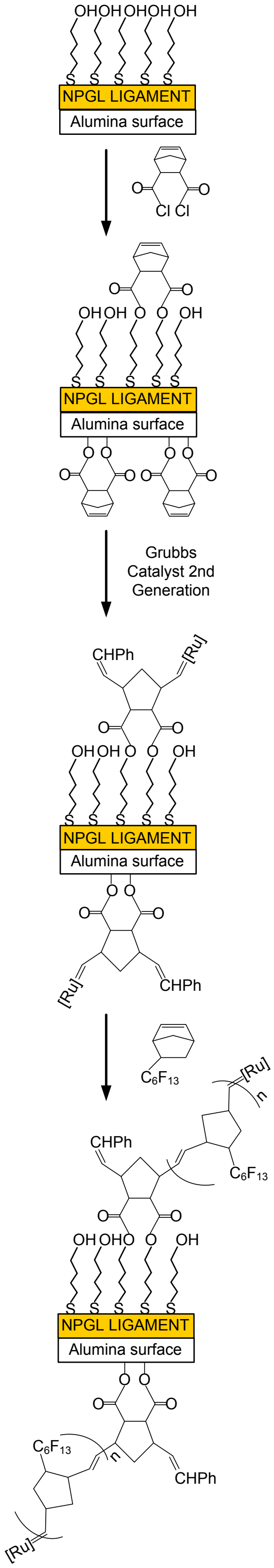

Figure 4.4. Schematic of SI-ROMP of 5-(perfluorohexyl) norbornene on the NPGL-coated alumina.

The second alternative (scheme not shown) enables the exclusive growth of a pNBF6 film on the NPGL structure. In this method, a vinyl-terminated thiol, namely, 11-undecene-1-thiol was used to functionalize the NPGL structure in order to provide reactive vinyl surface sites to which the polymerization initiator could bind. Briefly, the NPGL-coated alumina membranes were exposed to a 1 mM solution of 11-undecene-1-thiol in ethanol for at least 1 h to create a vinyl-terminated SAM. Samples were rinsed with ethanol and dried in a nitrogen stream. Subsequently, the samples were exposed to a 5 mM solution of Grubbs second-generation catalyst in DCM for 10 min. The membranes were rinsed in DCM and immediately exposed to a 0.05 M solution of 5-(perfluorohexyl) norbornene in DCM, resulting in the growth of partially fluorinated polymer films solely from NPGL. Samples were rinsed with DCM, ethanol, and water and dried in a stream of nitrogen.

Sulfonation of the pNBF6 Film

The sulfonation process described by Berron et al.,[29] was followed. In short, a 1.0 M acetyl sulfate solution in DCM was prepared immediately prior to use. Acetic anhydride (2.8 mL) was added to DCM (14.0 mL) at 0 °C. Concentrated sulfuric acid (1.0 mL) was added dropwise to the acetic acid solution resulting in a 1.0 M acetyl sulfate solution in DCM. A 1.0 mL aliquot of the 1.0 M acetyl sulfate solution was diluted to 0.1 M through the addition of 9.0 mL of dichloromethane. The pNBF6-coated NPGL-alumina assembly was exposed to the 0.1 M solution of acetyl sulfate for 1 h to yield a surface-tethered sulfonated polymer coating. Samples were rinsed with DCM and ethanol and dried in a nitrogen stream.

Results and Discussion

Growth of pNBF6 in NPGL/Alumina Membrane

NPGL-coated alumina was modified to grow pNBF6 films as shown in Figure 4.4 so that polymer is initiated within both the NPGL and the alumina pores. Figure 4.5a shows the cross-section of an unmodified assembled membrane in which the NPGL is chemically attached to the porous alumina, clearly showing NPGL (white) and alumina (gray). Figure 4.5b displays the cross-section of the filtration side (inlet) of an NPGL/alumina membrane after exposure to SI–ROMP for 5 min. Four regions can be identified in this image, namely, from the bottom up, the porous alumina, a pNBF6 interlayer, the NPGL, and an overgrown pNBF6 film atop the NPGL. Interestingly, the pNBF6 film not only overgrows atop the NPGL but also grows between the alumina and NPGL layers. As a consequence, the NPGL is lifted, in an even manner, from the alumina support. The thickness of the pNBF6 interlayer and the overgrown pNBF6 atop the NPGL averages 500 and 400 nm, respectively. This ability of SI-ROMP to slowly separate two bound materials at an average velocity of ~2 nm/s may have applications on the separation of surfaces to targeted nanoscale dimensions. Polymer growth is not limited to the inlet side of the NPGL/alumina membrane; Figure 4.5c shows the partial growth of pNBF6 filament- and film-like features along the walls of the alumina pores, indicating that the internal structure of the alumina support is also being modified.

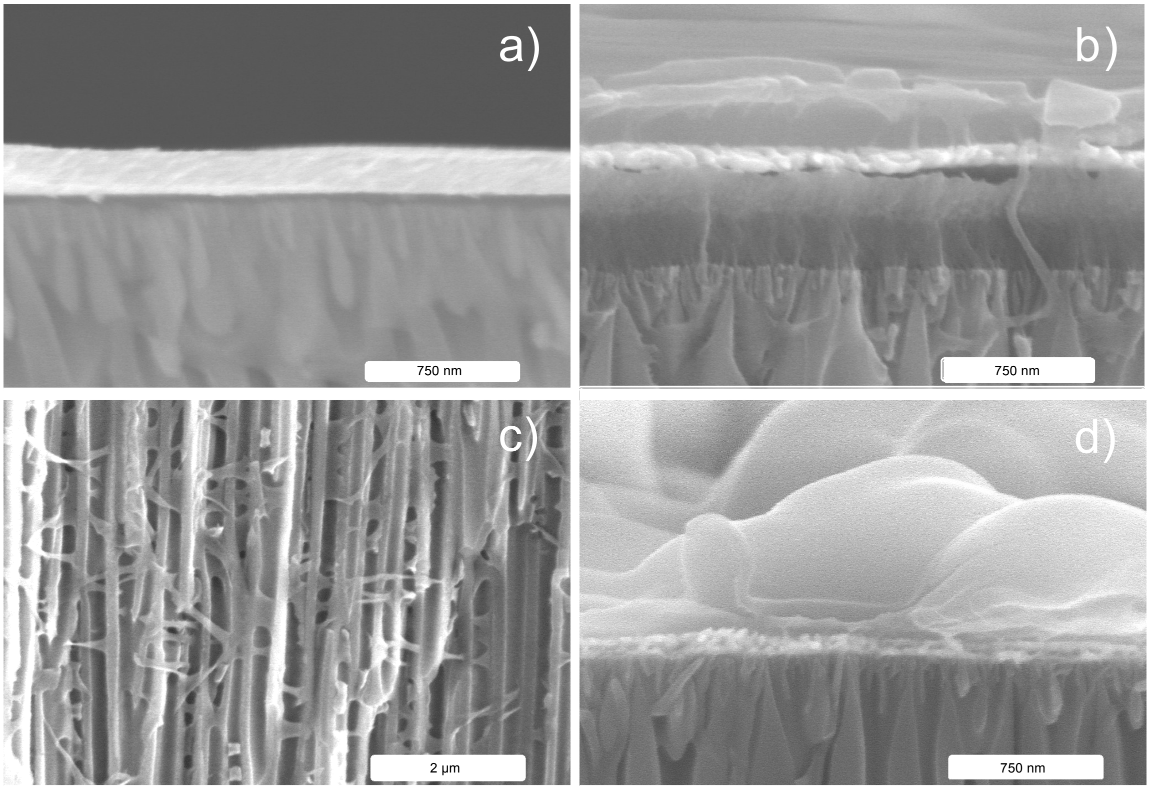

Figure 4.5. Scanning electron micrographs showing cross-sections of: a) an unfunctionalized NPGL/alumina membrane, b) the inlet side of a NPGL/alumina membrane in which pNBF6 was grown in both NPGL and alumina for 5 min, c) the alumina region of the membrane shown in b) in which pNBF6 filament- and film-like structures are present, d) the inlet side of a NPGL/alumina membrane in which pNBF6 was grown only in the NPGL for 5 min.

Figure 4.5d shows the growth of pNBF6 in an NPGL/alumina membrane in which the polymer was initiated only from the NPGL and exposed to SI–ROMP for 5 min. Polymerization of the monomer resulted in exclusive growth of pNBF6 within and atop the NPGL. Unlike the membrane in Figure 4.5b, in this membrane the NPGL does not rise upwards from the alumina support, suggesting that the presence of an interlayer in Figure 4.5b is a sole contribution of the polymer growing from the alumina. In addition, further inspection of the alumina support validates the exclusive growth in the NPGL region as no particular polymer-like features or structures are present inside its pores.

Table 4.1. Wetting properties of the NPGL/alumina assembly after various steps in the modification process. Three different polymerization times were evaluated.

	Contact angle (deg)	
	Water	HD
Sample	θ_A	θ_A
SAM/NPGL/alumina	56 ± 1	< 15
$NB(CO)_2$/SAM/NPGL/alumina	69 ± 2	< 15
NPGL/alumina, 1 min NBF6[a]	121 ± 2	69 ± 2
NPGL/alumina, 2 min NBF6[a]	128 ± 1	71 ± 1
NPGL/alumina, 5 min NBF6[a]	129 ± 2	74 ± 2

a. Contact angle values were similar on the outlet side of the alumina membrane.

Table 4.1 shows the advancing (θ_A) water and hexadecane (HD) contact angles of the polymer film grown atop the NPGL-coated alumina after each step of the modification, including the growth of pNBF6 films for 1, 2, and 5 min. Contact angle measurements on the inlet and on the outlet side (not shown on Table 4.1) of the pNBF6-modified membrane for 1, 2, and 5 min of polymerization exhibited similar values. Functionalization of the NPGL/alumina membrane with a hydroxyl-terminated thiol SAM (4-mercapto-1-butanol) yielded an advancing water contact angle (θ_A (water)) of 56°. Subsequent tethering of the hydroxyl moieties on the surface of the SAM to the norbornenyl groups in $NB(COCl)_2$ via ester linkages reduced the surface energy of the NPGL/alumina membrane as evidenced by an increase in contact angle ((θ_A (water) ≈ 69°) over that of the control SAM. Severe deformation of the drop shape did not allow measuring the receding contact angles, which is consistent with a large roughness introduced by the NPGL substrate. Both of these surfaces were wet by hexadecane due to the high-energy hydroxyl surface of the SAM and the methylene content of the $NB(COCl)_2$-modified film. Polymerization of the NBF6 monomer in NPGL/alumina membranes dramatically altered the surface characteristics. Such modification is evidenced by a surge in both water and hexadecane contact angles to represent hydrophobic and oleophobic behavior. The low wettability toward water and hexadecane exhibited by the membranes after polymerization is ascribed to the presence of fluorinated groups, such as $–CF_3$ and $–CF_2–$, on the surface of the films.[27,32] Hexadecane is more suitable to qualitatively assess the surface composition of these pNBF6 films as it exhibits a lower surface tension than water. This disparity makes hexadecane more sensitive to fluorocarbon groups, and therefore, it provides a superior characterization of the surface properties of low-energy films by magnifying dissimilarities in their surface energies.[31,33] Results in Table 1 show that the surface of the pNBF6 films is not exclusively dominated by $–CF_3$ moieties as the contact angles are not as high as those exhibited by dense $–CF_3$ surfaces (~80°).[34] Instead, contact angles range from 69 to 74° suggesting that not only $–CF_3$ moieties but also $–CF_2–$ groups may be exposed at the surface of the pNBF6 films. Furthermore, these results also suggest that for longer polymerization times, the $–CF_3$ groups increasingly dominate the surface of the pNBF6 films as the surface porosity of the NPGL is diminished.

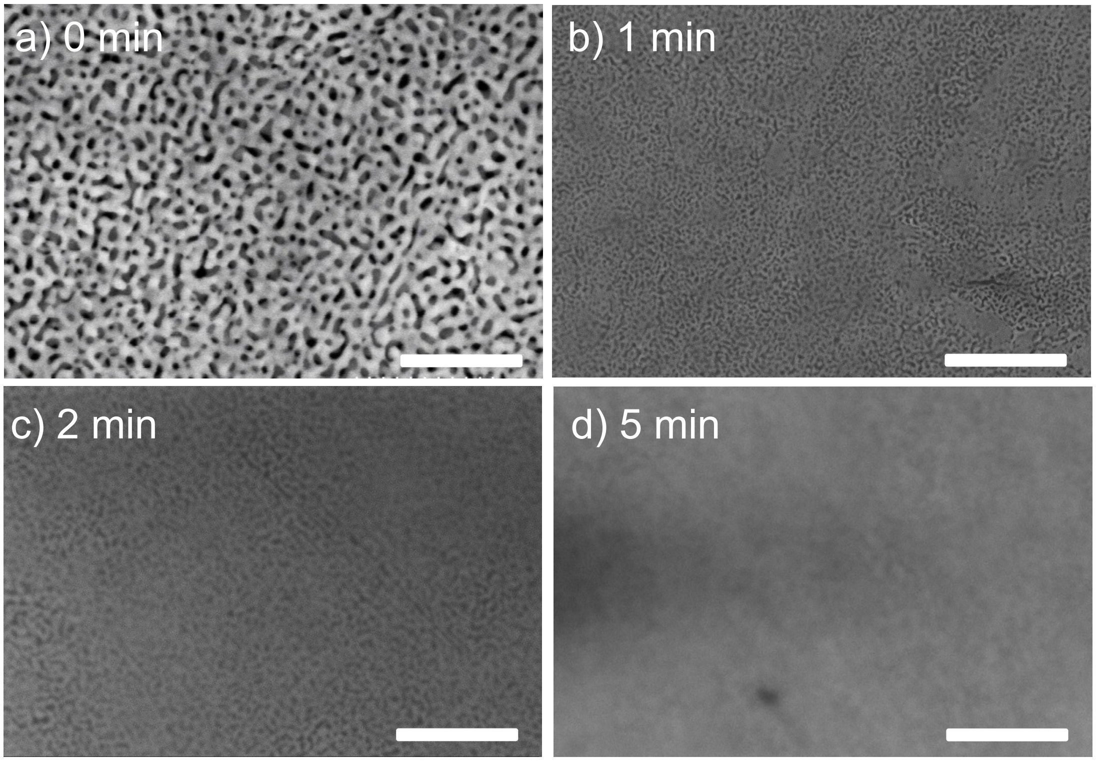

Figure 4.6. Scanning electron micrographs of pNBF6 films grown from a 0.05 M monomer solution NPGL-coated alumina after different polymerization times. The scale bar indicates 1 μm.

Figure 4.6 shows top view SEM images of pNBF6 films grown during 0, 1, 2, and 5 min of polymerization. As shown in Figure 4.6a, the NPGL-coated alumina assembly (0 min) exhibits a random porous configuration. Figure 4.6b illustrates that after 1 min of pNBF6 growth the porosity is greatly reduced as the polymer grows within the pores and throughout the entire structure. Figure 4.6c shows that a 2 min polymerization further reduces pore size, almost entirely filling the pores. A 5 min polymerization is sufficient to attain a thin polymer overlayer that covers the whole NPGL-coated alumina assembly as shown in Figure 4.6d.

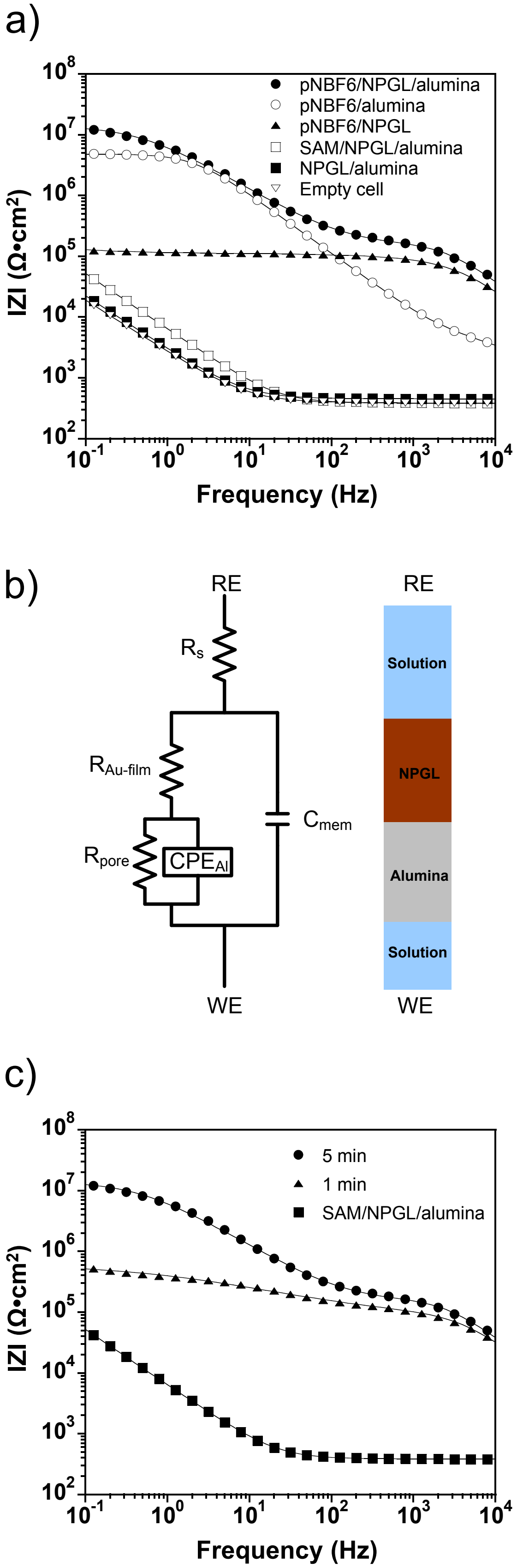

Figure 4.7. a) Electrochemical impedance spectra for pNBF6 films simultaneously polymerized for 5 min in NPGL and alumina, only alumina, and only NPGL. b) Equivalent circuit model used to fit EIS spectra for pNBF6 films grown on the NPGL/alumina assembly. RE and WE denote reference electrode and working electrode, respectively. c) Electrochemical impedance spectra collected for the empty cell, control SAM, and pNBF6 films polymerized for 1 and 5 min. The electrolyte solution for a) and c) consists of a 0.1 M aqueous solution of sodium trifluoroacetate. Solid lines indicate fits of the data using an appropriate equivalent circuit model. All films were polymerized from a 0.05 M monomer solution.

Performance of the Composite Membrane

Electrochemical Characterization

Electrochemical impedance spectroscopy (EIS) was used to quantify the barrier properties of different regions (alumina, NPGL, polymer overgrowth, etc.) within the composite membrane and thus, provide information regarding the extent of polymer growth within these layered structures. All impedance spectra were collected in a U-cell containing aqueous sodium trifluoroacetate (0.1 M) where the membrane separated two cell compartments, one containing a gold working electrode and the other containing both counter and reference electrodes. Figure 4.7a shows impedance spectra in the form of Bode magnitude plots for an empty cell (no membrane) as well as NPGL/alumina membranes, either unfunctionalized or exposed to mercaptobutanol to form a SAM on the NPGL surface, as well as those that were further functionalized with pNBF6. Comparison of the spectrum for the unfunctionalized membrane to an open cell reveals that the presence of the unfunctionalized membrane provides little, if any, measurable impedance. Both spectra reveal a resistance at high frequencies, which we will denote as a solution resistance, R_s, but is truly a combination of the resistances for ion migration both in solution and through the unfunctionalized membrane.

The spectra also reveal a capacitive impedance at low frequencies due to the double layer or interfacial capacitance of the gold working electrode and the membrane (if present). Formation of an ultrathin SAM on the gold surface of the NPGL/alumina membrane increases the capacitive impedance at low frequencies by 2.5-fold, consistent with the dielectric reduction often seen at 2-D electrode surfaces for SAMs of this thickness.[35] These curves do not show resistances at low frequencies because redox active molecules that could transfer charge with the gold electrode were not employed here. Collectively, these results indicate that the equivalent circuit for the SAM-functionalized and unfunctionalized membrane can be represented simply by a solution resistance in series with an interfacial capacitance (C_i), which is affected by the presence of a SAM deposited within the membrane. Fits to these spectra for this simple equivalent circuit are shown in the curves of Figure 4.7a. Figure 4.7a also shows three other impedance spectra where pNBF6 has been grown only in the NPGL region of an NPGL/alumina composite membrane, only in the alumina region of an alumina membrane (no NPGL), or throughout the membrane in both the alumina and the NPGL regions of a composite membrane. The equivalent circuit would now contain terms representing the membrane modification (Figure 4.7b), including the overall membrane capacitance (C_{mem}), the resistance due to polymer grown in the gold region ($R_{Au\text{-}film}$), as well as a constant phase element (CPE_{Al}) and resistance (R_{pore}) for polymer grown within and from the alumina membrane. The membrane where pNBF6 was grown only in the NPGL region exhibits a capacitance (C_{mem}) at highest frequencies and a constant resistance ($R_{Au\text{-}film}$) of ~10^5 Ω•cm^2 over most of the frequency range. C_{mem} and $R_{Au\text{-}film}$ are attributed to the pNBF6 grown within the NPGL as well as the pNBF6 that grows atop the NPGL membrane, as shown in the SEM image in Figure 4.5d. From the simple behavior of the impedance spectrum, we conclude that the impedance components due to C_{mem} and $R_{Au\text{-}film}$ from pNBF6 growth dominate all other impedances in the spectrum. Thus, our equivalent circuit for this particular membrane focuses only on the impedances due to the functionalized membrane, C_{mem} and $R_{Au\text{-}film}$, which are in parallel.

When pNBF6 is grown only within the alumina membrane, the spectrum exhibits three distinct regions (Figure 4.7a). At the very highest frequencies, the slight flattening of the spectrum indicates a resistance that is ~10 fold larger than the R_s measured for the unfunctionalized membrane, which is ascribed to a combination of R_s and the resistance due to the overgrown pNBF6 film on the outlet side of the alumina membrane, termed $R_{Al\text{-}film}$. At low frequencies, the large resistance ($10^{6.5}$ Ω•cm^2) corresponds to the pNBF6 film grown within the alumina membrane as well as the overgrowth on the filtration (inlet) side of the membrane, where the pores are smaller, to produce a denser polymer film within the pores as well as a thicker overgrowth, referred to as R_{pore}. In comparing spectra for pNBF6 grown only within alumina to that grown only within NPGL, the R_{pore} due to pNBF6 growth in alumina is 50-fold greater than the $R_{Au\text{-}film}$ due to growth in gold, which is reasonable considering the 600-fold greater thickness of the alumina membrane (60 μm) versus NPGL (100 nm). Connecting those regions at intermediate frequencies is a capacitive region that corresponds to the dielectric properties of the pNBF6-functionalized alumina membrane. The lower capacitive impedance for alumina at high frequencies as compared to pNBF6 grown only in NPGL is consistent with solution penetration into the alumina membrane to greatly increase the effective dielectric constant. Further support for solution penetration is derived from the fact that the intermediate region cannot be fit with an ideal capacitor but rather a constant phase element (CPE_{Al}) that accounts for heterogeneity.[36]

The final spectrum of interest in Figure 4.7a corresponds to the case where pNBF6 is grown both within the alumina and the NPGL regions of the composite membrane. This spectrum exhibits two *RC* time constants and nearly matches the addition of the two spectra for the above cases where pNBF6 is grown in only the NPGL and only the alumina. This approximate matching of the actual spectrum with the added spectra of the controls reinforces the assignment of equivalent circuit components and provides physical insight toward ion penetration within the pNBF6-functionalized composite membrane. The spectrum was fit with the equivalent circuit shown in Figure 4.7b that comprises the components identified when describing the above controls. At high frequencies, we observe the *RC* time constant corresponding to the total membrane capacitance (C_{mem}) and the resistance due to polymer grown from and within NPGL ($R_{Au\text{-}film}$), and at intermediate to lower frequencies we observe the time constant for the polymer-functionalized alumina. From the values derived from this equivalent circuit in Table 4.2, we conclude that the larger real impedance in this composite membrane is due to the pNBF6 grown throughout the alumina but that the pNBF6-modified NPGL provides high impedance at high frequencies where the timescale for permeation is short.

To investigate the effect of polymerization time, Figure 4.7c shows representative Bode plots for the control SAM and pNBF6 films polymerized for 1 and 5 min. These films clearly exhibit higher impedance than that of the control SAM at all frequencies. As shown in Figure 4.6d, a period of 5 min of polymerization creates a film that completely fills the pores and covers the entire surface of the NPGL, whereas a 1 min period (see Figure 4.6b) forms a film on the NPGL ligands but does not seal the pores entirely. Despite the difference in growth extent on NPGL, both the 1 and 5 min pNBF6 films exhibit a similar impedance response at high frequencies. This behavior in impedance suggests that 1 min of polymerization is enough time to create a film to fill the volume of the pores and affect ion transport. A major dissimilarity in the performance of these pNBF6 films as a barrier is seen at intermediate and low frequencies, where the 5 min pNBF6 film offers a superior barrier to ion transport. From Figure 4.7a, the impedance contribution of the alumina substrate corresponds to this low to intermediate range in frequency. Therefore, 1 min of polymerization is not sufficient to fill the pores of the alumina. As a consequence, the resistance of the 1 min film at low frequencies is at least an order of magnitude lower than that of a 5 min film. Table 4.2 shows a summary of film resistance and film capacitance for these fluorinated polymer films, which quantitatively shows that the blocking nature of these pNBF6 films progressively improves as polymerization time increases.

Table 4.2. Impedance properties of the pNBF6 films polymerized within NPGL/alumina, NPGL, and alumina from a 0.05 M monomer solution. Experiments were done in a 0.1 M NaTFA solution.

Sample	Polym. time (min)	Log $R_{Au\text{-}film}$ ($\Omega \cdot cm^2$)	C_{mem} (nF/cm^2)	Log R_{pore} ($\Omega \cdot cm^2$)	CPE_{Al} ($\mu S \cdot s^{\alpha}$)	α	W ($\mu S \cdot s^{0.5}$)
SAM/NPGL/alumina	0	–	–	–	29.3 ± 1.2	0.91	–
pNBF6/alumina[a]	5	–	–	6.68 ± 0.01	0.010 ± 0.001	0.94	–
pNBF6/NPGL[a]	5	4.59 ± 0.07	0.57 ± 0.17	–	–	–	56.3
pNBF6/NPGL/alumina	5	5.20 ± 0.13	0.42 ± 0.04	7.14 ± 0.07	0.030 ± 0.001	0.78	–
	1	4.89 ± 0.02	0.48 ± 0.01	5.72 ± 0.02	0.68 ± 0.03	0.43	–

a. Selectively grown on this substrate.

Effect of Sulfonation of pNBF6 on the Performance of the Composite Membrane

Figure 4.8a shows representative Bode plots taken in the presence of a 0.1 M NaTFA solution for pNBF6 films grown on the NPGL/alumina assembly for 1 and 5 min before and after 1 h of sulfonation. In both cases, impedance spectra exhibit a substantial reduction, indicating that ion transport through the composite membrane is significantly enhanced. Moreover, the spectrum for the sulfonated pNBF6 film grown for 1 min begins to approach that of the control SAM at low and high frequency. Table 4.3, for example, shows that R_{pore} for the 1 and 5 min pNBF6 films decreased by 40 and 67 fold, respectively, after sulfonation. These results suggest a significantly greater penetration of aqueous solution through the membrane. The considerable decrease in impedance is consistent with sulfonation of chain unsaturation in the polymer backbone to yield sulfonate and hydroxyl groups, as we and others have shown for 2-D films.[29,37,38] Upon sulfonation of the pNBF6 films, water and hexadecane contact angles exhibit a slight decrease, indicating that the surfaces are still hydrophobic and oleophobic and contain predominantly $-CF_2-$ and $-CF_3$ groups.

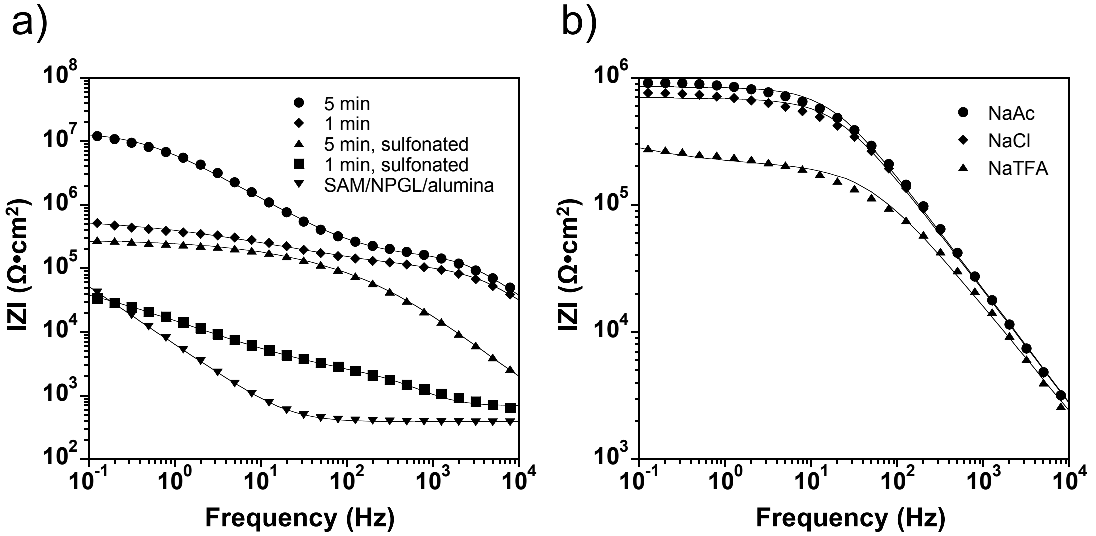

Figure 4.8. a) Electrochemical impedance spectra collected for the control SAM and pNBF6 films grown for 1 or 5 min, as indicated, before and after 1 h of sulfonation. Electrolyte solution consists of a 0.1 M aqueous solution of NaTFA. b) EIS spectra for a pNBF6 film grown for 5 min after 1 h of sulfonation. Three different 0.1 M electrolyte solutions, namely, NaAc, NaCl, and NaTFA were used. Solid lines indicate fits of the data using an appropriate equivalent circuit model.

Figure 4.8b shows impedance spectra of the anion selectivity for a 5 min pNBF6 film after sulfonation. Selectivity toward NaTFA over the other salts is evidenced by a 3 – 4 fold lower film resistance (see Table 4.3). This low impedance corroborates the importance of the chemical affinity of the solute for the polymer. Despite the fact that chloride is the smallest anion among the three salts, its spectrum exhibits higher impedance than that of the largest trifluoroacetate (TFA) anion over the entire frequency range. Similarly, the impedance response for the acetate anion is higher than that of the sodium TFA salt. Such specific impedance responses may be explained on the basis that the TFA anion exhibits a higher chemical affinity for the polymer film than do the other two species, and therefore, it permeates more readily. The permeability (*P*) of these solutes in the polymer matrix depends on their diffusion coefficient (*D*) in the membrane and partition coefficient (*K*) from the aqueous phase into the membrane:[8]

$$P = D \times K \qquad (4.1)$$

In general, the diffusion coefficient for large molecules is lower than that of small molecules, and for this reason the diffusivity of NaTFA should be lower than that of the two other salts due to the large size of the anion. For example, the TFA anion has a 45% greater van der Waals volume than the Ac anion.[38,39] Accordingly, NaTFA would not be expected to permeate as rapidly as NaAc or NaCl. However, permeation of the fluorinated salt is higher than that of the two other solutes as suggested by the EIS spectrum in Figure 4.8b, based on its higher capacitance and lower resistance, indicating that the solubility of the TFA anion is a key parameter in this case. The fact that the surface of the pNBF6 film grown on the NPGL-coated alumina is dominated by $–CF_2–$ and $–CF_3$ groups promotes partitioning of the TFA anion into the membrane and, in turn, facilitates the permeation of the salt, as compared to the smaller non-fluorinated anions. This result is consistent with findings by other groups. Goss et al.[40] demonstrated that fluorinated solutes exhibit smaller van der Waals interactions per molecular contact area than other organic compounds of similar size, and as a consequence, partitioning of the former into fluorous media is more prevalent than that of the latter. Recently, Zhang et al.[41] showed that replacement of a hydrogen atom by a fluorine atom in a solute, increases the partition coefficient into fluorous media to greater extent than it decreases the diffusion coefficient of the solute. This was evidenced by the greater permeability exhibited by species with higher molar mass/critical volumes when compared to those of lower molar mass/critical volumes through a highly fluorinated membrane.

Table 4.3. Impedance properties and contact angles of pNBF6 films before and after 1 h sulfonation.

Sample	Poly. time (min)	Salt	Log $R_{\text{Au-film}}$ (Ω•cm^2)	C_{mem} (nF/cm^2)	Log R_{pore} (Ω•cm^2)	CPE_{Al} (μS•s$^{\alpha}$)	α	W (μS•s$^{0.5}$)	Contact angle (deg)	
									Water	HD
									θ_A	θ_A
SAM/NPGL/ alumina	0	NaTFA	–	–	–	29.3 ± 1.2	0.91		56 ± 1	< 15
pNBF6/NPGL/ alumina	1	NaTFA	4.89 ± 0.02	0.48 ± 0.01	5.72 ± 0.02	0.68 ± 0.03	0.43		121 ± 2	69 ± 2
Sulf-pNBF6/NPGL/ alumina	1	NaTFA	–	–	4.11 ± 0.04	26.1 ± 2.5	0.41	5.41	116 ± 1	66 ± 2
pNBF6/NPGL/ alumina	5	NaTFA	5.20 ± 0.13	0.42 ± 0.04	7.14 ± 0.07	0.030 ± 0.001	0.78		129 ± 2	74 ± 2
Sulf-pNBF6/NPGL/ alumina	5	NaTFA	–	–	5.31± 0.05	0.040 ± 0.001	0.83	12.98	121 ± 1	71 ± 1
Sulf-pNBF6/NPGL/ alumina	5	NaCl	–	–	5.84 ± 0.04	0.020 ± 0.001	0.88			
Sulf-pNBF6/NPGL/ alumina	5	NaAc	–	–	5.92 ± 0.04	0.020 ± 0.002	0.89			

Conclusions

The integration of NPGL with alumina supports to form a porous composite membrane has been successfully achieved. The use of silane chemistry provided functionalization and subsequent integration of the alumina membrane with NPGL. SI–ROMP facilitated the incorporation of a partially fluorinated thin film into the porous NPGL-alumina assembly. SEM images and contact angle measurements confirm formation of the thin polymer film. The porous microstructure of the NPGL/alumina assembly as well as the ion transport properties of the membrane can be altered by regulating the polymerization time of the NBF6 monomer. Conformal pNBF6 films polymerized for 5 min exhibit impedance on the order of 1×10^7 Ω•cm^2 for sodium trifluoroacetate, indicating that the composite membrane has ultralow pinhole defect density. In addition, EIS characterization shows that ion transport through the composite membrane is substantially enhanced after sulfonation. The fluorinated nature of the polymer thin film renders the membrane selective towards ions with similar chemical properties. For this reason, the sulfonated membrane is more permeable to the ion transport of sodium trifluoroacetate than it is to sodium chloride or sodium acetate.

References

(1) Loeb, S.; Sourirajan, S. Sea Water Demineralization by Means of an Osmotic Membrane. In *Advances in Chemistry Series*; Saline Water Conversion-II: **1963**; Vol. 38, p 117-132.

(2) Baker, R. *Membrane Technology and Applications*; McGraw-Hill: New York, **2002**, p 2.

(3) Seader, J. D.; Henley, E. J. *Separation Process Principles*; John Wiley & Sons, Inc., **2006**, p 493.

(4) Che, G. L.; Lakshmi, B. B.; Fisher, E. R.; Martin, C. R. Carbon Nanotubule Membranes for Electrochemical Energy Storage and Production. *Nature* **1998,** 393, 346-349.

(5) Martin, C. R. Membrane-Based Synthesis of Nanomaterials. *Chemistry of Materials* **1996,** 8, 1739-1746.

(6) Balachandra, A. M.; Baker, G. L.; Bruening, M. L. Preparation of Composite Membranes by Atom Transfer Radical Polymerization Initiated from a Porous Support. *J. Membr. Sci.* **2003,** 227, 1-14.

(7) Bai, D.; Elliott, S. M.; Jennings, G. K. pH-Responsive Membrane Skins by Surface-Catalyzed Polymerization. *Chemistry of Materials* **2006,** 18, 5167-5169.

(8) Velleman, L.; Triani, G.; Evans, P. J.; Shapter, J. G.; Losic, D. Structural and Chemical Modification of Porous Alumina Membranes. *Microporous and Mesoporous Materials* **2009,** 126, 87-94.

(9) Cheow, P.-S.; Liu, L.; Toh, C.-S. Grafting of Nanoporous Alumina Membranes and Films with Organic Acids. *Surface and Interface Analysis* **2007,** 39, 601-610.

(10) Hanaoka, T. A.; Heilmann, A.; Kroll, M.; Kormann, H. P.; Sawitowski, T.; Schmid, G.; Jutzi, P.; Klipp, A.; Kreibig, U.; Neuendorf, R. Alumina Membranes - Templates for Novel Nanocomposites. *Applied Organometallic Chemistry* **1998,** 12, 367-373.

(11) Ding, Y.; Kim, Y. J.; Erlebacher, J. Nanoporous Gold Leaf: "Ancient Technology"/Advanced Material. *Advanced Materials* **2004,** 16, 1897-1900.

(12) Ciesielski, P. N.; Scott, A. M.; Faulkner, C. J.; Berron, B. J.; Cliffel, D. E.; Jennings, G. K. Functionalized Nanoporous Gold Leaf Electrode Films for the Immobilization of Photosystem I. *ACS Nano* **2008,** 2, 2465-2472.

(13) Kramer, D.; Viswanath, R. N.; Weissmuller, J. Surface-Stress Induced Macroscopic Bending of Nanoporous Gold Cantilevers. *Nano Letters* **2004,** 4, 793-796.

(14) Liu, Z.; Du, J.; Qiu, C.; Huang, L.; Ma, H.; Shen, D.; Ding, Y. Electrochemical Sensor for Detection of p-Nitrophenol Based on Nanoporous Gold. *Electrochemistry Communications* **2009,** 11, 1365-1368.

(15) Zeis, R.; Lei, T.; Sieradzki, K.; Snyder, J.; Erlebacher, J. Catalytic Reduction of Oxygen and Hydrogen Peroxide by Nanoporous Gold. *Journal of Catalysis* **2008,** 253, 132-138.

(16) Liu, P.; Ge, X.; Wang, R.; Ma, H.; Ding, Y. Facile Fabrication of Ultrathin Pt Overlayers onto Nanoporous Metal Membranes via Repeated Cu UPD and in Situ Redox Replacement Reaction. *Langmuir* **2009,** 25, 561-567.

(17) Qiu, H.-J.; Zhou, G.-P.; Ji, G.-L.; Zhang, Y.; Huang, X.-R.; Ding, Y. A Novel Nanoporous Gold Modified Electrode for the Selective Determination of Dopamine in the Presence of Ascorbic Acid. *Colloids and Surfaces B-Biointerfaces* **2009,** 69, 105-108.

(18) Lux, K. W.; Rodriguez, K. J. Template Synthesis of Arrays of Nano Fuel Cells. *Nano Letters* **2006,** 6, 288-295.

(19) Liu, L.; Pippel, E.; Scholz, R.; Goesele, U. Nanoporous Pt-Co Alloy Nanowires: Fabrication, Characterization, and Electrocatalytic Properties. *Nano Letters* **2009,** 9, 4352-4358.

(20) Liu, L.; Lee, W.; Huang, Z.; Scholz, R.; Goesele, U. Fabrication and Characterization of a Flow-Through Nanoporous Gold Nanowire/AAO Composite Membrane. *Nanotechnology* **2008,** 19, 335604.

(21) Dotzauer, D. M.; Dai, J.; Sun, L.; Bruening, M. L. Catalytic Membranes Prepared Using Layer-by-Layer Adsorption of Polyelectrolyte/Metal Nanoparticle Films in Porous Supports. *Nano Letters* **2006,** 6, 2268-2272.

(22) Qian, L.; Shen, W.; Shen, B.; Qin, G. W.; Das, B. Nanoporous Gold-Alumina Core-Shell Films with Tunable Optical Properties. *Nanotechnology* **2010,** 21, 305705.

(23) Jennings, G. K.; Brantley, E. L. Physicochemical Properties of Surface-Initiated Polymer Films in the Modification and Processing of Materials. *Adv. Mater.* **2004,** 16, 1983-1994.

(24) Slugovc, C. The Ring Opening Metathesis Polymerisation Toolbox. *Macromol. Rapid Commun.* **2004,** 25, 1283-1297.

(25) Buchmeiser, M. R. Metathesis Polymerization to and from Surfaces. In *Surface-Initiated Polymerization I*; Jordan, R., Ed.; Springer-Verlag Berlin: Berlin, **2006**; Vol. 197, p 137-171.

(26) Rutenberg, I. M.; Scherman, O. A.; Grubbs, R. H.; Jiang, W.; Garfunkel, E.; Bao, Z. Synthesis of Polymer Dielectric Layers for Organic Thin Film Transistors via Surface-Initiated Ring-Opening Metathesis Polymerization. *J. Am. Chem. Soc.* **2004,** 126, 4062-4063.

(27) Faulkner, C. J.; Fischer, R. E.; Jennings, G. K. Surface-Initiated Polymerization of 5-(Perfluoro-n-alkyl)norbornenes from Gold Substrates. *Macromolecules* **2010,** 43, 1203-1209.

(28) Faulkner, C. J.; Payne, P. A.; Jennings, G. K. Surface-Initiated Ring-Opening Metathesis Polymerization of 5-(perfluorohexyl)norbornene on Carbon Paper Electrodes. *J. Colloid Interface Sci.* **2010,** 351, 248-253.

(29) Berron, B. J.; Payne, P. A.; Jennings, G. K. Sulfonation of Surface-Initiated Polynorbornene Films. *Industrial & Engineering Chemistry Research* **2008,** 47, 7707-7714.

(30) Berron, B. J.; Faulkner, C. J.; Fischer, R. E.; Payne, A.; Jennings, G. K. Surface-Initiated Growth of Ionomer Films from Pt-Modified Gold Electrodes. *Langmuir* **2009,** 25, 12721-12728.

(31) Berron, B. J.; Graybill, E. P.; Jennings, G. K. Growth and Structure of Surface-Initiated Poly(n-alkylnorbornene) Films. *Langmuir* **2007,** 23, 11651-11655.

(32) Bain, C. D.; Troughton, E. B.; Tao, Y. T.; Evall, J.; Whitesides, G. M.; Nuzzo, R. G. Formation of Monolayer Films by the Spontaneous Assembly of Organic Thiols from Solution onto Gold. *J. Am. Chem. Soc.* **1989,** 111, 321-335.

(33) Brantley, E. L.; Jennings, G. K. Fluorinated Polymer Films from Acylation of ATRP Surface-Initiated Poly(hydroxyethyl methacrylate). *Macromolecules* **2004,** 37, 1476-1483.

(34) Fukushima, H.; Seki, S.; Nishikawa, T.; Takiguchi, H.; Tamada, K.; Abe, K.; Colorado, R.; Graupe, M.; Shmakova, O. E.; Lee, T. R. Microstructure, Wettability, and Thermal Stability of Semifluorinated Self-Assembled Monolayers (SAMs) on Gold. *J. Phys. Chem. B* **2000,** 104, 7417-7423.

(35) Porter, M. D.; Bright, T. B.; Allara, D. L.; Chidsey, C. E. D. Spontaneously Organized Molecular Assemblies. 4. Structural Characterization of Normal-Alkyl Thiol Monolayers on Gold by Optical Ellipsometry, Infrared-Spectroscopy, and Electrochemistry. *Journal of the American Chemical Society* **1987,** 109, 3559-3568.

(36) Orazem, M. T., B. *Electrochemical Impedance Spectroscopy*; John Wiley & Sons, Inc., **2008**.

(37) Eckenrode, H. M.; Dai, H.-L. Nonlinear Optical Probe of Biopolymer Adsorption on Colloidal Particle Surface: Poly-l-lysine on Polystyrene Sulfate Microspheres. *Langmuir* **2004,** 20, 9202-9209.

(38) Seebach, D. Organic Synthesis - Where now? *Angewandte Chemie International Edition* **1990,** 29, 1320 - 1367.

(39) Zhao, Y. H.; Abraham, M. H.; Zissimos, A. M. Fast Calculation of van der Waals Volume as a Sum of Atomic and Bond Contributions and Its Application to Drug Compounds. *The Journal of Organic Chemistry* **2003,** 68, 7368-7373.

(40) Goss, K.-U.; Bronner, G. What Is So Special about the Sorption Behavior of Highly Fluorinated Compounds? *The Journal of Physical Chemistry A* **2006,** 110, 9518-9522.

(41) Zhang, H.; Hussam, A.; Weber, S. G. Properties and Transport Behavior of Perfluorotripentylamine (FC-70)-Doped Amorphous Teflon AF 2400 Films. *Journal of the American Chemical Society* **2010,** 132, 17867-17879.

CHAPTER V

AMPLIFICATION OF SURFACE-INITIATED RING-OPENING METATHESIS POLYMERIZATION OF 5-(PERFLUORO-N-ALKYL)NORBORNENES BY MACROINITIATION

Adapted with permission from Escobar, C. A.; Harl, R. R.; Maxwell, K. E.; Mahfuz, N. N.; Rogers, B. R.; Jennings, G. K. Amplification of Surface-Initiated Ring-Opening Metathesis Polymerization of 5-(Perfluoro-n-alkyl)norbornenes by Macroinitiation. Langmuir 2013, 29, 12560-12571. Copyright 2013 American Chemical Society.

Introduction

Surface-initiated polymerization (SIP) or "grafting from" approaches provide robust chemisorption, a vast range of available compositions and chemistries, tunable thicknesses, and the ability to conformally and uniformly coat planar and non-planar architectures.[1-3] A key limitation of SIP approaches in the application of coatings has been that, with a few exceptions,[4-6] the resulting films are too thin to offer the requisite protection and robustness. Thickness is an important parameter of coatings that enables improvement of the blocking properties and robustness of the film. For example, an increase in thickness translates into longer diffusion times, i.e., undesirable species would have to penetrate to a greater extent in order to reach the underlying surface.[7] Several research groups,[4,8] including ours,[6,9] have reported different polymerization strategies to grow polymer films exceeding 1 μm in thickness on a wide variety of substrates. However, reports on surface-initiated, fast-growing, partially fluorinated films of these thicknesses are scarce. In this connection, fluorinated and partially fluorinated polymers attract great technological interest because of their unique physicochemical properties, including excellent chemical resistance, high thermal stability, repellence towards water and oils, superior outdoor durability, and exceptional mechanical and thermal properties.[10] Accordingly, these polymers exhibit high performance in a wide range of applications, such as protective coatings,[11,12] membrane separations,[13,14] low surface-energy surfaces,[15,16] and electronics.[17,18] Therefore, the ability to combine the many practical benefits of SIP with new approaches to enable the routine production of coatings with thickness greater than 1 μm could have a profound impact in the area of specialty coatings.

Of the many classes of SIP, intense research over the past decade has led to the development and recognition of SI-ATRP and SI-ROMP as robust, versatile, and well-established techniques.[2,17,19,20] For example, SI-ATRP is widely used because it enables the preparation of a wide range of polymer brushes with diverse chemical functionality and controlled thickness from both flat and curved surfaces, and porous substrates.[2,21] Similarly, SI-ROMP stands out as a useful technique for synthesizing polymers with tailorable functionalities[22] to achieve attractive biological, electronic, and mechanical properties.[20] Most importantly, SI-ROMP provides fast polymerization rates, even at room temperature in ambient conditions, which result in the rapid growth of thick polymer films. Salient advantages of SI-ROMP include tolerance towards functional groups, preparation of high-molecular weight polymers, and preservation of the olefin functionality in the resulting polymer.[23] In this chapter, I report on the synergistic combination of SI-ATRP and SI-ROMP as a versatile method to grow exceptionally thick partially fluorinated surface-initiated polymer films.

Some of the thickest SIP films reported in the literature have been achieved by employing SI-ATRP or SI-ROMP polymerization techniques. For example, Huang et al.[8] extended the aqueous solution-phase ATRP method developed by Armes et al.[24] to SI-ATRP. They used a mixed halide initiation system comprised of CuCl and $CuBr_2$ to successfully and controllably grow poly(2-hydroxyl methacrylate) (PHEMA) films with thickness up to 700 nm in 12 h of polymerization time. In addition, the study demonstrated that the hydroxyl groups in the PHEMA films could be further derivatized, providing an opportunity to fine-tune the physicochemical properties of the polymer brushes. Similarly, Brantley et al.[25] and Saha et al.[26] have grown thick polymer films using SI-ATRP. The SI-ROMP of norbornene and its derivatives are among the thickest polymer films produced by an SIP technique.[27] For instance, Weck et al.[17] performed early work on employing SI-ROMP as an alternative technique to overcome the challenges that other SIP techniques faced at the time, such as side reactions and impurities on the surface, and were able to grow polymer brushes of substituted norbornenes on gold with thicknesses up to several hundreds of nanometers. In an effort to create covalently attached, organic overlayers on silicon (111) substrates, Juang et al.[18] combined a chlorination/alkylation process, in order to form catalyst-anchoring allyl groups on the silicon substrate, with SI-ROMP. As a result, electrically insulating polymer layers of polynorbornene with thicknesses of up to 5.5 μm were produced. Similarly, Rutenberg et al.[28] employed SI-ROMP to fabricate polymer dielectric layers for field effect transistors that exhibited a thickness of 1.2 μm. Recently, our group[16] reported on the formation of partially fluorinated films by means of SI-ROMP exhibiting critical surface tensions from 9 – 18 $mN{\bullet}m^{-1}$ and thicknesses in excess of 1 μm.

High grafting density is essential in the formation of thick surface-initiated polymer films.[29] Consequently, researchers have resorted to the use of macroinitiators as a tool to enhance grafting density.[3] This approach has been applied, in particular, in the formation of polymer films by SI-ATRP.[30] For example, Liu et al.[31] deposited poly(glycidyl methacrylate) onto silicon wafers followed by exposure to bromoacetic acid vapor to create a macroinitiator for subsequent SI-ATRP. As a result, the initiator surface density achieved by this method exceeded that reported for the self-assembled monolayers (SAMs) of ATRP initiators by a factor of ~ 13 (~ $40{\bullet}nm^{-2}$ for a 6-nm-thick macroinitiator vs. ~ $3{\bullet}nm^{-2}$ for a SAM). Investigations reporting on the use of macroinitiators in conjunction with SI-ROMP are scarce. In this regard, the work done by

Detrembleur and co-workers[4] and Voccia et al.[5] is worthy of mention. These groups successfully integrated electrografting[32,33] and SI-ROMP as a versatile approach to prepare dense polymer films on conducting substrates.

The efficiency and quality of fluorinated and partially fluorinated films, which often yield critical surface tensions as low or lower than fully fluorinated polymers because of the segregation of the fluorocarbon chains to the interface,[15,16] depend to a great extent on the deposition techniques used to create them. For example, conventional deposition methods based on physisorption give rise to weak interactions that undermine the adhesion between the film and the solid surface, rendering the films unstable.[15,16,34] Conversely, SIP is an ideal approach to avert such deficiency, as demonstrated by several groups.[35] Here, I describe the sequential use of two versatile SIP techniques, namely, SI-ATRP and SI-ROMP, in the preparation of thick partially fluorinated polymer films prepared from 5-(perfluoro-n-alkyl)norbornenes (NBFn), where n represents the number of carbons present in the fluorocarbon side chain, e.g., 4, 6, 8, and 10.

Experimental Methods

Polymerization

Two approaches were used to grow partially fluorinated polymer films from gold substrates, namely, initiation from a monolayer and initiation from a macroinitiator. In both cases, the films were grown from 0.05, 0.2, and 1 M monomer solutions and allowed to polymerize for 1, 5, and 15 min in each concentration. In the monolayer approach, the gold samples were exposed to a 1 mM ethanolic solution of 4-mercapto-1-butanol for at least 1 h to form a chemisorbed hydroxyl-terminated SAM. Afterwards, samples were rinsed in ethanol and dried in a stream of nitrogen. The dried substrates were exposed to a 5 mM solution of NBDAC in DCM for 30 min. Then, samples were rinsed with DCM and ethanol, and dried in a stream of nitrogen. These substrates were exposed to a 5 mM solution of Grubbs second-generation catalyst in DCM for 10 min. Upon removal from solution, samples were rinsed with DCM and immediately placed in a solution of NBFn (n = 4, 6, 8, 10) in DCM for 1, 5, or 15 min. After polymerization, samples were rinsed with DCM, ethanol, water, and dried in a stream of nitrogen.

In the macroinitiator approach, the gold substrates were sequentially exposed to two surface-initiated polymerization processes, specifically, SI-ATRP and SI-ROMP. SI-ATRP was performed to grow a PHEMA film, which, after modification, served as a macroinitiator layer for the SI-ROMP process. The procedure to grow PHEMA from the gold substrates is similar to that reported by Brantley et al.[25] Briefly, gold substrates were exposed to a 1 mM ethanolic solution of the disulfide ATRP initiator $(BrC(CH_3)_2COO(CH_2)_{11}S)_2$ for 24 h.[8,36] Afterward, these initiator-bearing samples were rinsed with ethanol, dried in a stream of nitrogen, and placed in vials sealed with rubber septa. These vials underwent a subsequent degassing and back-filling process with nitrogen. The polymerization mixture consisting of Cu^I/Cu^{II}/bpy (69 mM CuCl, 20 mM $CuBr_2$, 195 mM bpy) in a 50:50 v:v water/HEMA solution, contained in a Schlenk flask sealed with a rubber septum, was exposed to a degassing process by performing three freeze-pump-thaw cycles. Subsequently, the mixture was transferred via cannula into the vials containing the ATRP-active substrates. After 12 h of polymerization at room temperature, samples were rinsed with water and DMF and dried with nitrogen.

To perform the SI-ROMP process, the PHEMA samples were subsequently exposed to a 20 mM NBDAC solution in DMF for 3 h and were thoroughly rinsed with DMF and ethanol after removal from solution and dried in a stream of nitrogen. In a similar manner to that in the monolayer initiation process, samples were exposed to a 5 mM solution of Grubbs second-generation catalyst in DCM for 10 min. Subsequently, samples were thoroughly rinsed with DCM and immediately placed in a solution of NBFn (n = 4, 6, 8, 10) in DCM for 1, 5, or 15 min. After polymerization, the samples were rinsed with DCM, ethanol, water, and dried with a stream of nitrogen. All SI-ROMP reactions took place under ambient conditions, unless otherwise indicated.

Results and Discussion

The polymerization of partially fluorinated films from gold-coated substrates was achieved via monolayer initiation and macroinitiation. In the former process,[16] exposure of a SAM prepared from 4-mercapto-1-butanol on gold to an NBDAC solution led to the coupling of the norbornenyl group to the underlying hydroxyl monolayer via ester linkages. Subsequent exposure to a Grubbs 2nd generation catalyst solution rendered the surface active for SI–ROMP.[23] In the latter approach, depicted in Scheme 5.1, the gold-coated substrates underwent an SI-ATRP process to grow a PHEMA macroinitiator. The use of PHEMA as a macroinitiator is advantageous, as the hydroxyl groups present in the side chain of each repeating unit can be further derivatized to introduce initiating groups from which other polymerization processes can take place.[8,25] In this case, some of the hydroxyl groups in the PHEMA film were acylated by exposure to a 20 mM solution of NBDAC in DMF to produce norbornenyl groups throughout the film. In contrast to the monolayer approach, DMF replaced DCM as the solvent in the acylation process because DMF swells PHEMA for attachment of the norbornenyl groups. For example, the solubility parameter, δ, for PHEMA is ~ 27 $(\mathrm{MPa})^{1/2}$,[37] whereas the values of δ for DMF and DCM are 24.8 and 19.8 $(\mathrm{MPa})^{1/2}$, respectively.[38] This proximity in solubility parameters promotes stretching of the surface-bound polymer chains away from the surface as opposed to adopting a collapsed coil regime,[39] rendering the hydroxyl groups more accessible for further reaction. After the acylation process, the norbornenyl-decorated PHEMA films were exposed to a solution containing Grubbs 2nd generation catalyst, which becomes immobilized by breaking and reforming the olefin double bond of the norbornenyl ring and consequently opening it.[28] Through this modification, the PHEMA macroinitiator becomes active for SI-ROMP. Subsequent immersion of the ROMP-active substrates in solutions of NBFn in DCM resulted in the growth of partially fluorinated polymer films.

Macroinitiator Characterization

X-ray Photoelectron Spectroscopy (XPS)

The use of XPS to examine the composition of the outer ~10 nm of the PHEMA film before and after the acylation and activation processes provided a quantitative assessment of the extent of conversion of the side chain hydroxyl groups in PHEMA with NBDAC, as well as the degree of attachment of the Ru-based catalyst to the norbornenyl groups of the acylated PHEMA films.

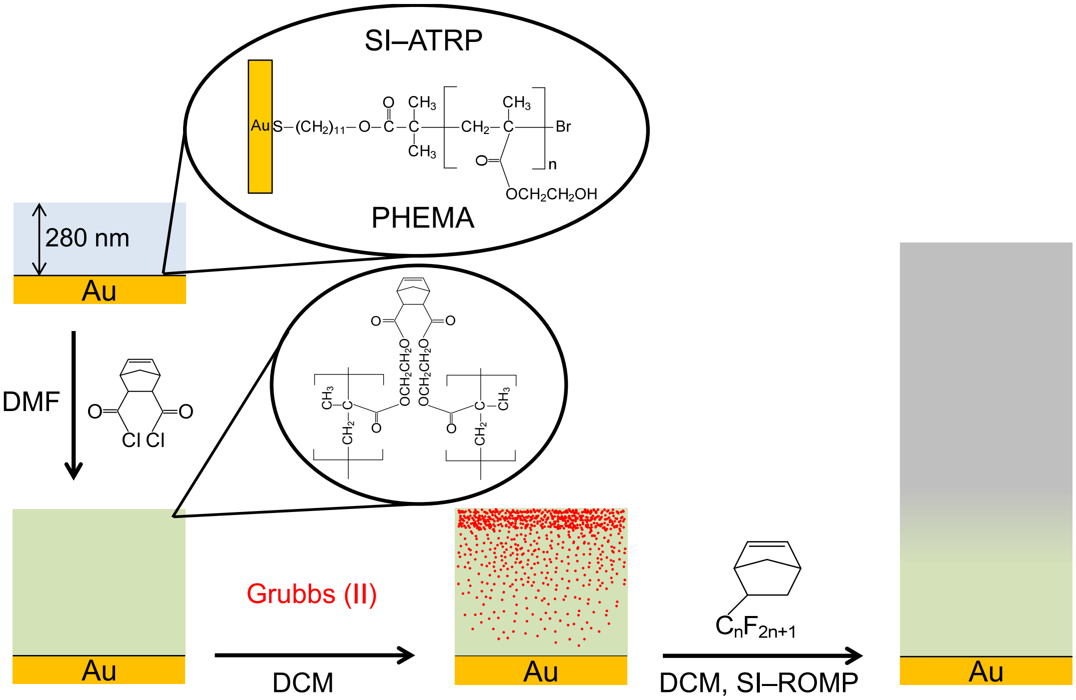

Scheme 5.1. Polymerization process of partially fluorinated films initiated from a PHEMA macroinitiator.

The XPS survey spectrum in Figure 5.1a shows the two major binding energy peaks of a PHEMA film: O 1s at 532 eV and C 1s at 284.8 eV. Figure 5.1b shows the high resolution C 1s spectrum of the PHEMA film deconvoluted into three peak components representing the different carbon bonds in PHEMA: C–C at 284.8 eV, C–O at 286.3 eV, and the carbonyl carbon (O–C=O) at 288.7 eV.[40] Figure 5.1c shows the survey spectrum of PHEMA upon acylation, in which, besides the O 1s and C 1s peaks at 532 and 284.8 eV, respectively, an emission peak appears at 200 eV. This new peak, attributed to the binding energy of Cl 2p,[40] is indicative of a single ester bond between the hydroxyl groups of PHEMA and NBDAC (vide infra). The deconvoluted C 1s core-level spectrum of the modified PHEMA shown in Figure 5.1d exhibits a weakened C–O peak at 286.4 eV, consistent with a decrease in the number of C–OH bonds after the acylation reaction. Figure 5.1e shows a survey spectrum of the modified PHEMA film after exposure to the Ru catalyst solution, in which, in addition to the O 1s (532 eV), C 1s (284.4 eV), and Cl 2p (200 eV) peaks, the Ru $3p_{3/2}$ and N 1s peaks appear at 462 and 400 eV, respectively, to signal the successful incorporation of the catalyst. The N 1s signal arises as a consequence of the presence of nitrogen atoms in the N-heterocyclic carbene ligand of the catalyst. Moreover, the high resolution C 1s spectrum in Figure 5.1f shows a Ru transition peak, assigned as Ru $3d_{5/2}$, at ~ 280 eV.

Table 5.1 summarizes the measured percentage of C 1s bonding states for PHEMA films in each of the modification steps prior to SI-ROMP. The PHEMA repeat unit contains 3 C-C bonds, one C–O bond, one C–OH bond, and one O–C=O bond, summing to a theoretical C 1s bonding composition of 50% C–C, 33.3% C–O/C–OH, and 16.7% O–C=O, which matches well with measured values. The increasing trend in C–C bonding is consistent with the introduction of hydrocarbon molecules into the unmodified PHEMA film, such as the norbornenyl di-acid chloride and the N-heterocyclic carbene ligand of the catalyst. The decreasing percentage in C–O bonding is consistent with the decrease of the C–O peak in Figure 5.1d, which is ascribed to the reaction of the hydroxyl groups with NBDAC. Similarly, the slight increase in O–C=O bonding may be attributed to the addition of ester groups present in NBDAC. The XPS-determined atomic composition and percentage of the different C 1s bonding states of the acylated PHEMA film on Table 5.1, serve to estimate the extent of conversion of the hydroxyl groups in PHEMA. The estimation assumes that the detected chlorine remains from a monodentate reaction between NBDAC and a hydroxyl group of PHEMA. Accordingly, the calculation suggests that 5% of the hydroxyl termini in PHEMA formed a single ester bond, 33% formed two ester bonds, and 62% were unreacted. In addition, Table 5.1 shows the atomic compositions of the PHEMA films after each modification step. Comparison of the calculated atomic composition and percentages of C 1s bonding states versus those obtained experimentally for the acylated PHEMA are shown in Table A.1 (see APPENDIX A).

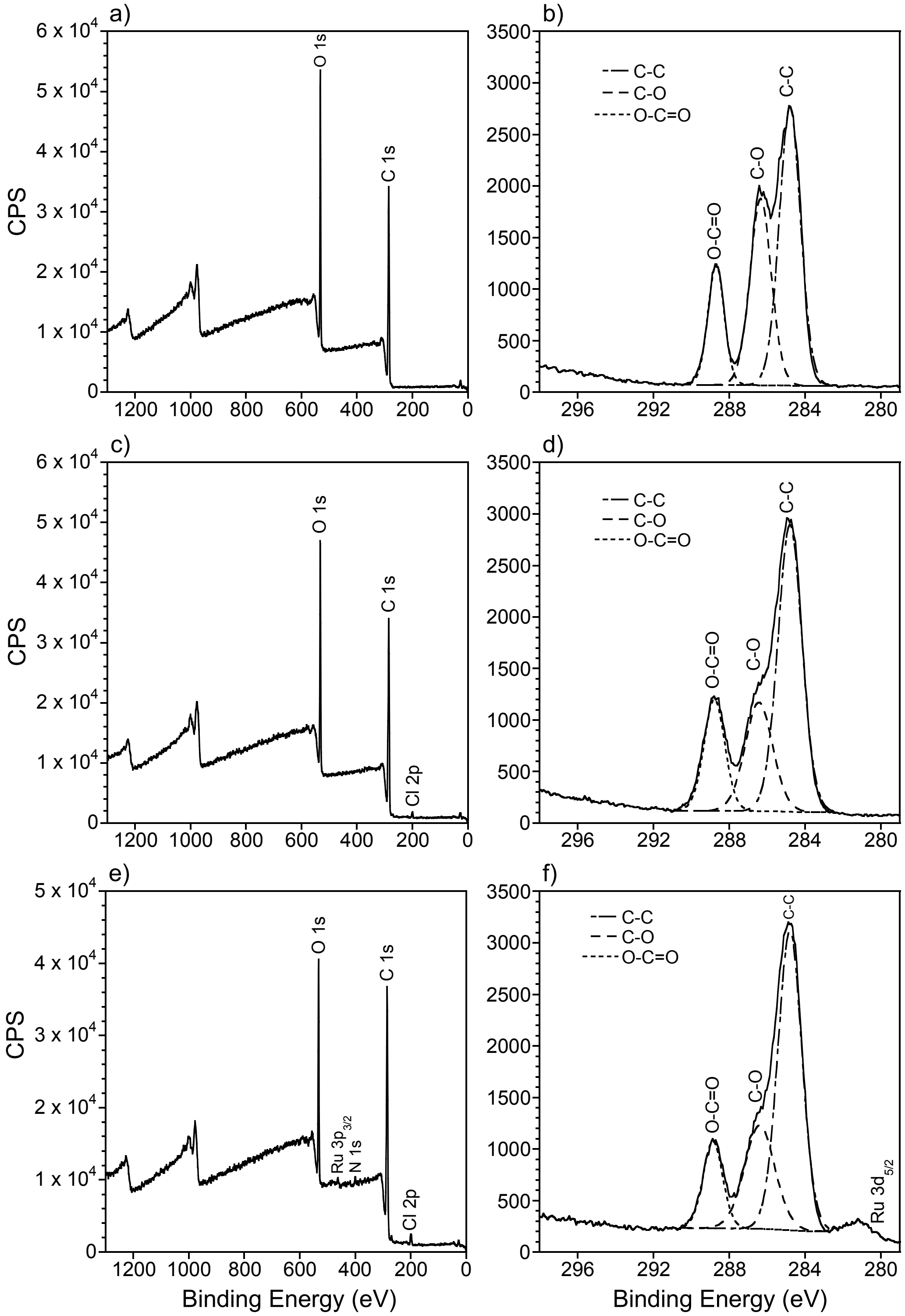

Figure 5.1. XPS survey scans of a) PHEMA, c) acylated PHEMA, and e) activated PHEMA. XPS high resolution scans of C 1s core levels for b) PHEMA, d) acylated PHEMA, and f) activated PHEMA.

Table 5.1. Measured percentage of C 1s bonding states and atomic compositions for PHEMA films before and after acylation, and after activation.

Sample	C 1s bonding (%)			Atomic Compositions				
	C–C	C–O	O–C=O	C	O	Cl	N	Ru
PHEMA	49.9	33.6	16.5	65.6	34.4	0	0	0
PHEMA, NBDAC	56.8	24.7	18.5	68.3	31.3	0.4	0	0
PHEMA, NBDAC, Ru	59.7	26.1	14.2	71	26.3	1	1.2	0.5

The extent of the reaction between the catalyst and the immobilized norbornenyl groups was determined by the Ru atomic composition observed after exposure of the modified-PHEMA film to the catalyst solution. Table 5.2 presents a comparison of the calculated and measured compositions of the acylated PHEMA film after exposure to a 5 mM DCM solution of Grubbs second-generation catalyst for 10 min. The values for the NBDAC attachment to PHEMA, summarized in Table A.1 in APPENDIX A, were used as the potential number of bonding sites for the catalyst molecule. In this case, the calculated Ru atomic composition was fit such that it matched the experimental counterpart. In addition, the calculated values were estimated by adding 27 carbons, 2 chlorines, 1 ruthenium, and 2 nitrogens for every catalyst molecule attached. Results from this calculation suggest that 7% (± 1%) of the norbornenyl groups reacted with a catalyst molecule. The atomic composition of Ru in the norbornenyl-decorated SAM, by contrast, could not be determined due to lack of Ru signal-to-noise in XPS. This outcome suggests that the amount of immobilized Ru molecules on the SAM is below the detection limit of approximately ± 0.1 at%.

Table 5.2. Calculated and experimental atomic compositions of the acylated PHEMA after exposure to the catalyst solution. Calculations were obtained by an atom balance based on the measured Ru composition.

Sample: PHEMA, NBDAC, Ru	C	O	Cl	Ru	N
Calculation	72.0	25.1	1.4	0.5	1.0
Experimental	71.0	26.3	1.0	0.5	1.2

Angle resolved XPS (ARXPS) enables the inference of compositional changes with depth into the film, usually up to 10 nm below the surface. Data collected at lower take-off angles (defined with respect to the surface parallel) offer insight into the outermost surface composition, whereas data collected at higher angles provide information deeper into the film. In an attempt to characterize the depth distribution of Ru into the modified-PHEMA films, ARXPS data were collected from the modified-PHEMA sample exposed to the catalyst solution. Results shown in Table 5.3 suggest a higher concentration of the catalyst at the surface than in the bulk, as evidenced by the decrease in the atomic composition of Ru with an increase in take-off angle. Notably, the atomic composition of Ru remains constant for take-off angles above 60°. Such stable composition suggests that the initiator is bound within the film, at least to an extent equal to the maximum depth resolution of the technique. These results indicate that the anchoring of the catalyst is not limited to the outermost portion of the surface, as if this were the case, a continuous reduction of the atomic composition with increasing take-off angle would be expected.

Table 5.3. Atomic compositions of the activated PHEMA film determined from data collected using take off angles between 15° and 90° off surface parallel.

Angle (deg)	C	O	N	Ru	Cl
15	71.3	25.8	1.6	0.7	0.6
30	71.4	26.2	1.4	0.7	0.4
45	71.2	26.6	1.3	0.6	0.3
60	71.1	26.9	1.2	0.5	0.3
80	71.1	26.9	1.2	0.5	0.3
90	71.1	27.1	1.2	0.5	0.3

Rutherford Backscattering Spectrometry (RBS)

To quantitatively assess the areal density of Ru catalyst in the modified-PHEMA film, we characterized activated PHEMA films using RBS. A thinner gold layer (25 nm) was used for this characterization because a thicker one would result in a broad, intense substrate peak that would obscure the signal due to Ru. Figure 5.2a shows the RBS spectrum for an activated PHEMA film that clearly shows the silicon, chromium, gold, and ruthenium transitions, along with those of the elements comprising the PHEMA film (carbon and oxygen). The Ru peak was fit with a single Gaussian peak, and by using a secondary Bi implanted standard (see Chapter III) and the area of the Ru peak, the Ru areal density was estimated at ~3.7 × 10^{14} atoms•cm^{-2}. A thorough explanation of the common method to perform this calculation can be found elsewhere.[41] For comparison, the estimated coverage of a densely packed monolayer of this catalyst is equivalent to ~ 1.2 × 10^{14} molecules•cm^{-2} (see APPENDIX A). Further, because the coverage of the Ru catalyst is known to be less than 10% in previous studies based on monolayer initiation,[42] the use of a macroinitiator results in at least 30-times greater amounts of Ru catalyst bound per geometric area.

Thickness

Figure 5.2b shows the effect of the PHEMA thickness on the ultimate thickness of pNBF8 films, as measured by profilometry. The thickness of the resulting pNBF8 film increases as the thickness of PHEMA increases, but the thinnest PHEMA film was the most efficient initiator of pNBF8 films. For example, comparison of its thickness (~ 0.03 µm) to that of its corresponding pNBF8 film (1.9 ± 0.08 µm) shows that the pNBF8 film was 64 times thicker. By comparison, the thickness of pNBF8 films grown from PHEMA films ~ 0.09, 0.17, and 0.28 µm thick were thicker than their initiating films by factors of ~ 35, 20, and 15, respectively. This decreasing trend suggests that initiator bound at increasing depths below the activated PHEMA surface is less efficient in producing polymer, although the general increase in pNBF8 thickness with PHEMA thickness suggests that some initiator located more than 170 nm below the surface does contribute.

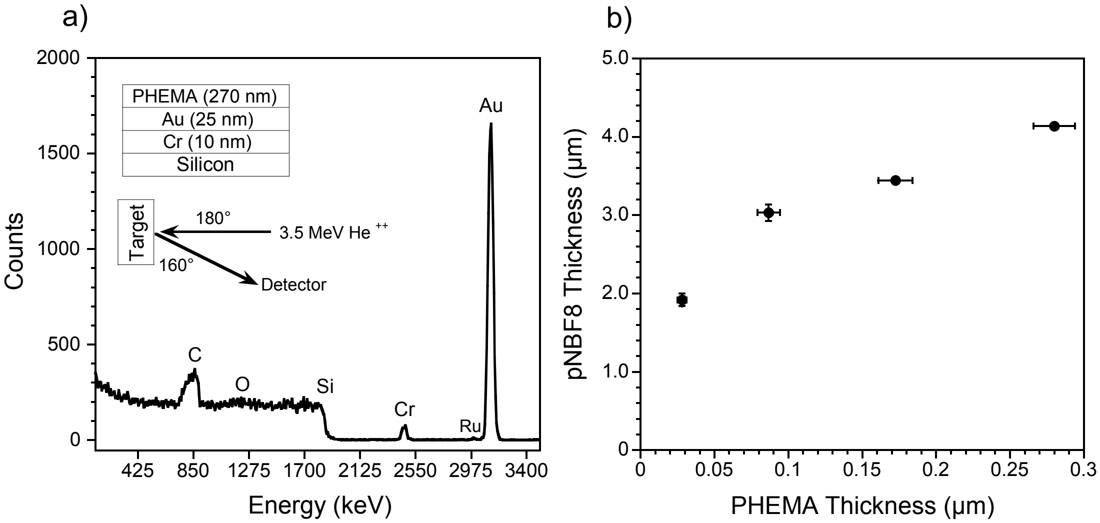

Figure 5.2. a) RBS spectrum for an activated PHEMA film, b) thickness profile of pNBF8 films grown from PHEMA films as thick as ~ 0.03, 0.09, 0.17, and 0.28 µm. Polymerizations were performed in a 0.05 M monomer solution during 15 min. Respective PHEMA thicknesses were subtracted from the final pNBF8 thickness values.

Polymer Film Properties

Reflectance Absorption Infrared Spectroscopy (RAIRS)

Figure 5.3 shows the reflectance absorbance IR spectra of a PHEMA film and its compositional changes after the acylation and polymerization steps. PHEMA is characterized by absorption bands originating from hydroxyl stretching (3200 – 3650 cm^{-1}), C=O stretching (1732 cm^{-1}), C–H stretching vibrations of CH_2 and CH_3 groups (2800 – 3050 cm^{-1}), and in-plane bending vibrations of CH_2, twist and rock vibrations of CH_2, and stretching vibrations of C–O–C at 1483, 1367, and 1079 cm^{-1}, respectively.[43] The most noticeable changes in the IR spectrum of PHEMA after the acylation process are the reduction of the hydroxyl peak and the appearance of a broader, more intense carbonyl peak that represents both the PHEMA carbonyl and the carbonyl formed after the reaction (~ 1738 cm^{-1}), both of which suggest that the –OH groups in the film reacted with NBDAC to form esters. After exposure to NBF8 for 1 min, the intensity of the C–H stretching vibrations increased significantly, owing to the presence of cyclic methylene stretching from the cyclopentane units in the pNBF8 backbone. The decline in the intensity of the carbonyl peak may be attributed to the growth of a thick pNBF8 film, i.e., the average thickness for this film was 1 μm, which is slightly opaque and may obscure the intensity of the C=O peak by limiting the reflectance of the IR beam. In addition, strong CF_2 bands appeared from 1100 – 1400 cm^{-1} as a consequence of the fluorocarbon side chain in the monomer unit. Specifically, two types of CF_2 stretching are present: those parallel to the helical structure of the fluorocarbon chain (ν_{ax} (CF_2), 1300 – 1400 cm^{-1}) and those perpendicular to the helical axis (ν_{pd} (CF_2), 1100 – 1300 cm^{-1}).[16] The large ratio of ν_{pd} (CF_2):ν_{ax} (CF_2) absorbances in the IR spectrum suggests that the majority of the fluorocarbon chains in the film assume a parallel orientation.[16]

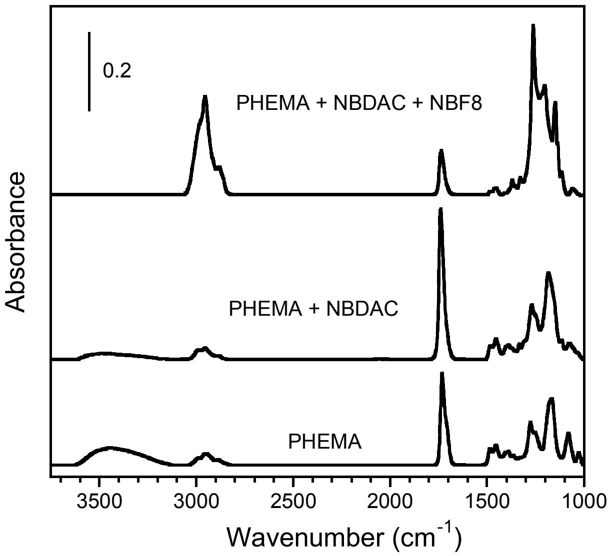

Figure 5.3. Reflectance absorption IR spectra of PHEMA on gold-coated substrates before and after the acylation and polymerization processes. The polymerization step ended after 1 min. The spectra have been offset vertically for clarity.

Contact Angles

Table 5.4 summarizes the measured advancing (θ_A) water and hexadecane (HD) contact angles for pNBFn films grown in a 0.05 M monomer solution after 15 min of polymerization. The trend exhibited in both water and HD contact angles with chain length agrees with the critical surface tensions (γ_C) that we have previously reported for monolayer-initiated films.[16] As n increases from 4 to 8, the oleophobicity and hydrophobicity increase due to increasing coverage of fluorocarbons on the surface. The low γ_C values for n = 6, 8, and 10 suggest that the surface is rich in $–CF_3$ groups as a pure $–CF_3$ surface has a γ_C = 6 mN•m^{-1}, whereas a $–CF_2–$ surface has a γ_C of ~ 18 mN•m^{-1}. The higher wettability of pNBF10 films towards water and HD (as compared to pNBF8) may be attributed to its larger CF_2:CF_3 ratio, which leads to more $–CF_2–$ groups exposed at the outer surface and increases its γ_C.[16,44] Comparison of the measured water contact angles for a common fluorocarbon chain length suggests that, at low concentrations, the hydrophobicity of the resulting films is irrespective of the initiation process, whereas macroinitiated films of pNBF4 and pNBF6 were more oleophobic than their monolayer-initiated counterparts. Similarly, increasing the polymerization time does not have an effect on the hydrophobicity of the films, as the θ_A (H_2O) for 1 and 5 min of polymerization (not shown) are similar to those for 15 min. However, a moderate increase in both the hydrophobic and oleophobic character of the films occurred with an increase in concentration (see Table A.2 in APPENDIX A), for which macroinitiated films exhibited a more pronounced effect (vide infra).

Table 5.4. Wetting properties of the pNBFn films prepared in a 0.05 M monomer solution, after 15 min of polymerization at 21 °C. Contact angles are in degrees.

		Monolayer		Macroinitiator	
pNBFn	γ_C (mN•m^{-1})	θ_A (H_2O)	θ_A (HD)	θ_A (H_2O)	θ_A (HD)
4	19 ± 2	112 ± 1	58 ± 1	113 ± 1	67 ± 1
6	13 ± 1	118 ± 2	71 ± 1	120 ± 1	74 ± 1
8	9 ± 1	126 ± 1	78 ± 1	127 ± 1	76 ± 3
10	11 ± 1	119 ± 3	71 ± 1	120 ± 1	71 ± 2

Figures 5.4a – c show SEM images of the surface topography of macroinitiated pNBF8 films polymerized in different monomer concentrations for 15 min at 21 °C. All films show a relatively smooth base supporting globular-like structures. A closer inspection of the surface reveals that these features result from the surface-initiated polymerization process, as they are actually emerging from the smooth areas of the film. Increasing the monomer concentration from 0.05 M (Figure 5.4a) to 0.2 M (Figure 5.4b) causes the round structures to agglomerate to form isolated, multiple scaled clusters comprised of tens, and in some cases, hundreds of globules. When the polymerization process takes place at a higher monomer concentration (1 M), the

clusters become interconnected by, what seems to be, a continuous emergence of globular features, resulting in a denser network of larger structures, as shown in Figure 5.4c. An example of a hemisphere-like structure with diameter of ~ 25 μm is shown as well. The increased roughness at higher concentrations results in a higher advancing H_2O and HD contact angles (see Table A.2 in APPENDIX A). Figure 5.4d shows a remarkable example of how polymerization temperature affects surface roughness, and consequently, the wettability of a macroinitiated pNBF8 film polymerized at 38 °C in a 0.05 M monomer solution. Notably, despite the fact that the polymerization occurred at a low monomer concentration, the density of visible and emerging globular features and clusters is larger than those of films grown at 21 °C. As a result, the film exhibited an increase in both θ_A (water) (~ 165°) and θ_A (HD) (~ 94°).

Electrochemical impedance spectroscopy (EIS)

The robustness, stability, thickness, and low wettability towards water and oils exhibited by these partially fluorinated films make them ideal candidates to be used as protective coatings. To characterize the barrier properties of monolayer-initiated and macroinitiated pNBF8 films, EIS was performed in an aqueous solution containing 1 mM $K_3Fe(CN)_6$, 1 mM $K_4Fe(CN)_6{\bullet}3H_2O$, and 0.1 M Na_2SO_4. Figure 5.5 shows impedance spectra in the form of Bode magnitude plots for gold electrodes functionalized with monolayer-initiated pNBF8 and macroinitiated pNBF8 as well as controls consisting of PHEMA or a SAM prepared from 4-mercapto-1-butanol, each exposed to NBDAC, and an unfunctionalized gold electrode (Au).

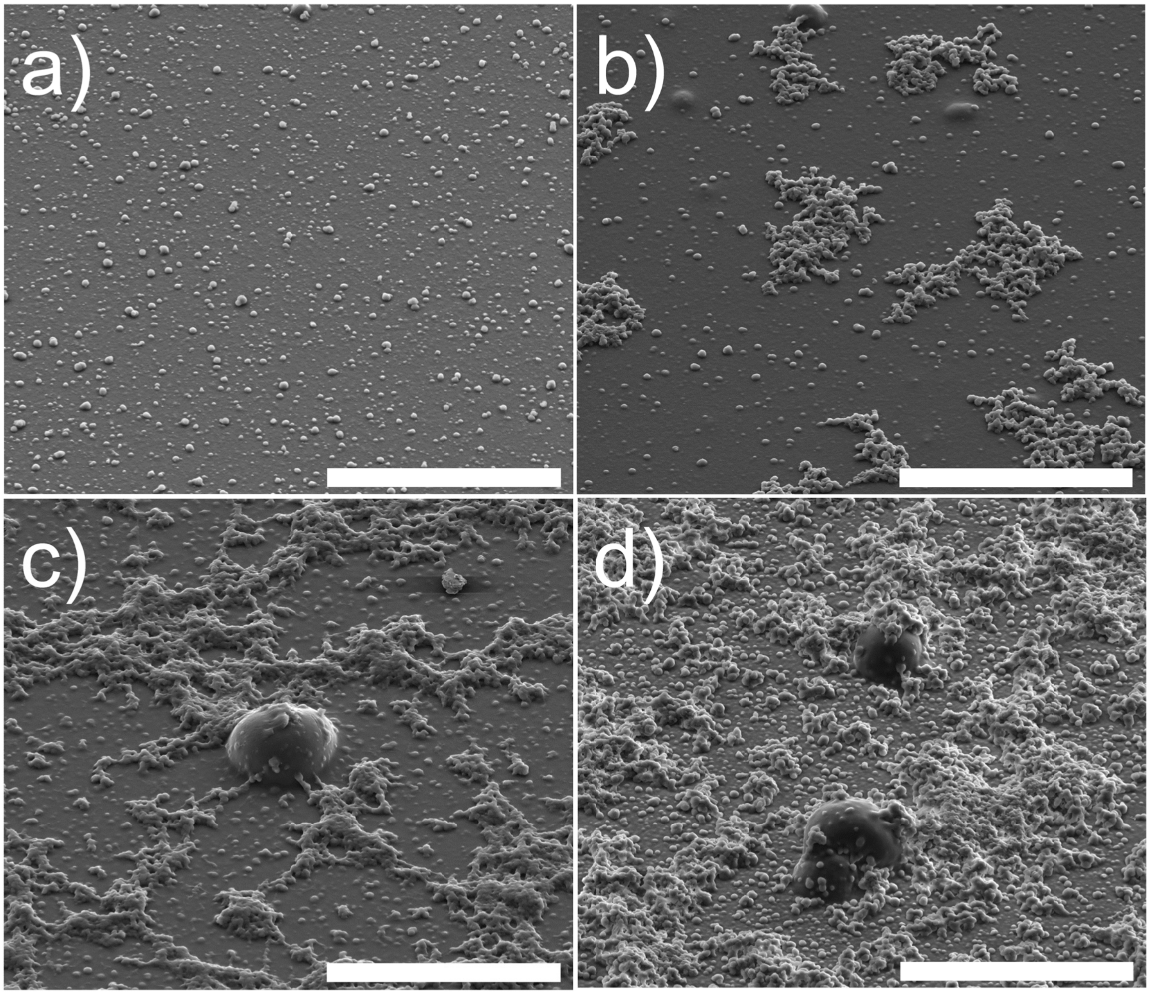

Figure 5.4. Scanning electron microscopy images showing the surface roughness of macroinitiated pNBF8 films polymerized for 15 min in various monomer concentrations a) 0.05 M, b) 0.2 M, c) 1 M, and d) 0.05 M (@ 38 °C). Images were taken at a 45° angle with respect to the surface normal. Scale bar indicates 50 µm.

The monolayer- and macroinitiated films were grown in 1 M NBF8 for 5 min, and their thicknesses are 5.3 µm and 11.3 µm, respectively. Upon comparison of both pNBF8 spectra with those of the modified monolayer and PHEMA, Figure 5.5 shows that the impedance at low frequency improves by over 4 orders of magnitude through growth of the hydrophobic pNBF8 film. To provide quantitative information regarding the resistance and capacitance of the films, the experimental data were fit with an appropriate equivalent circuit[45] model. Quantitative results drawn from the fitting process reveal that the charge transfer resistance of the unfunctionalized gold is ~ 38 Ω•cm^2, whereas the resistances for the modified monolayer, modified PHEMA, and monolayer- and macroinitiated pNBF8 films are 1.3×10^3, 1.2×10^5, 3.2×10^7 and $> 1 \times 10^{10}$ Ω•cm^2, respectively. The impedance responses of self-assembled monolayers[46] and modified PHEMA[45] have been described previously by us and thus, are not further described here. The spectrum for the monolayer-initiated film is likewise similar to what we have reported previously,[16] showing a capacitive region at intermediate to high frequencies and a resistance against the penetration of redox species at low frequencies. The spectrum of the macroinitiated film, by contrast, does not show a resistive behavior; instead, its response is completely capacitive, i.e., a linear increase in impedance with decreasing frequency. This is further corroborated by a phase angle of – 90°, which is characteristic of a purely capacitive behavior,[47] for all the frequencies sampled. Accordingly, the film acts as a perfect barrier to the transport of ions over the frequency range. In fact, the capacitance obtained from the fit for the monolayer-initiated film (1.5×10^{-9} F•cm^{-2}) is 7.5-fold higher than that of the macroinitiated film (2.0×10^{-10} F•cm^{-2}). As capacitance is proportional to (thickness)$^{-1}$ in a Helmholtz model, the ratio of 7.5 suggests that the 11.3-µm macroinitiated film is much more effective than the 5.3-µm monolayer-initiated film in reducing water penetration into the film. The presence of water would raise the effective dielectric constant of the film and lead to higher capacitances. In summary, these results demonstrate the importance of constructing thick, hydrophobic coatings for substrate protection, and macro-initiated SI–ROMP provides a versatile approach to achieve such thicknesses for robustly bound coatings.

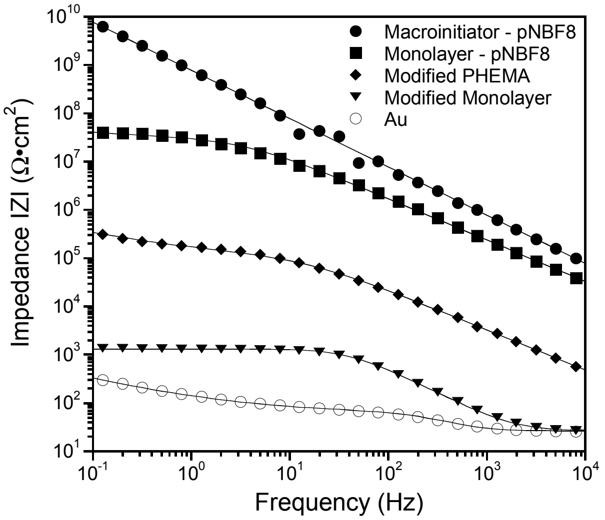

Figure 5.5. Electrochemical impedance spectra collected for bare Au, the NBDAC-modified SAM and PHEMA films, as well as monolayer-initiated and macroinitiated pNBF8 films polymerized for 5 min in a 1 M monomer solution at 21 °C. The redox species and electrolyte consisted of $K_3Fe(CN)_6$ and $K_4Fe(CN)_6•3H_2O$, and Na_2SO_4, respectively. Solid lines indicate fits of the data using an appropriate equivalent circuit model.

Kinetics of Film Growth

Figure 5.6 shows the effects of fluorocarbon chain length and macroinitiation on the time-dependence of pNBFn film thickness from a 0.05 M monomer solution, as measured by profilometry. The rate of film growth increases as the fluorocarbon side chain length increases, and the macroinitiator produces much thicker pNBFn films than the monolayer (note difference in y scale). Although the rate of growth for all the monomers decreases after 5 min of polymerization, films as thick as ~ 1.2 and 6.2 μm for the monolayer and macroinitiation processes, respectively, were achieved with pNBF10 in just 15 min at this low monomer concentration.

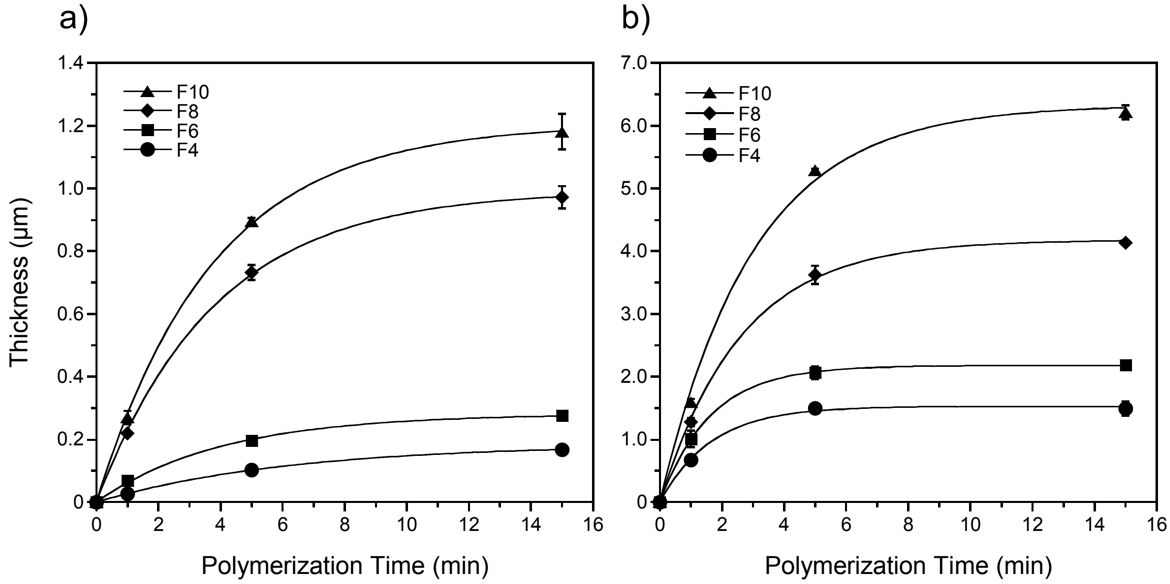

Figure 5.6. Profilometry film thickness of pNBFn, n = 4, 6, 8, 10, films prepared from a) a monolayer and from b) a macroinitiator. All the films were grown from a 0.05 M monomer solution. For the macroinitiator case, an average thickness for PHEMA of 280 nm was subtracted from the measured thickness. Solid curves represent fits of the data using equation. 5.3.

The deceleration of film growth is common in surface-initiated polymerizations[8,42,48] and may be attributed to a progressive deactivation of the Ru catalyst by, for example, dissolved oxygen in the monomer solution[49,50] and/or to the prompt occlusion of the active Ru centers from the monomer by the fast-growing pNBFn film. The former was somewhat expected, as both the activation of the substrates and the polymerization process took place under ambient conditions. In summary, after 15 min of polymerization, the macroinitiated pNBFn films were thicker than their monolayer counterparts by a factor of 9 for both pNBF4 and pNBF6, and 4 and 5 for pNBF8 and pNBF10.

To estimate the relative propagation and termination rate constants involved in the growth of these pNBFn films, and therefore, the relative reactivity of the monomers used, we employed a kinetic model developed by Harada et al.[42] In this model, the change of film thickness (*d*) as a function of time was given as

$$d = \left(\frac{k_p M}{k_t}\right)\left(\frac{m_0 P_I}{\rho}\right)\left(1 - e^{-k_t t}\right) \tag{5.1}$$

where k_p is the propagation rate constant, M is the concentration of the monomer in solution, k_t is the termination rate constant, m_0 is the mass of the monomer unit, P_I is the initial number of active catalyst sites per unit area, and ρ is the density of the polymer. The model assumes that the growing polymer chains add one monomer unit at a time at a propagation rate of k_p in a second-order reaction, and that the active catalyst may become irreversibly deactivated in each step by a first-order reaction at a rate of k_t. Since the value of P_I for the norbornenyl-decorated SAM is below the detection limit, as noted earlier in the XPS results, we opted for the combination of k_p and P_I as a single rate term (K) for film growth

$$K = k_p P_I \tag{5.2}$$

which expresses both initiation and propagation. Accordingly, this term allows a general comparison of film growth kinetics for this series of monomers. As a result, equation (5.1) becomes

$$d = \left(\frac{K M m_0}{k_t \rho}\right)\left(1 - e^{-k_t t}\right) \tag{5.3}$$

In addition, we approximated the density of the polymer films, i.e., pNBF4, pNBF6, pNBF8, and pNBF10, to that of the monomers, as measured by pycnometry, to be 1.46, 1.54, 1.62, and 1.70 g•cm^{-3}, respectively.

Table 5.5 summarizes the estimated values for K and k_t obtained from fitting the experimental data with Equation 5.3. In general, an increase in the film growth rate constant K was observed from pNBF4 to pNBF10 for both the monolayer and the macroinitiator approaches.

Table 5.5. Relative film growth and termination rate constants for NBFn monomers, n = 4, 6, 8, 10, polymerized from a monolayer or a macroinitiator. The concentration of the monomer solution was 0.05 M. Values are presented along with their standard errors.

	Monolayer		Macroinitiator	
Monomer	K (m•s^{-1})	k_t (s^{-1})	K (m•s^{-1})	k_t (s^{-1})
NBF4	$4.6 \times 10^{-8} \pm 5.4 \times 10^{-10}$	$0.0026 \pm 4.6 \times 10^{-5}$	$1.4 \times 10^{-6} \pm 1.2 \times 10^{-7}$	$0.0100 \pm 9.5 \times 10^{-4}$
NBF6	$8.7 \times 10^{-8} \pm 4.6 \times 10^{-9}$	$0.0041 \pm 2.8 \times 10^{-4}$	$1.7 \times 10^{-6} \pm 2.9 \times 10^{-8}$	$0.0102 \pm 2.1 \times 10^{-4}$
NBF8	$2.7 \times 10^{-7} \pm 6.6 \times 10^{-9}$	$0.0043 \pm 1.3 \times 10^{-4}$	$1.7 \times 10^{-6} \pm 7.1 \times 10^{-8}$	$0.0064 \pm 3.2 \times 10^{-4}$
NBF10	$2.9 \times 10^{-7} \pm 7.2 \times 10^{-9}$	$0.0044 \pm 1.3 \times 10^{-4}$	$1.9 \times 10^{-6} \pm 1.6 \times 10^{-7}$	$0.0055 \pm 5.6 \times 10^{-4}$

In the monolayer initiation process, there was a 6.3-fold increase in K from NBF4 to NBF10, whereas for the macroinitiation approach, it was only 1.4. For NBF4, the ratio of K macroinitiator to K monolayer is 31. Analogously, the macroinitiator to monolayer K ratios for NBF6, NBF8, and NBF10 were ~ 19, 6, and 7, respectively. In this connection, the greater macroinitiator to monolayer K ratio exhibited when polymerizing smaller monomers may be attributed to a better ability for these molecules to penetrate to a greater extent, not only into activated PHEMA, but also into the growing pNBFn film itself. As a consequence, diffusing monomers may react with still active growing chains from within PHEMA, e.g., those that started to grow later than their surface counterparts, and/or Ru molecules that had not yet reacted or were not deactivated.

The termination rate constant k_t for the monolayer initiation also exhibited an overall increase, namely, its value increased by 69% from NBF4 to NBF10. However, the difference in k_t values between NBF6, NBF8, and NBF10 was small, such that, within error, k_t may be assumed to be the same for these three monomers. The values of k_t for the macroinitiation approach are, in general, higher than those of their monolayer counterparts. The use of a macroinitiator not only provides an increase in the number of potential active sites from which the pNBFn film can grow, it may also increase the probability of termination reactions as a consequence of higher localized chain concentration. In other words, because of their greater proximity, a consequence of the higher number of sites onto which Ru can be anchored, active Ru centers on growing chains may react with each other and terminate the polymerization process. In addition, the probability of secondary metathesis and backbiting reactions may increase as well.[22,51] Despite the fact that macroinitiator k_t values were higher than their monolayer counterparts; there was a noticeable 45% reduction in k_t from NBF4 to NBF10. Interestingly, k_t decreases for NBF8 and NBF10. This outcome suggests that longer side chains could promote more growth by protecting both the active Ru center and the backbone olefin functionality from termination reactions such as those mentioned above.

I also studied the effects of monomer concentration on pNBF8 film thickness for both initiation processes (see Figure A.1 and Table A.3 in APPENDIX A). In general, an increase in concentration promoted faster polymerization rates and the growth of thicker pNBF8 films, with the macroinitiated pNBF8 films being thicker than the ones initiated from a monolayer. However, the ratio of macroinitiator thickness to monolayer thickness decreased with an increase in concentration from 0.05 M to 1 M, indicating that the macroinitiation process becomes less effective, relative to monolayer initiation, at higher monomer concentrations. At these high concentrations, the initiators nearest the solution interface are predominantly utilized as the deeper ones become rapidly occluded so that the macroinitiation starts to resemble a 2-D initiation. The maximum pNBF8 film thickness achieved by the monolayer initiation process after 15 min of polymerization, at a concentration of 1 M, was 5.6 μm, whereas the resulting pNBF8 film thickness for the macroinitiated polymerization, under the same conditions of time and concentration, was ~ 12 μm.

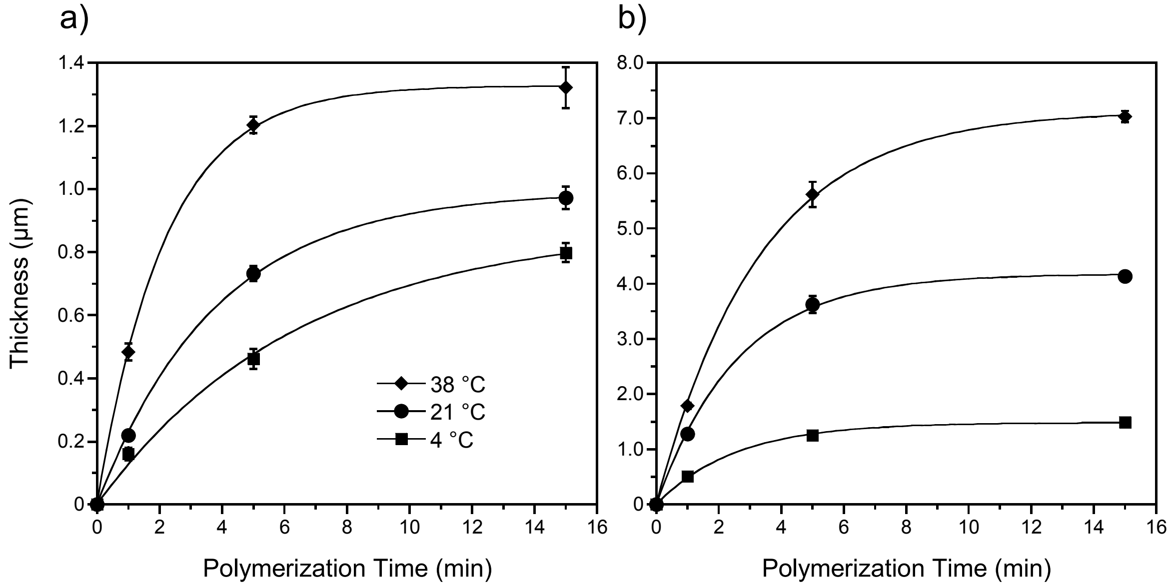

Figure 5.7. Temperature effects on film thickness for a) a monolayer initiation and b) macroinitiation. Data refer to pNBF8 films grown from a 0.05 M monomer solution. For the macroinitiator case, an average thickness for PHEMA of 280 nm was subtracted from the measured thickness. Solid curves represent data fits using equation 5.3.

Figure 5.7 shows the effect of temperature on the thickness of pNBF8 films prepared either from a monolayer or a macroinitiator. In this case, the polymerizations were performed at three temperatures, namely, 4, 21, and 38 °C, in a 0.05 M monomer solution. In general, film thickness increases as temperature increases. The effect of temperature was greater for the macroinitiation process, as evidenced by much thicker films than those obtained from the monolayer approach. For example, a change in polymerization temperature from 4 to 38 °C resulted in an increase in maximum thickness (that achieved at 15 min of polymerization) by ~ 1.6 and 5-fold for the monolayer and the macroinitiation processes, respectively. Moreover, the ratios of the maximum thickness achieved by films prepared from a macroinitiator to that of films prepared from a monolayer were 1.9, 4.3, and 5.3 at 4, 21, and 38 °C, respectively. This overall trend of achieving thicker films by performing the polymerization at higher temperatures, as shown in Figure 5.7, may be explained as a result of an increase in the activity of the catalyst with an increase in temperature.[49,52] Diffusion and solubility of the monomer unit into the pNBF8 film are additional factors that may contribute toward the strong effect of temperature on film growth. In general, an increase in temperature can produce a considerable increase in the diffusion coefficient of molecules and, consequently, we would expect an increased permeability of monomer through the growing polymer to the active Ru sites;[53] likewise, higher temperatures can increase the solubility of fluorous solutes in flourous media, as discussed by Gladysz et al.[54]

In a further effort to characterize the activation energy (E_a) required for both the monolayer and macroinitiation processes, an Arrhenius plot (Figure 5.8) was created. Both initiation processes exhibit an increase in the film growth rate constant K with increasing temperature. For example, K incremented by a factor of 4.6 and 3.7, from 4 to 38 °C, yielding E_a values of 31 and 28 $kJ{\bullet}mol^{-1}$ for the monolayer and macroinitiation approaches, respectively. A rise in temperature has a separate effect on the termination rate constant k_t for each initiation process; whereas k_t for the monolayer triples its value with a change in temperature from 4 to 38 °C, exhibiting an E_a of 23 $kJ{\bullet}mol^{-1}$, k_t for the macroinitiator decreases by ~ 25% ($E_a = -6$ $kJ{\bullet}mol^{-1}$). A plausible explanation for this discrepancy may be attributed to a fast-growing polymer front in the macroinitation process that may shield active Ru centers from terminating agents, in contrast to the monolayer-initiated case where the initiators are located near the solution/polymer interface. A related possibility is that the number of collisions between these buried active Ru centers and deactivating species, such as dissolved oxygen molecules, may tend to decrease at higher temperatures as a consequence of a lower solubility of oxygen within the film at higher temperature. Solubility studies of oxygen in liquid perfluorocarbons,[55] fluorinated liquids,[56] and hydrocarbons[57] show that such a trend is not unusual.

The values of E_a for K are in reasonable agreement with values reported for other ring-opening polymerization reactions, which generally fall in the range of 20 – 80 kJ•mol^{-1} with most values on the high end of this range.[58] In summary, a higher E_a for K compared to that of k_t is consistent with the use of higher temperatures to achieve greater film thickness.

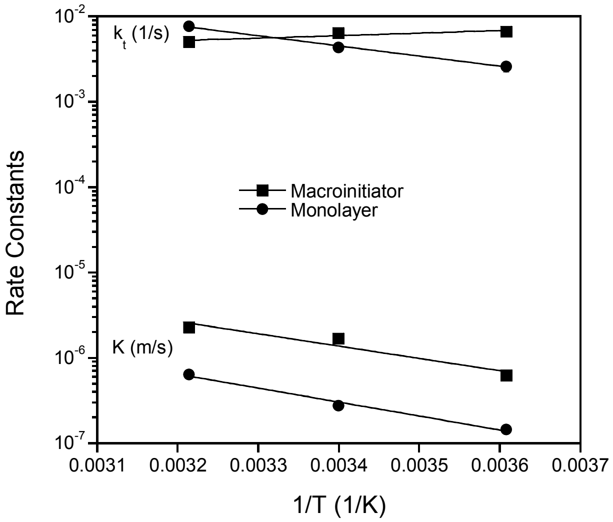

Figure 5.8. Arrhenius plot showing the temperature effect on film growth and termination rate constants.

Conclusions

The enhancement in the polymerization rate and the greater film thickness of the partially fluorinated polymer films achieved in this study demonstrate that the SI-ROMP of 5-(perfluoro-n-alkyl)norbornenes is greatly amplified by employing a PHEMA-based macroinititiation process. The effectiveness of this approach, by contrast to a monolayer initiation, relies on the ability to immobilize a higher number of catalyst molecules into PHEMA, as confirmed by XPS analysis, by derivatizing its hydroxyl functional groups via post-polymerization reactions. The length of the fluorocarbon side chain, monomer concentration, and temperature had marked effects on the polymerization kinetics and thickness of the resulting pNBFn films. In summary, longer side chains, higher concentrations, and higher temperatures promoted faster polymerization rates and thicker films. The polymerization approach enables fine-tuning of the thickness and wetting properties of pNBFn films by adjusting any of the variables described above. The achievement of exceptionally thick pNBFn films, exhibiting remarkable barrier properties, renders this method as a potential candidate for the preparation of highly effective and stable surface-bound protective coatings.

References

(1) Jennings, G. K.; Brantley, E. L. Physicochemical Properties of Surface-Initiated Polymer Films in the Modification and Processing of Materials. *Adv. Mater.* **2004,** 16, 1983-1994.

(2) Olivier, A.; Meyer, F.; Raquez, J.-M.; Damman, P.; Dubois, P. Surface-Initiated Controlled Polymerization as a Convenient Method for Designing Functional Polymer Brushes: From Self-Assembled Monolayers to Patterned Surfaces. *Prog. Polym. Sci.* **2012,** 37, 157-181.

(3) Edmondson, S.; Armes, S. P. Synthesis of Surface-Initiated Polymer Brushes Using Macro-Initiators. *Polym Int* **2009,** 58, 307 - 316.

(4) Detrembleur, C.; Jérôme, C.; Claes, M.; Louette, P.; Jérôme, R. Combination of Electrografting and Ring-Opening Metathesis Polymerization: An Efficient Way to Prepare Polynorbornene Brushes on Conducting Substrates. *Angew. Chem. Int.* **2001,** 40, 1268 - 1271.

(5) Voccia, S.; Claes, M.; Jérôme, R.; Jérôme, C. Sequential Electrografting and Ring-Opening Metathesis Polymerization: a Strategy for the Tailoring of Conductive Surfaces. *Macromol. Rapid Commun.* **2005,** 26, 779 - 783.

(6) Tuberquia, J. C.; Nizamidin, N.; Harl, R. R.; Albert, J.; Hunter, J.; Rogers, B. R.; Jennings, G. K. Surface-Initiated Polymerization of Superhydrophobic Polymethylene. *J. Am. Chem. Soc.* **2010,** 132, 5725-5734.

(7) Skale, S.; Doleček, V.; Slemnik, M. Electrochemical Impedance Studies of Corrosion Protected Surfaces Covered by Epoxy Polyamide Coating Systems. *Prog. Org. Coat.* **2008,** 62, 387-392.

(8) Huang, W.; Kim, J.-B.; Bruening, M. L.; Baker, G. L. Functionalization of Surfaces by Water-Accelerated Atom-Transfer Radical Polymerization of Hydroxyethyl Methacrylate and Subsequent Derivatization. *Macromolecules* **2002,** 35, 1175-1179.

(9) Guo, W. F.; Jennings, G. K. Directed Growth of Polymethylene Films on Atomically Modified Gold Surfaces. *Adv. Mater.* **2003,** 15, 588-591.

(10) Hansen, N. M. L.; Jankova, K.; Hvilsted, S. Fluoropolymer Materials and Architectures Prepared by Controlled Radical Polymerizations. *Eur. Polym. J.* **2007,** 43, 255-293.

(11) Delucchi, M.; Turri, S.; Barbucci, A.; Bassi, M.; Novelli, S.; Cerisola, G. Fluoropolyether Coatings: Relationships of Electrochemical Impedance Spectroscopy Measurements, Barrier Properties, and Polymer Structure. *J. Polym. Sci., Part B: Polym. Phys.* **2002,** 40, 52 - 64.

(12) Sorensen, P. A.; Kiil, S.; Dam-Johansen, K.; Weinell, C. E. Anticorrosive Coatings: A Review. *J. Coat. Technol. Res.* **2009,** 6, 135-176.

(13) Balachandra, A. M.; Baker, G. L.; Bruening, M. L. Preparation of Composite Membranes by Atom Transfer Radical Polymerization Initiated from a Porous Support. *J. Membr. Sci.* **2003,** 227, 1-14.

(14) Escobar, C. A.; Zulkifli, A. R.; Faulkner, C. J.; Trzeciak, A.; Jennings, G. K. Composite Fluorocarbon Membranes by Surface-Initiated Polymerization from Nanoporous Gold-Coated Alumina. *ACS Appl. Mater. Interfaces* **2012,** 4, 906-915.

(15) Ye, Q.; Wang, X.; Li, S.; Zhou, F. Surface-Initiated Ring-Opening Metathesis Polymerization of Pentadecafluorooctyl-5-norbornene-2-carboxylate from Variable Substrates Modified with Sticky Biomimic Initiator. *Macromolecules* **2010,** 43, 5554-5560.

(16) Faulkner, C. J.; Fischer, R. E.; Jennings, G. K. Surface-Initiated Polymerization of 5-(Perfluoro-n-alkyl)norbornenes from Gold Substrates. *Macromolecules* **2010,** 43, 1203-1209.

(17) Weck, M.; Jackiw, J. J.; Rossi, R. R.; Weiss, P. S.; Grubbs, R. H. Ring-Opening Metathesis Polymerization from Surfaces. *J. Am. Chem. Soc.* **1999,** 121, 4088-4089.

(18) Juang, A.; Scherman, O. A.; Grubbs, R. H.; Lewis, N. S. Formation of Covalently Attached Polymer Overlayers on Si(111) Surfaces Using Ring-Opening Metathesis Polymerization Methods. *Langmuir* **2001,** 17, 1321-1323.

(19) Pyun, J.; Kowalewski, T.; Matyjaszewski, K. Synthesis of Polymer Brushes Using Atom Transfer Radical Polymerization. *Macromol. Rapid Commun.* **2003,** 24, 1043 - 1059.

(20) Leitgeb, A.; Wappel, J.; Slugovc, C. The ROMP Toolbox Upgraded. *Polymer* **2010,** 51, 2927-2946.

(21) Barbey, R.; Lavanant, L.; Paripovic, D.; Schüwer, N.; Sugnaux, C.; Tugulu, S.; Klok, H.-A. Polymer Brushes via Surface-Initiated Controlled Radical Polymerization: Synthesis, Characterization, Properties, and Applications. *Chem. Rev.* **2009,** 109, 5437-5527.

(22) Bielawski, C. W.; Grubbs, R. H. Living Ring-Opening Metathesis Polymerization. *Prog. Polym. Sci.* **2007,** 32, 1-29.

(23) Buchmeiser, M. R. Metathesis Polymerization to and from Surfaces. In *Surface-Initiated Polymerization I*; Jordan, R., Ed.; Springer-Verlag Berlin: Berlin, **2006**; Vol. 197, p 137-171.

(24) Wang, X. S.; F. Lascelles, S.; A. Jackson, R.; P. Armes, S. Facile Synthesis of Well-Defined Water-Soluble Polymers Via Atom Transfer Radical Polymerization in Aqueous Media at Ambient Temperature. *Chem. Commun.* **1999**, 1817-1818.

(25) Brantley, E. L.; Holmes, T. C.; Jennings, G. K. Blocklike Fluorocarbon and Hydrocarbon Copolymer Films via Surface-Initiated ATRP and Postpolymerization Reactions. *Macromolecules* **2005,** 38, 9730-9734.

(26) Saha, S.; Bruening, M. L.; Baker, G. L. Facile Synthesis of Thick Films of Poly(methyl methacrylate), Poly(styrene), and Poly(vinyl pyridine) from Au Surfaces. *ACS Appl. Mater. Interfaces* **2011,** 3, 3042-3048.

(27) Carlsson, L.; Malmstrom, E.; Carlmark, A. Surface-Initiated Ring-Opening Metathesis Polymerisation from Cellulose Fibres. *Polym. Chem.* **2012,** 3, 727-733.

(28) Rutenberg, I. M.; Scherman, O. A.; Grubbs, R. H.; Jiang, W.; Garfunkel, E.; Bao, Z. Synthesis of Polymer Dielectric Layers for Organic Thin Film Transistors via Surface-Initiated Ring-Opening Metathesis Polymerization. *J. Am. Chem. Soc.* **2004,** 126, 4062-4063.

(29) Edmondson, S.; Vo, C.-D.; Armes, S. P.; Unali, G.-F.; Weir, M. P. Layer-by-Layer Deposition of Polyelectrolyte Macroinitiators for Enhanced Initiator Density in Surface-Initiated ATRP. *Langmuir* **2008,** 24, 7208-7215.

(30) Tomlinson, M. R.; Efimenko, K.; Genzer, J. Study of Kinetics and Macroinitiator Efficiency in Surface-Initiated Atom-Transfer Radical Polymerization. *Macromolecules* **2006,** 39, 9049-9056.

(31) Liu, Y.; Klep, V.; Zdyrko, B.; Luzinov, I. Polymer Grafting via ATRP Initiated from Macroinitiator Synthesized on Surface. *Langmuir* **2004,** 20, 6710-6718.

(32) Gabriel, S.; Jérôme, R.; Jérôme, C. Cathodic Electrografting of Acrylics: From Fundamentals to Functional Coatings. *Prog. Polym. Sci.* **2010,** 35, 113-140.

(33) Belanger, D.; Pinson, J. Electrografting: A Powerful Method for Surface Modification. *Chem. Soc. Rev.* **2011,** 40, 3995-4048.

(34) Jung, D.-H.; Park, I. J.; Choi, Y. K.; Lee, S.-B.; Park, H. S.; Rühe, J. Perfluorinated Polymer Monolayers on Porous Silica for Materials with Super Liquid Repellent Properties. *Langmuir* **2002,** 18, 6133-6139.

(35) Jordan, R.; Advincula, R.; Buchmeiser, R.; Dyer, D. J.; Fukuda, T.; Goto, A.; Matsuda, T.; Ohno, K.; Tsujii, Y.; Yamamoto, S. *Surface-Initiated Polymerization I*; Springer, **2010**.

(36) Shah, R. R.; Merreceyes, D.; Husemann, M.; Rees, I.; Abbott, N. L.; Hawker, C. J.; Hedrick, J. L. Using Atom Transfer Radical Polymerization To Amplify Monolayers of Initiators Patterned by Microcontact Printing into Polymer Brushes for Pattern Transfer. *Macromolecules* **2000,** 33, 597-605.

(37) Kwok, A. Y.; Qiao, G. G.; Solomon, D. H. Synthetic Hydrogels 3. Solvent Effects on Poly(2-hydroxyethyl methacrylate) Networks. *Polymer* **2004,** 45, 4017-4027.

(38) Brandrup, J.; Immergut, E. H.; Grulke, E. A.; Abe, A.; Bloch, D. R. *Polymer Handbook (4th Edition)*; John Wiley & Sons, **2003**.

(39) Galvin, C. J.; Genzer, J. Applications of Surface-Grafted Macromolecules Derived from Post-Polymerization Modification Reactions. *Prog. Polym. Sci.* **2012,** 37, 871-906.

(40) Briggs, D.; Seah, P. *Practical Surface Analysis: Auger and X-ray photoelectron spectroscopy*; Wiley, **1990**.

(41) Tesmer, J. R.; Nastasi, M. A. *Handbook of modern ion beam materials analysis*; Materials Research Society, **1995**.

(42) Harada, Y.; Girolami, G. S.; Nuzzo, R. G. Catalytic Amplification of Patterning via Surface-Confined Ring-Opening Metathesis Polymerization on Mixed Primer Layers Formed by Contact Printing. *Langmuir* **2003,** 19, 5104-5114.

(43) Perova, T. S.; Vij, J. K.; Xu, H. Fourier Transform Infrared Study of Poly(2-hydroxyethyl methacrylate) PHEMA. *Colloid Polym. Sci.* **1997,** 275, 323-332.

(44) Fukushima, H.; Seki, S.; Nishikawa, T.; Takiguchi, H.; Tamada, K.; Abe, K.; Colorado, R.; Graupe, M.; Shmakova, O. E.; Lee, T. R. Microstructure, Wettability, and Thermal Stability of

Semifluorinated Self-Assembled Monolayers (SAMs) on Gold. *J. Phys. Chem. B* **2000,** 104, 7417-7423.

(45) Brantley, E. L.; Holmes, T. C.; Jennings, G. K. Modification of ATRP Surface-Initiated Poly(hydroxyethyl methacrylate) Films with Hydrocarbon Side Chains. *J. Phys. Chem. B* **2004,** 108, 16077-16084.

(46) Berron, B.; Jennings, G. K. Loosely Packed Hydroxyl-Terminated SAMs on Gold. *Langmuir* **2006,** 22, 7235-7240.

(47) Bard, A. J.; Faulkner, L. R. *Electrochemical Methods: Fundamentals and Applications*; Wiley, **2001**.

(48) Berron, B. J.; Graybill, E. P.; Jennings, G. K. Growth and Structure of Surface-Initiated Poly(n-alkylnorbornene) Films. *Langmuir* **2007,** 23, 11651-11655.

(49) Bielawski, C. W.; Grubbs, R. H. Highly Efficient Ring-Opening Metathesis Polymerization (ROMP) Using New Ruthenium Catalysts Containing N-Heterocyclic Carbene Ligands. *Angew. Chem.* **2000,** 39, 2903 - 2906.

(50) Love, J. A.; Sanford, M. S.; Day, M. W.; Grubbs, R. H. Synthesis, Structure, and Activity of Enhanced Initiators for Olefin Metathesis. *J. Am. Chem. Soc.* **2003,** 125, 10103-10109.

(51) Slugovc, C. The Ring Opening Metathesis Polymerisation Toolbox. *Macromol. Rapid Commun.* **2004,** 25, 1283-1297.

(52) Perring, M.; Bowden, N. B. Assembly of Organic Monolayers on Polydicyclopentadiene. *Langmuir* **2008,** 24, 10480-10487.

(53) Seader, J. D.; Henley, E. J. *Separation Process Principles*; John Wiley & Sons, Inc., **2006**, p 493.

(54) Gladysz, J.; Jurisch, M. Structural, Physical, and Chemical Properties of Fluorous Compounds. In *Fluorous Chemistry*; Horváth, I. T., Ed.; Springer Berlin Heidelberg: **2012**; Vol. 308, p 1-23.

(55) Dias, A. M. A.; Freire, M.; Coutinho, J. A. P.; Marrucho, I. M. Solubility of Oxygen in Liquid Perfluorocarbons. *Fluid Phase Equilib.* **2004,** 222–223, 325-330.

(56) Costa Gomes, M. F.; Deschamps, J.; Menz, D. H. Solubility of Dioxygen in Seven Fluorinated Liquids. *J. Fluorine Chem.* **2004,** 125, 1325-1329.

(57) Battino, R.; Rettich, T. R.; Tominaga, T. The Solubility of Oxygen and Ozone in Liquids. *J. Phys. Chem. Ref. Data* **1983,** 12, 163-178.

(58) Odian, G. G. *Principles of Polymerization*; Wiley, **2004**.

CHAPTER VI

MICROMOLDING SURFACE-INITIATED POLYMERIZATION: A VERSATILE ROUTE FOR FABRICATION OF MICROSCALE SURFACE FEATURES WITH HEIGHT MODULATION

Introduction

The provision of texture or patterns to surfaces in a controlled fashion plays a key role in applications such as microelectronics,[1] drag reduction,[2] optics,[3,4] chemical and corrosion protection,[5,6] and biomimetic systems.[7,8] While photolithography,[1] laser scanning,[1,9] and micro- and nanomachining[10] have long been used to fabricate surface texture and patterns, soft lithography, a suite of non-photolithographic techniques, was developed as an alternative, rapid, and low-cost option.[11] This technique employs soft materials such as poly(dimethylsiloxane) (PDMS) that may not exhibit the same physical properties of traditional rigid materials such as silicon, but offer advantages such as the capability to mold small-scale substrates with high fidelity, chemical inertness, transparency, durability, and low cost.[12] Limitations of soft lithography include the physisorbed nature of the polymeric microfeatures that hamper their long-term stability[13] and the inability to tune the size of the features independent of the mold. In this Chapter, I seek to employ soft lithography to develop robust chemically bound coatings with microscale surface features of tunable heights.

This Chapter describes the combination of soft lithographic molding and a surface-initiated polymerization (SIP) to produce a versatile process termed micromolding surface-initiated polymerization (μMSIP) for the fabrication of microscale-textured, surface-bound polymer coatings. Specifically, μMSIP involves the molding of a microscale-textured master with a polymeric composite comprising hard-PDMS (h-PDMS) and Sylgard 184 PDMS to produce a negative replica exhibiting the corresponding inverted structures of the master. This composite mold is then filled with pure monomer and subsequently pressed against an activated surface, i.e., a surface containing anchored initiator species to promote a polymerization. As the polymerization progresses, the surface-tethered growing polymer chains form a uniform film at the base and begin filling the inverted structures in the mold, thereby producing a coating where the surface topography reproduces the corresponding surface features of the master. Furthermore, I show that I am able to modulate the height of the surface features by tuning the conversion of the monomer through control of the initiator amount by means of a monolayer- or macroinitiation process or by systematically varying process variables such as temperature and polymerization time. If achievement of the full height of the master features is desired, either the monolayer or the macroinitiation approaches can be combined with the addition of initiator species into the mold. Moreover, the thickness of the coating at the base of the features can be controlled based on the amount of excess monomer added to the mold. Here, as the SIP, I use the surface-initiated ring-opening metathesis polymerization (SI-ROMP) of 5-(perfluorooctyl)norbornene (NBF8) onto gold-coated solid supports to yield partially fluorinated coatings with surface microfeatures and ultralow critical surface tensions (9 mN/m).[14] Representative examples of surface microstructures obtained through μMSIP include arrays of pyramids and inverted pyramids.

Extensive research efforts have established SI-ROMP as a robust, versatile polymerization technique.[15-18] SI-ROMP has become a useful technique for synthesizing polymers that exhibit tunable properties and functionalities with attractive biological, electronic, and mechanical properties.[19,20] Salient advantages of SI-ROMP include tolerance towards functional groups, rapid polymerization kinetics at room temperature under ambient conditions, preservation of the olefin functionality in the resulting polymer, and preparation of high-molecular weight polymers.[19,21] In Chapter V, I have shown that the SI-ROMP of the monomer NBF8 exhibits fast polymerization kinetics resulting in the formation of thick partially fluorinated polymer films exhibiting low wettability toward water and oils.[14,22]

Experimental Methods

Molding

The molds bearing the pattern of the master substrates, DFEA and Klarite®, were produced by means of soft lithography. Previous to the mold preparation, each master was placed in a plastic petri dish (5 cm in diameter) and then in a desiccator, along with a smaller petri dish containing three drops of TFOCS. To hold the masters still and prevent any movement, a small piece of double-sided tape was placed on the back of the samples. The masters were exposed to the vapor of TFOCS by holding the desiccator under vacuum for 30 min; this process creates a thin layer of TFOCS on the surface of the masters that prevents the resulting mold from adhering to it. The molding process, which yields an elastomeric composite comprising hard-PDMS (h-PDMS) and Sylgard 184 PDMS, proceeded as follows: 3.4 g of [(7–8% vinylmethylsiloxane)-(dimethylsiloxane)] copolymer, two drops of 1, 3, 5, 7-tetramethylcyclotetrasiloxane, and 1 drop of platinum divinyltetramethyldisiloxane were thoroughly mixed for at least 8 min with a glass rod in a weighing boat. During mixing, air bubbles are trapped within the mixture; to remove these, the weighing boat was placed in a desiccator connected to a vacuum line and evacuated until bubbles were no longer visible. As pressure decreases, bubbles begin to expand and rise; therefore, to prevent any spilling while degassing, the vacuum was broken and restored several times. Subsequently, 1 g of [(25–30% methylhydrosiloxane)-(dimethylsiloxane)] was added to the degassed mixture and rapidly stirred with the glass rod for 3 min. The mixture was poured onto the petri dishes containing the masters and placed once again in a desiccator connected to a vacuum line to remove the entrapped bubbles resulting from the rapid mixing. Similarly, vacuum was broken and restored several times. To cure the h-PDMS, the petri dishes were placed in an oven at 60 °C for 10 min. During the curing process, a mixture of Sylgard polymer base (4.0 g) and curing agent (0.4 g) was added to a weighing boat and thoroughly mixed using a glass rod for at least 8 min. Once the h-PDMS was cured, the petri dishes were removed from the oven and the freshly prepared Sylgard 184 PDMS/curing agent mixture was poured onto them. As in the previous step, the petri dishes were placed in a desiccator for degassing. Once free of bubbles, these were placed in an oven set at 60 °C and allowed to cure for 6 h. The resulting molds, exhibiting two layers, namely h-PDMS (~ 1 mm thick) and Sylgard 184 PDMS (~ 2 mm thick), were removed by gently breaking the entire wall surrounding the petri dish with pliers and carefully peeling them off the masters. Afterwards, the elastomeric molds were exposed to the vapor of TFOCS following the same procedure described earlier for 10 min in order to facilitate the separation of the substrate from the mold after polymerization.

Polymerization

Two different polymerization approaches were performed on the gold substrates to alter the amount of bound initiator. In one case, SI-ROMP was initiated from an initiator-activated self-assembled monolayer,[22] whereas in the other case, SI-ROMP was initiated from a macroinitiator prepared by surface-initiated atom transfer radical polymerization (SI-ATRP) with subsequent modification.[22] In the former approach, the gold samples were exposed to a 1 mM ethanolic solution of 4–mercapto–1–butanol for at least 1 h to create a hydroxyl-terminated self-assembled monolayer (SAM) on the gold surface. Afterwards, samples were rinsed in ethanol and dried in a stream of nitrogen. Subsequent exposure of the SAM-decorated substrates to a 5 mM solution of NBDAC in DCM for 30 min resulted in the coupling of norbornenyl groups to the underlying hydroxyl monolayer via ester linkages. Next, samples were rinsed with DCM and ethanol and dried in a stream of nitrogen. To immobilize the initiator and render the surface active for SI-ROMP, the norbornenyl decorated surfaces were exposed to a 5 mM solution of Grubbs second-generation catalyst in DCM for 10 min. Subsequently, samples were rinsed in DCM, dried with nitrogen, and immediately pressed against (load ~ 194 ± 18 mN) the h-PDMS mold filled with pure NBF8 monomer, resulting in the growth of partially fluorinated polymer films from the gold surface. To prepare the monomer-filled mold, 2 μL of NBF8 were added to the mold 30 s before removing the modified substrates from the catalyst solution. After polymerization, samples were rinsed with DCM, ethanol, and water, and dried in a stream of nitrogen.

In the latter approach, the SI-ARTP of PHEMA is similar to that reported by Brantley et al.[23] Briefly, gold substrates were exposed to a 1 mM ethanolic solution of the disulfide ATRP initiator $(BrC(CH3)_2COO(CH2)_{11}S)_2$ for 24 h. Afterward, these initiator-bearing samples were rinsed with ethanol, dried in a stream of nitrogen, and placed in vials sealed with rubber septa. These samples underwent a subsequent degassing and back-filling process with nitrogen. The polymerization mixture consisted of Cu^I/Cu^{II}/bpy (69 mM CuCl, 20 mM $CuBr_2$, 195 mM bpy) in a 50:50 v:v water/HEMA solution. These reagents were subsequently transferred to a Schlenk flask sealed with a rubber septum and exposed to a degassing process by performing three freeze-pump-thaw cycles. The solution was then transferred via cannula into the vials, where the SI-ATRP took place. After 12 h of polymerization at room temperature, samples were thoroughly rinsed with DMF and water and dried with nitrogen. The average PHEMA film thickness as measured by ellipsometry of at least 80 samples prepared from five different batches was 280 ± 14 nm. The PHEMA samples were further derivatized by exposing them to a 20 mM solution of NBDAC in DMF for 3 h. Afterwards, the modified-PHEMA substrates were rinsed with DMF, ethanol, and dried in a stream of nitrogen, followed by exposure to a 5 mM solution of Grubbs second-generation catalyst in DCM for 15 min. Subsequently, samples were rinsed with DCM and immediately pressed against (load ~ 194 ± 18 mN) the monomer-filled h-PDMS mold as described above.

The monolayer and macroinitiated polymerizations were performed both under ambient conditions and under a nitrogen atmosphere in a glove box. In general, the textured polymer films obtained by the former tended to be thinner with shorter features than the ones formed by the latter, especially at longer polymerization times (> 15 min). This may be attributed to the eventual deactivation of the initiator species by the oxygen in the environment.[24,25] Therefore, results shown in this Chapter correspond to polymerizations performed in a glove box unless otherwise indicated.

Results and Discussion

Scheme 6.1 illustrates the different steps of μMSIP to fabricate polymer coatings with microtextured surfaces that reproduce the topography of master substrates. In this case, DFEA and Klarite® were chosen because they exhibit well-defined dimensions and specific geometric shapes that are easily measured and serve as a reference to evaluate the accuracy of the reproduction process. Such features would not only allow testing the overall performance of the technique, but also help identify potential limitations. Importantly, the height of the reproduced features can be varied based on the amount of initiator employed during the polymerization process, as well as the time and temperature of the polymerization. Furthermore, the thickness of the coating at the base of the features can be controlled based on the amount of excess monomer added to the mold. Briefly, DFEA and Klarite® were molded by soft lithography to create a polymeric composite mold displaying the inverse structures of their corresponding textured surface (see Experimental Methods section for more details). Prior to the SIP step, if a nearly 100% replication of the master features is desired, initiator species are added into the mold by depositing 150 μL of a 0.7 mM solution of Grubbs catalyst in DCM and letting the solvent evaporate. This step is omitted if one seeks to control feature heights below those of the master. Immediately afterward, the mold was filled with pure NBF8, and subsequently pressed against the activated surface of the substrate from which the textured film would grow. The activation of the substrate, which is performed in advance and could be monolayer- or macroinitiator-based, was achieved by anchoring initiator species on the surface of the gold-coated silicon substrates (see Experimental Methods for details). In Chapter V, I showed that the macroinitiation approach binds more initiator molecules per geometric area than that bound by the monolayer initiation, and thus, provides another "knob" to control microfeature height.[22] Finally, the elastomeric mold bearing the textured pattern is removed, and as a result, a surface-bound pNBF8 coating that displays the surface relief of the respective master is obtained.

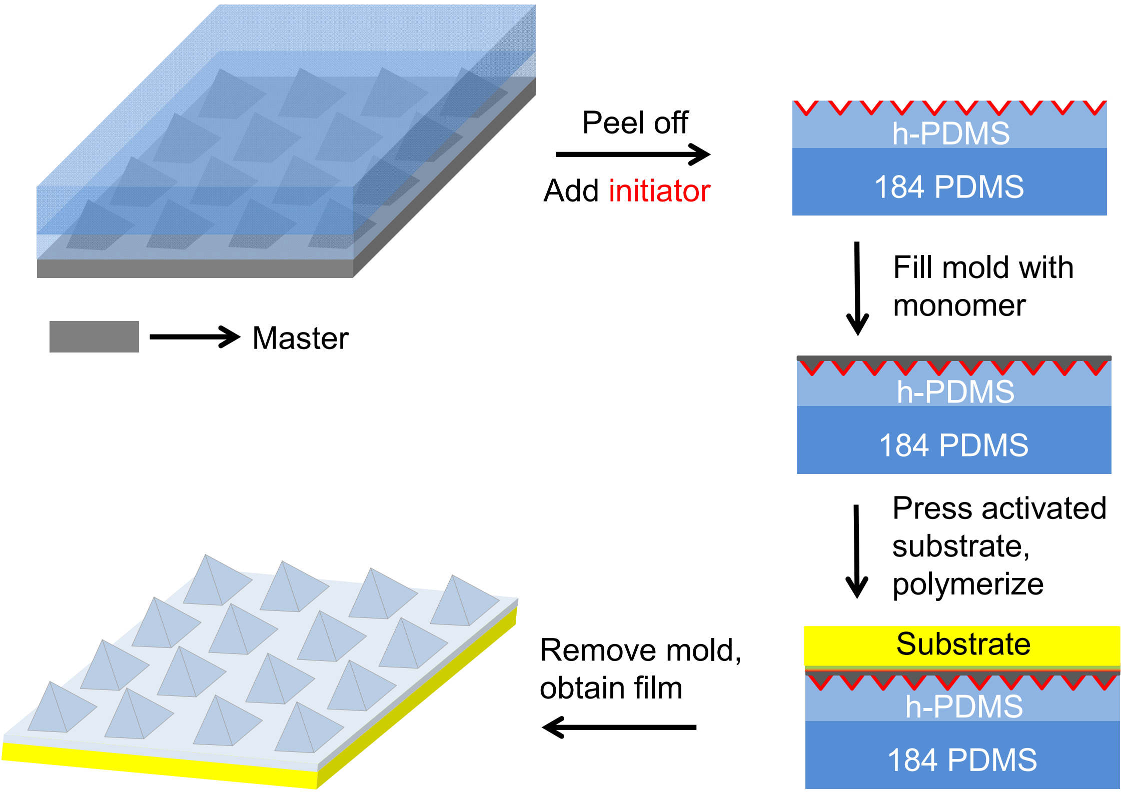

Scheme 6.1. The µMSIP process used to produce microtextured pNBF8 films.

During the SIP process, each monomer-filled pyramid represents a microreactor in which the amount of initiator can be varied systematically based on the initiation approach, including monolayer-initiation (single layer of initiator at the base of the pyramid), macroinitiation (multilayer of initiator at the base of the pyramid), and macroinitiation plus initiator added to the mold (initiator present on all surfaces). Figure 6.1 shows the effect of the polymerization time on the height of the pyramidal structures produced by μMSIP of the DFEA substrate using each of the initiation approaches. In general, the height of the pyramidal structures, which is directly related to monomer conversion, increases with the polymerization time. In Chapter V, I showed that the thickness (*d*) of pNBFn coatings increases with time based on the kinetic equation developed by Harada et al.[26] In this Chapter, we have derived an equation, in which we adopt some of the terms present in that of Harada's,[26] to estimate monomer conversion (χ):

$$\chi = 1 - \frac{C_M}{C_{M0}} = 1 - e^{\left\{\frac{K}{k_t}\left[e^{(-k_t t)}-1\right]\right\}} \tag{6.1}$$

In this equation, C_M represents the monomer concentration at a given time, t, C_{M0} is the initial monomer concentration, k_t is the termination rate constant, and the single rate term K reflects both initiation and propagation:

$$K = P_I k_p \tag{6.2}$$

where P_I represents the initial number of active initiators sites per unit area and k_p is the propagation rate. Based on this equation, I would expect the monomer conversion (feature height) in μMSIP to depend on P_I, k_p, and k_t, so that increasing initiator loading (P_I) is a way to offset terminations and yield higher conversions. Accordingly, the average height of the pyramidal structures, as measured by AFM, is the highest for those grown from a combination of macroinitiation and initiator-loaded mold (1.73 ± 0.04 μm), followed, in descending order, by those grown from a macroinitiator (0.88 ± 0.03 μm) and from a monolayer (0.64 ± 0.07 μm). The height of the pyramids reaches a plateau for both the monolayer and macroinitiator approaches after 120 and 90 min, respectively. By contrast, the height of the pyramids polymerized from the macroinitiator/initiator-loaded mold approach achieves the height of the inverse structures of the composite mold (1.73 ± 0.02 μm) within 60 min. The difference in the polymerization kinetics for these three approaches relates to the different amounts of initiator to shift the ratio of chain growth to termination. Without initiator added to the mold, the macroinitiator provides a greater areal density of initiator species on the activated substrate than that exhibited at a 2-D interface by the monolayer, in agreement with the findings in Chapter V,[22] which results in higher monomer conversions and polymer feature heights. Ultimately, chain terminations limit monomer conversion in the purely surface-initiated cases and prevent the reproduced features from matching the mold heights, as is achieved by adding a tremendous excess of initiator to the mold.

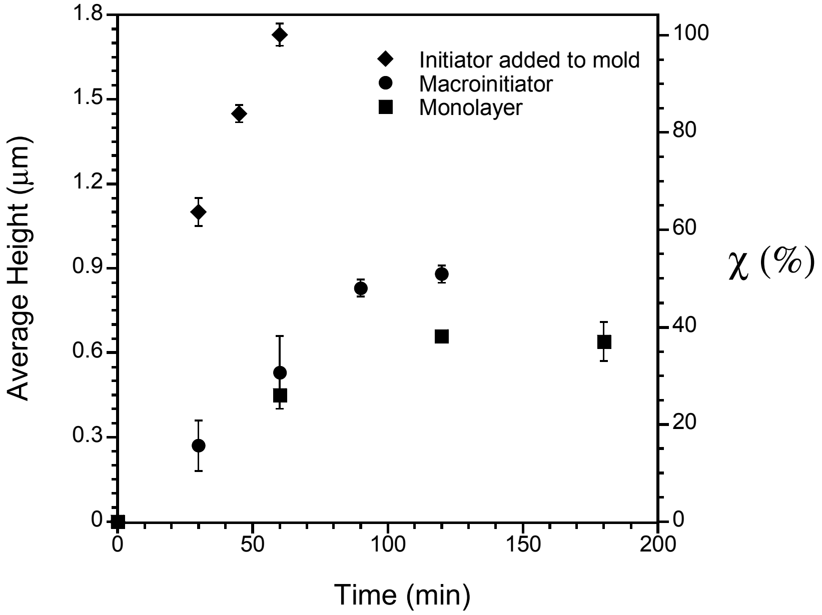

Figure 6.1. Effect of polymerization time on feature height for the three different initiation approaches, namely monolayer initiation, macroinitiation, and a combination of macroinitiation and addition of initiator to the mold. Polymerizations were performed at room temperature.

The SEM characterization of the DFEA master shown in Figure 6.2a reveals that its surface topography is comprised of pyramids with a square base set in a matrix configuration. The SEM micrograph in Figure 6.2b shows that the resulting textured pNBF8 film grown by μMSIP, through the combination of a macroinitiated polymerization (60 min) with addition of initiator to the mold, also exhibits a structured pyramidal relief resembling that of the master. It also reveals that the reproduced pyramidal structures sit atop a continuous residual pNBF8 film (see Figure 6.2f). The SEM images shown in Figures 6.2c and 6.2d illustrate the surface topography of the resulting film (Figure 6.2b) at lower magnifications, as denoted by the scale bars. Figure 6.2c shows that the reproduced surface features are homogeneously distributed and organized in a grid-like manner. Figure 6.2d shows a continuous textured film blanketing the surface of the supporting substrate across an area of ~40,000 μm^2. More strikingly and interestingly, Figures 6.2b – d show two remarkable advantages of μMSIP: first, few, if any, defects appear across the entire reproduced area or on the pyramidal structures themselves, and second, the size of the reproduced features is homogeneous. Figure 6.2e shows the atomic force microscopy line profiles of the DFEA master, the corresponding composite mold, and the resulting film. The AFM measurements of the composite mold show that its recessed structures achieved an average of 93% of the volume of those on the master (see APPENDIX B). Such disparity may be attributed to the chemical and thermal shrinkage of the h-PDMS during the curing process.[27,28] The film, which is limited by the imperfect replication of the master features by the composite mold, also achieves 93% replication of the master (Figure 6.2a). Figure 6.2f shows a cross-sectional image of the film shown in Figure 6.2b. The dark portion at the bottom of the figure represents the silicon wafer, and the bright thin line observed right above it corresponds to the gold layer. The macroinitiator film is not distinguishable because it is obscured by the thick pNBF8 film grown within and atop it. The pNBF8 film has a thickness of ~20 μm, which is due to excess monomer added to the mold. The brighter lines running horizontally across the thick film are a consequence of charge build-up and do not represent any type of interlayer films. Thus, Figure 6.2f reveals that we have indeed produced a rather thick textured coating with pyramidal features dominating the outermost surface.

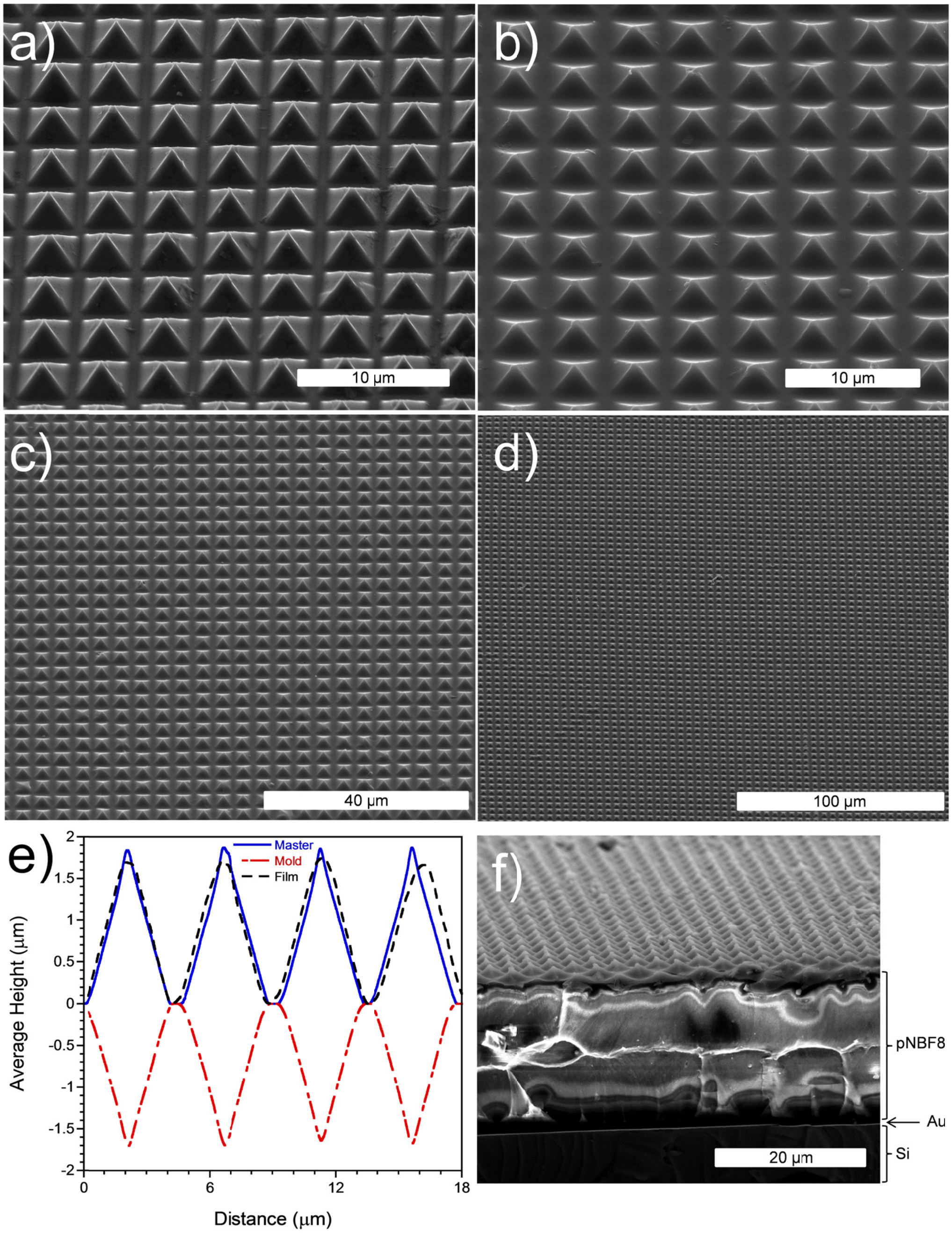

Figure 6.2. Scanning electron microscopy characterization of a) the surface morphology of DFEA master, b) resulting pNBF8 film reproducing the surface topography of the DFEA master shown in a). c) and d) scanning electron micrographs showing different length scales from b). e) AFM line profiles of DFEA master in a), composite mold, and pNBF8 film in b), f) cross-

sectional SEM image of the pNBF8 film in b). The SEM images in a), b), c), and d) were taken at a 45° angle with respect to surface parallel; f) was taken at 85°. All AFM measurements were performed in tapping mode. The error bars of the AFM line profiles are not shown for better clarity of the plot. Error is within 3.5%.

I also studied the micromorphological characteristics of the pyramid-textured films grown from a macroinitiated μMSIP process in which there was no addition of initiator species to the mold. As an example, Figures 6.3a – d show the respective SEM and AFM characterization of a macroinitiated film polymerized at 55 °C for 60 min. The SEM image in Figure 6.3a shows that the surface topography of the film is similarly comprised of pyramids with a square base set in a matrix configuration. The corresponding 3D AFM characterization of such film, shown in Figure 6.3b, indicates that the surface features are ~1 μm in height. For comparison purposes, Figure 6.3c displays the corresponding 3D AFM of the DFEA master. Figure 6.3d shows the AFM line profiles of the master, composite mold, and resulting pNBF8 film. The line profile of the pNBF8 film reveals that the polymer pyramids achieved ~ 60% of the volume of the composite mold. The incomplete conversion here indicates that the monomer:initiator ratio is sufficiently high that over time, termination reactions overcome those of propagation to limit the height of the microfeatures.

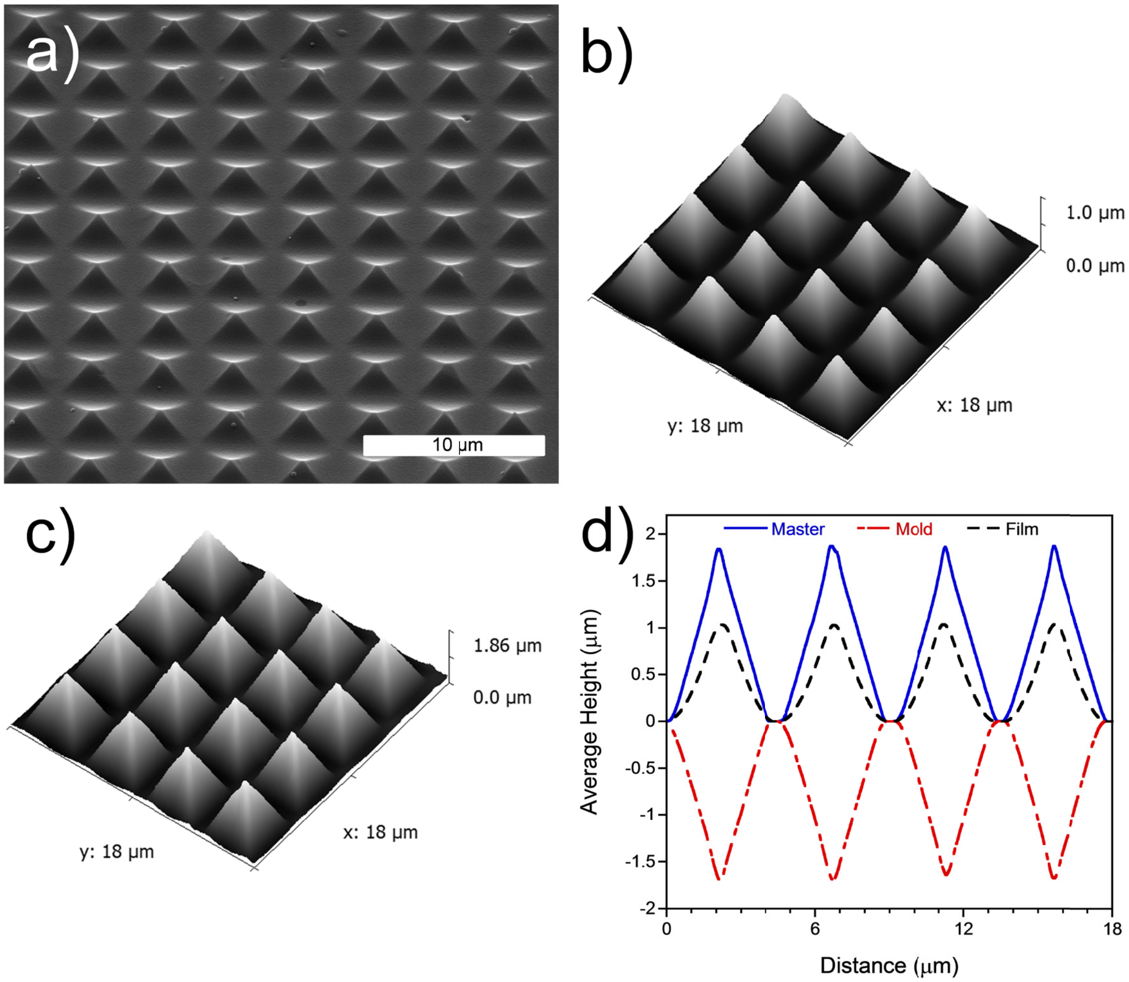

Figure 6.3. Surface topography characterization of a textured film polymerized solely from a macroinitiator at 55 °C for 1 h. a) Scanning electron microscopy image showing the surface morphology of the resulting film. b) 3D AFM image of the film in a), c) 3D AFM image of DFEA master, d) AFM line profiles of DFEA master, h-PDMS mold, and pNBF8 film. The SEM images were taken at a 45° angle with respect to surface parallel. All AFM measurements were performed in tapping mode. The error bars of the AFM line profiles are not shown for better clarity of the plot. Error is within 3.5%.

The SEM image in Figure 6.4a shows that Klarite® exhibits inverted square pyramidal topography in which the structures are distributed in a grid-like fashion. Figure 6.4c shows a 3D AFM image of the surface topography of Klarite®, whose measurements are summarized in Table B.1 in APPENDIX B. Figure 6.4b shows the resulting textured pNBF8 film by a macroinitated μMSIP process (55 °C, 60 min), displaying the similar inverted pyramidal topography as the master, and demonstrating the versatility of μMSIP to prepare these inverted structures exhibiting surface cavities. Figure 6.4d shows the AFM line profiles of the master, composite mold, and resulting pNBF8 film. When compared to the composite mold, the structures in the film achieved ~ 63% of the corresponding height under these conditions.

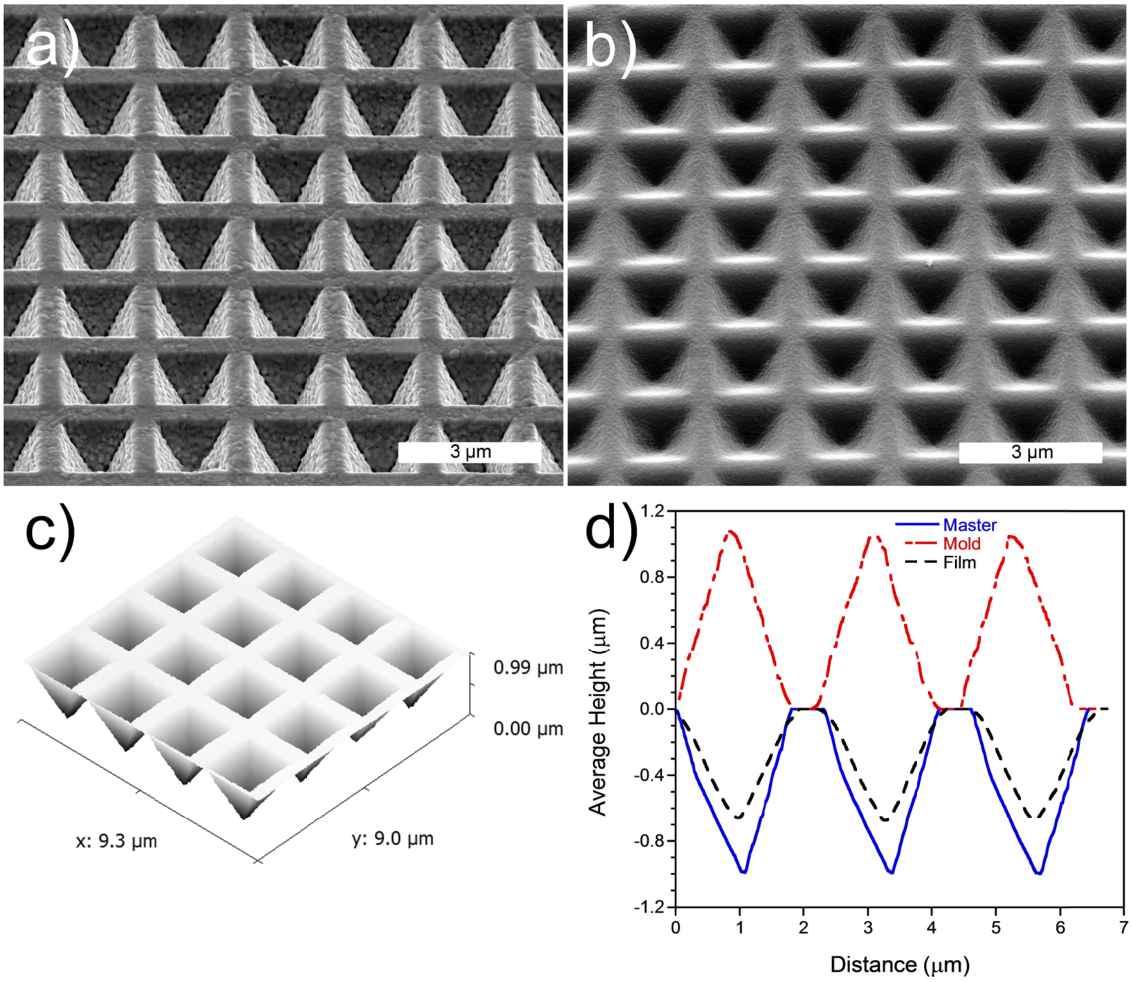

Figure 6.4. Surface topography characterization of Klarite® and its corresponding μMSIP film. Scanning electron microscopy image of a) the surface morphology of Klarite® master, b) resulting polymer film, c) 3D AFM image of Klarite® master, d) AFM line profiles of Klarite® master, composite mold, and pNBF8 film. All AFM images were taken in tapping mode. The SEM images were taken at a 45° angle with respect to surface parallel. Error bars are not shown for better clarity of the plot. Error is within 3.5%.

Figure 6.5 shows the effect of temperature on the height of the pyramidal structures prepared by μMSIP of a DFEA master. The plots show the results for textured films prepared by either a monolayer-initiated (a) or a macroinitiation (b) approach. In Chapter V, I showed that higher temperatures accelerate the growth of pNBF8 films since the propagation reaction has a higher activation energy than the termination reaction.[22] In this case, polymerizations were performed at three temperatures, namely 21, 40, and 55 °C. In general, for both polymerization approaches, the height of the resulting pyramids increases as temperature increases. For example, a change in polymerization temperature from 21 to 55 °C increased the average height of the pyramids by a factor of ~ 2.17 and 1.46 for the monolayer and macroinitiation approaches, respectively. Such an effect could be attributed to an increase in the activity of the initiator with an increase in temperature.[22,24,29] The average height of the pyramids formed by the macroinitiation approach is greater than those formed by a monolayer initiation at all temperatures, but the difference in average height between monolayer-initiated and macroinitiated pyramids decreases from 0.27 to 0.07 μm, as temperature increases from 21 to 55 °C. This trend suggests that the macroinitiation of pure NBF8 molecules becomes less effective relative to monolayer initiation at higher temperatures. Since the activity of the initiator increases with an increase in temperature, those initiator species located nearest the interface react extremely fast to form a growing polymer front that may rapidly occlude those initiators located deeper within the macroinitiator film. Consequently, the macroinitiation resembles the 2-D monolayer initiation as the propagation rate increases.

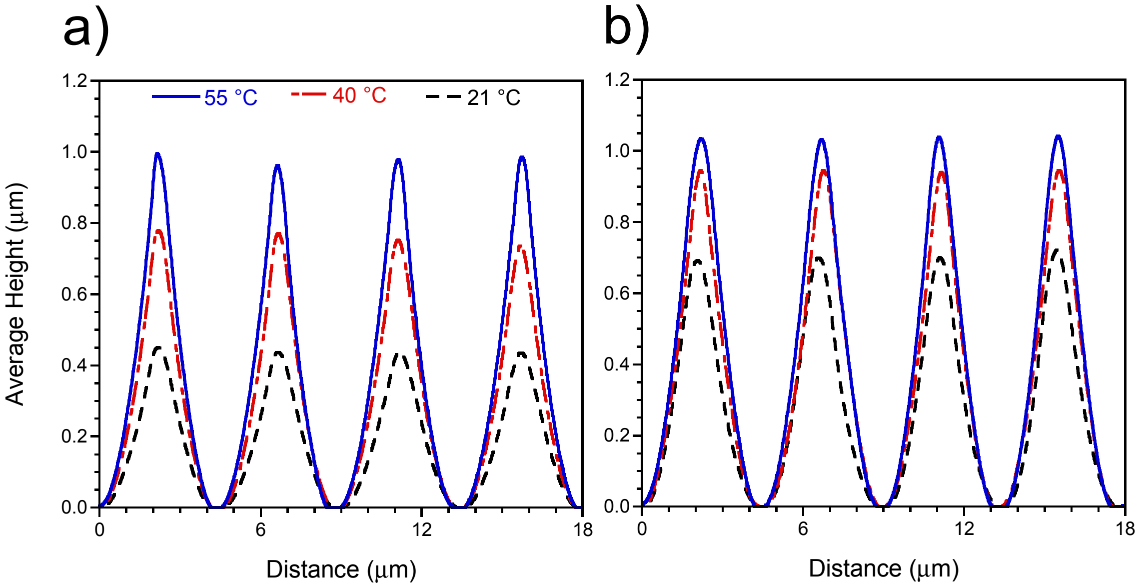

Figure 6.5. Temperature effects on the growth of pyramidally-textured pNBF8 films formed from a monolayer (a) or a macroinitiation (b) approach. Polymerzations were performed for 1 h in all cases. Error bars are not shown for better clarity of the plot. Error is within 3.5%.

The μMSIP approach takes advantage of the fact that the conversion of the monomer is controlled by the type of initiation approach used (see Figure 6.1) to fabricate generational, pyramid-textured films in which the surface features maintain the same base size footprint, but whose height can be modulated after each generation. μMSIP achieves this effect by means of sequential molding and polymerization processes. Figure 6.6 shows AFM line profiles of three generational films prepared by macroinitiated μMSIP and the composite molds. The first generation film, derived from the first generation composite mold of the master, is used to create a second generation composite mold, which in turn is used to perform a subsequent μMSIP process to produce a second generation textured film, and so on. AFM measurements show that, for this particular case in which polymerizations were performed from a macroinitiator at 55 °C for 1 h, the average height of the pyramids is reduced by 43% (± 4%) after each generation to enable pyramid heights of 0.53 ± 0.09 and 0.35 ± 0.02 μm, for the second and third generations, respectively, which are 3.2- and 4.9-fold lower than the height of the master pyramids. The ability to reduce feature heights generationally provides yet another means to control the microscale topography of the surface of the coatings.

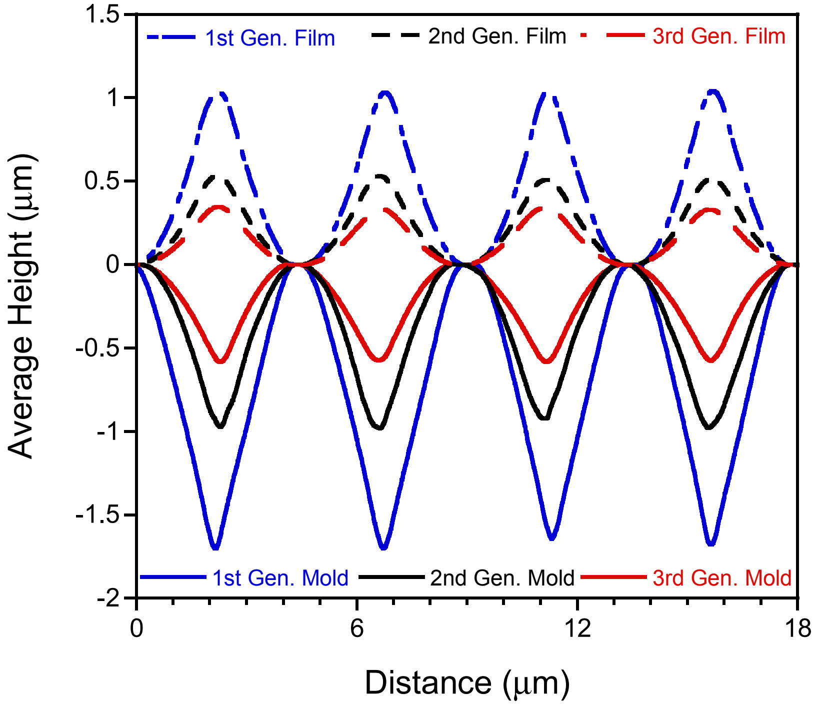

Figure 6.6. Atomic force microscopy line profiles of generational textured films and molds. Line profiles correspond to macroinitiated films polymerized at 55 °C for 1 h. Error bars are not shown for better clarity of the plot. Error is within 3.5%.

Conclusions

This Chapter introduces an innovative and versatile process termed µMSIP that enables the fabrication of microscale-textured, surface-bound polymer coatings by combining soft lithography and surface-initiated polymerization techniques. µMSIP enables the formation of polymer films exhibiting either high-relief or recessed topographies. The choice of initiation approach, e.g., monolayer or macroinitiator, had marked effects on the height (monomer conversion) of the resulting surface features. Other process variables such as polymerization time and temperature had a direct effect on the final height of the features as well. SEM images showed that the resulting films were uniform in quality and exhibited homogeneous surface structures across large areas. AFM measurements revealed a high level of uniformity in terms of feature footprint and height. Furthermore, the versatility of μMSIP, which relies on the capability and simplicity to manipulate any of the variables noted above, allows the modulation or fine-tuning of the height of the final polymer surface features and enables the preparation of generationally textured films.

References

(1) del Campo, A.; Arzt, E. Fabrication Approaches for Generating Complex Micro- and Nanopatterns on Polymeric Surfaces. *Chemical Reviews* **2008,** 108, 911-945.

(2) Bixler, G. D.; Bhushan, B. Bioinspired Rice Leaf and Butterfly Wing Surface Structures Combining Shark Skin and Lotus Effects. *Soft Matter* **2012,** 8, 11271-11284.

(3) Xia, Y. N.; Kim, E.; Zhao, X. M.; Rogers, J. A.; Prentiss, M.; Whitesides, G. M. Complex Optical Surfaces Formed by Replica Molding Against Elastomeric Masters. *Science* **1996,** 273, 347-349.

(4) Xiaosheng, Z.; Qianli, D.; Fuyun, Z.; Guangyi, S.; Haixia, Z. Wideband Anti-Reflective Micro/Nano Dual-Scale Structures: Fabrication and Optical Properties. *Micro & Nano Letters, IET* **2011,** 6, 947-950.

(5) Pan, S.; Kota, A. K.; Mabry, J. M.; Tuteja, A. Superomniphobic Surfaces for Effective Chemical Shielding. *Journal of the American Chemical Society* **2013,** 135, 578-581.

(6) Tuteja, A.; Choi, W.; Ma, M.; Mabry, J. M.; Mazzella, S. A.; Rutledge, G. C.; McKinley, G. H.; Cohen, R. E. Designing Superoleophobic Surfaces. *Science* **2007,** 318, 1618-1622.

(7) Thickett, S. C.; Neto, C.; Harris, A. T. Biomimetic Surface Coatings for Atmospheric Water Capture Prepared by Dewetting of Polymer Films. *Advanced Materials* **2011,** 23, 3718 - 3722.

(8) Wu, D.; Wang, J.-N.; Wu, S.-Z.; Chen, Q.-D.; Zhao, S.; Zhang, H.; Sun, H.-B.; Jiang, L. Three-Level Biomimetic Rice-Leaf Surfaces with Controllable Anisotropic Sliding. *Adv. Funct. Mater.* **2011,** 21, 2927 - 2932.

(9) LaFratta, C. N.; Baldacchini, T.; Farrer, R. A.; Fourkas, J. T.; Teich, M. C.; Saleh, B. E. A.; Naughton, M. J. Replication of Two-Photon-Polymerized Structures with Extremely High Aspect Ratios and Large Overhangs. *The Journal of Physical Chemistry B* **2004,** 108, 11256-11258.

(10) Fujii, T.; Iwasaki, K.; Munekane, M.; Takeuchi, T.; Hasuda, M.; Asahata, T.; Kiyohara, M.; Kogure, T.; Kijima, Y.; Kaito, T. A Nanofactory by Focused Ion Beam. *Journal of Micromechanics and Microengineering* **2005,** 15, S286-S291.

(11) Manz, A.; Becker, H.; Qin, D.; Xia, Y.; Rogers, J.; Jackman, R.; Zhao, X.-M.; Whitesides, G. Microfabrication, Microstructures and Microsystems. In *Microsystem Technology in Chemistry and Life Science*; Springer Berlin / Heidelberg: **1998**; Vol. 194, p 1-20.

(12) Xia, Y. N.; Whitesides, G. M. Soft Lithography. *Annu. Rev. Mater. Sci.* **1998,** 28, 153-184.

(13) Jennings, G. K.; Brantley, E. L. Physicochemical Properties of Surface-Initiated Polymer Films in the Modification and Processing of Materials. *Adv. Mater.* **2004,** 16, 1983-1994.

(14) Faulkner, C. J.; Fischer, R. E.; Jennings, G. K. Surface-Initiated Polymerization of 5-(Perfluoro-n-alkyl)norbornenes from Gold Substrates. *Macromolecules* **2010,** 43, 1203-1209.

(15) Weck, M.; Jackiw, J. J.; Rossi, R. R.; Weiss, P. S.; Grubbs, R. H. Ring-Opening Metathesis Polymerization from Surfaces. *J. Am. Chem. Soc.* **1999,** 121, 4088-4089.

(16) Juang, A.; Scherman, O. A.; Grubbs, R. H.; Lewis, N. S. Formation of Covalently Attached Polymer Overlayers on Si(111) Surfaces Using Ring-Opening Metathesis Polymerization Methods. *Langmuir* **2001,** 17, 1321-1323.

(17) Bielawski, C. W.; Grubbs, R. H. Living Ring-Opening Metathesis Polymerization. *Prog. Polym. Sci.* **2007,** 32, 1-29.

(18) Leitgeb, A.; Wappel, J.; Slugovc, C. The ROMP Toolbox Upgraded. *Polymer* **2010,** 51, 2927-2946.

(19) Slugovc, C. The Ring Opening Metathesis Polymerisation Toolbox. *Macromol. Rapid Commun.* **2004,** 25, 1283-1297.

(20) Sutthasupa, S.; Shiotsuki, M.; Sanda, F. Recent Advances in Ring-Opening Metathesis Polymerization, and Application to Synthesis of Functional Materials. *Polym. J.* **2010,** 42, 905-915.

(21) Buchmeiser, M. R. Metathesis Polymerization to and from Surfaces. In *Surface-Initiated Polymerization I*; Jordan, R., Ed.; Springer-Verlag Berlin: Berlin, **2006**; Vol. 197, p 137-171.

(22) Escobar, C. A.; Harl, R. R.; Maxwell, K. E.; Mahfuz, N. N.; Rogers, B. R.; Jennings, G. K. Amplification of Surface-Initiated Ring-Opening Metathesis Polymerization of 5-(Perfluoro-n-alkyl)norbornenes by Macroinitiation. *Langmuir* **2013,** 29, 12560-12571.

(23) Brantley, E. L.; Jennings, G. K. Fluorinated Polymer Films from Acylation of ATRP Surface-Initiated Poly(hydroxyethyl methacrylate). *Macromolecules* **2004,** 37, 1476-1483.

(24) Bielawski, C. W.; Grubbs, R. H. Highly Efficient Ring-Opening Metathesis Polymerization (ROMP) Using New Ruthenium Catalysts Containing N-Heterocyclic Carbene Ligands. *Angew. Chem.* **2000,** 39, 2903 - 2906.

(25) Love, J. A.; Sanford, M. S.; Day, M. W.; Grubbs, R. H. Synthesis, Structure, and Activity of Enhanced Initiators for Olefin Metathesis. *J. Am. Chem. Soc.* **2003,** 125, 10103-10109.

(26) Harada, Y.; Girolami, G. S.; Nuzzo, R. G. Catalytic Amplification of Patterning via Surface-Confined Ring-Opening Metathesis Polymerization on Mixed Primer Layers Formed by Contact Printing. *Langmuir* **2003,** 19, 5104-5114.

(27) Choi, K. M.; Rogers, J. A. A Photocurable Poly(dimethylsiloxane) Chemistry Designed for Soft Lithographic Molding and Printing in the Nanometer Regime. *Journal of the American Chemical Society* **2003,** 125, 4060-4061.

(28) Hui, C. Y.; Jagota, A.; Lin, Y. Y.; Kramer, E. J. Constraints on Microcontact Printing Imposed by Stamp Deformation. *Langmuir* **2002,** 18, 1394-1407.

(29) Perring, M.; Bowden, N. B. Assembly of Organic Monolayers on Polydicyclopentadiene. *Langmuir* **2008,** 24, 10480-10487.

CHAPTER VII

REPRODUCING NATURE'S SUPERHYDROPHOBIC SURFACES BY MICROMOLDING SURFACE-INITIATED POLYMERIZATION

Introduction

In recent years, nature and its remarkably optimized designs, acquired through millions of years of evolution, have provided endless sources of inspiration for researchers who seek solutions or ideas to address specific challenges.[1-5] For example, Thickett et al.[1] used a dewetting process to create a combination of hydrophilic polymer domains on a hydrophobic polymer background, inspired by that found on the exoskeleton of the *Stenocara* beetle, to efficiently collect water from dry environments. In a similar manner, Zhiwu et al.[2] reported a bionic method to minimize the damage caused by solid particle erosion in mechanical components, inspired by the erosion resistance exhibited by the morphology and structure of the dorsal surface of the mesosoma of the desert scorpion (*Androctonus australis*). In a different application, Noone et al.[3] introduced a biomimetic arrangement based on the spirals of the phyllotaxis disc pattern, which is similar to the configuration exhibited by the florets on the head of a sunflower, that improves the efficiency and reduces the land area of heliostat fields by 0.36% and 15.8%, respectively. Likewise, Wong et al.[4] were inspired by the *Nepenthes* pitcher plant to design liquid-repellent surfaces that use a microtextured substrate to lock-in a lubricating liquid in order to not only achieve omniphobicity, but also be self-repairing and function at high pressures. Moreover, the superhydrophobic character and self-cleaning capability demonstrated by a large number of plant leaves are the driving forces behind numerous attempts of using these biological structures as templates for the fabrication of superhydrophobic surfaces.[6-8] Methods to mimic these surfaces include soft lithography,[7] lithography of silicon wafers,[6] UV-nanoimprint lithography,[9] etching,[10] and membrane casting.[11]

In this Chapter, I report on the extendibility of micromolding surface-initiated polymerization (μMSIP), which is a versatile process used for the fabrication of textured polymer films, to fabricate polymer coatings that reproduce the surface topography of superhydrophobic leaves onto solid supports. μMSIP comprises a soft lithographic molding process and a surface-initiated polymerization (SIP). This technique is used not only to reproduce the highly evolved and functional surface architectures of Nature, but also to provide tremendously greater versatility in chemical composition, as the building blocks of Nature are limited to hydrocarbons. Accordingly, the resulting bioreplicated, surface-bound polymer coatings are obtained by means of the mold-confined, surface-initiated ring-opening metathesis polymerization (SI-ROMP) of 5-(perfluorooctyl)norbornene (NBF8), which exhibits a critical surface tension of 9 mN/m.[12] The replication of Nature's engineered, microscopically rough, and highly functional surfaces onto a solid substrate through an SIP technique provides polymer coatings with the necessary long-term stability, i.e., the capability to withstand external chemical and physical conditions that may diminish their integrity or performance.[13] While efforts to replicate superhydrophobic and self-cleaning surfaces have been largely successful,[7,9,14] the resulting products are hand-held, peel-away materials and not surface-bound coatings. Superhydrophobic surfaces have potential applications as self-cleaning surfaces,[6,15] water-repellent textiles,[15] ice-resistant coatings,[16] interfacial slip,[17] and in drag reduction.[18]

μMSIP involves the molding of the superhydrophobic leaf with an elastomeric composite comprising hard-PDMS (h-PDMS) and Sylgard 184 PDMS to produce a negative replica exhibiting the corresponding inverted structures of the surface of the leaf. Afterward, initiator species are added into the mold by depositing dilute solution of the initiator in diethyl ether and letting the solvent evaporate. The activated mold is then filled with pure monomer and subsequently pressed against an activated surface, i.e., a surface containing anchored initiator species to promote an SIP. As the polymerization progresses, both the surface-tethered growing polymer chains and those grown from the mold start filling the inverted structures, thereby reproducing the corresponding surface features. Representative examples of polymeric films obtained through μMSIP include those replicating the surface topography of *Trifolium repens* (White Clover) and *Aristolochia esperanzae* (Dutchman's Pipe).

Experimental Methods

Preparation of Leaves for Scanning Electron Microscopy (Fixing)

Leaves underwent a primary fixation step by exposing them to 1% paraformaldehyde and 1.25% gluteraldehyde in 0.1 M sodium cacodylate buffer (pH 7.1) at room temperature for 2 – 4 h. Afterward, the leaves were rinsed three times with a 0.1 M sodium cacodylate buffer pH (7.1) at room temperature. Subsequently, the leaves underwent a secondary fix by exposing them to 1% osmium tetroxide in 0.1 M sodium cacodylate buffer (pH 7.1) at room temperature for 15 min. Warning: osmium tetroxide is a dangerous chemical; wear the appropriate protective personal equipment and use a fume hood when working with it. Afterward, the leaves were washed three times with 0.1 M sodium cacodylate buffer (pH 7.1) at room temperature. The leaves were dehydrated in an aqueous solution containing increasing concentrations of ethanol as follows: 25% – 1 h, 50% – 1 h, 75% – 0.5 to 0.75 h, 95% – 1 h, 100% – 1 h, 100% – 1 h, 100% – 1 h. Finally, the samples were dried using a Polaron critical point dryer.

Molding

The molds bearing the inverse pattern of the master leaves, *Trifolium repens* and *Aristolochia esperanzae*, were produced by means of soft lithography. Only freshly cut, fully developed leaves were used. Samples of 10 mm × 10 mm, cut from the center of the leaf lamina, were affixed to the bottom of a plastic petri dish (5 cm in diameter) by double-sided adhesive tape to ensure a fully extended, flat surface. Once secured, a drop of tetraethoxysilane was added onto the leaf masters to create a thin layer on the surface of the masters that prevents the resulting mold from adhering to it. The molding process, which yields a polymeric composite comprising hard-PDMS (h-PDMS) and Sylgard 184 PDMS, proceeded as follows: 3.4 g of [(7–8% vinylmethylsiloxane)-(dimethylsiloxane)] copolymer, two drops of 1, 3, 5, 7-tetramethylcyclotetrasiloxane, and 1 drop of platinum divinyltetramethyldisiloxane were thoroughly mixed for at least 8 min with a glass rod in a weighing boat. During mixing, air bubbles are trapped within the mixture; to remove these, the weighing boat was placed in a desiccator connected to a vacuum line and evacuated until bubbles were no longer visible. As pressure decreases, bubbles start to expand and rise. Therefore, to prevent any spilling while degassing, vacuum was broken and restored several times. Subsequently, 1 g of [(25–30% methylhydrosiloxane)-(dimethylsiloxane)] was added to the degassed mixture and rapidly stirred with the glass rod for 3 min. The mixture was poured onto the petri dishes containing the masters and placed once again in a desiccator connected to a vacuum line to remove the entrapped bubbles resulting from the rapid mixing. Similarly, vacuum was broken and restored several times. To cure the h-PDMS, the petri dishes containing the leaf masters were placed in an oven at 60 °C for 10 min. During the curing process, a mixture of Sylgard polymer base (4.0 g) and curing agent (0.4 g) was added to a weighing boat and was thoroughly mixed using a glass rod for at least 8 min. Once the h-PDMS was cured, the petri dishes were removed from the oven and the freshly prepared Sylgard 184 PDMS/curing agent mixture was poured onto them. As in the previous step, the petri dishes were placed in a desiccator for degassing. Once free of bubbles, these were placed in an oven set at 60 °C and allowed to cure for 6 h. The resulting molds, exhibiting two layers, namely h-PDMS (~ 1 mm thick) and Sylgard 184 PDMS (~ 2 mm thick), were removed by gently breaking the entire wall surrounding the petri dish with pliers and carefully peeling them off the masters. The composite elestomeric molds were also exposed to the vapor of TFOCS for 20 min in order to facilitate the separation of the substrate from the mold after polymerization.

Polymerization

SI-ROMP was initiated from an initiator-activated self-assembled monolayer (SAM). Briefly, the gold-coated silicon samples were exposed to a 1 mM ethanolic solution of 4–mercapto–1–butanol for at least 1 h to create a hydroxyl-terminated SAM on the gold surface. Afterwards, samples were rinsed in ethanol and dried in a stream of nitrogen. Subsequent exposure of the SAM-decorated substrates to a 5 mM solution of NBDAC in DCM for 30 min resulted in the coupling of norbornenyl groups to the underlying hydroxyl monolayer via ester linkages. Next, samples were rinsed with DCM and ethanol and dried in a stream of nitrogen. To immobilize the initiator and render the surface active for SI-ROMP, the norbornenyl decorated surfaces were exposed to a 5 mM solution of Grubbs second-generation catalyst in DCM for 10 min. While the substrates were immersed in such solution, initiator species were added to the composite mold by depositing 200 μL of a 3 mM solution of Grubbs catalyst in diethyl ether and letting the solvent evaporate. After activation, samples were rinsed with DCM and immediately pressed against (load ~194 ± 18 mN) the initiator-containing composite mold filled with pure NBF8 monomer (5 μL of NBF8 were added to the mold 1 – 2 seconds before pressing the substrate against the mold), resulting in the growth of partially fluorinated polymer films from the gold surface. After polymerization, the coatings were rinsed with DCM, ethanol, and water, and dried in a stream of nitrogen. The polymerization process was performed under ambient conditions.

Results and Discussion

Scheme 7.1 illustrates the different steps of μMSIP to create polymer coatings that reproduce the structures and topography of the master substrates. In this case, *Trifolium repens* and *Aristolochia esperanzae* were chosen because they provide both high equilibrium water contact angles and different complex surface topographies. Briefly, each master leaf was molded by soft lithography to create a polymeric composite mold displaying the inverse structures of their corresponding textured surface (see Experimental Methods for details). Initiator species were added into the mold by depositing a dilute solution of Grubbs catalyst in diethyl ether and letting the solvent evaporate. Immediately afterward, the mold was filled with pure NBF8, and subsequently pressed against the activated surface of the substrate from which the textured film would grow. The substrate was activated in advance by anchoring initiator species on the surface of the gold-coated silicon substrates (see Experimental Methods for details). Finally, the composite mold bearing the textured pattern was removed after 20 min, and as a result, a surface-bound pNBF8 film displaying the surface relief of the respective master was obtained. As seen from Scheme 7.1, one of the advantages of μMSIP is that the fabrication of polymer coatings is a fast, straight forward process once the reusable composite mold has been prepared.

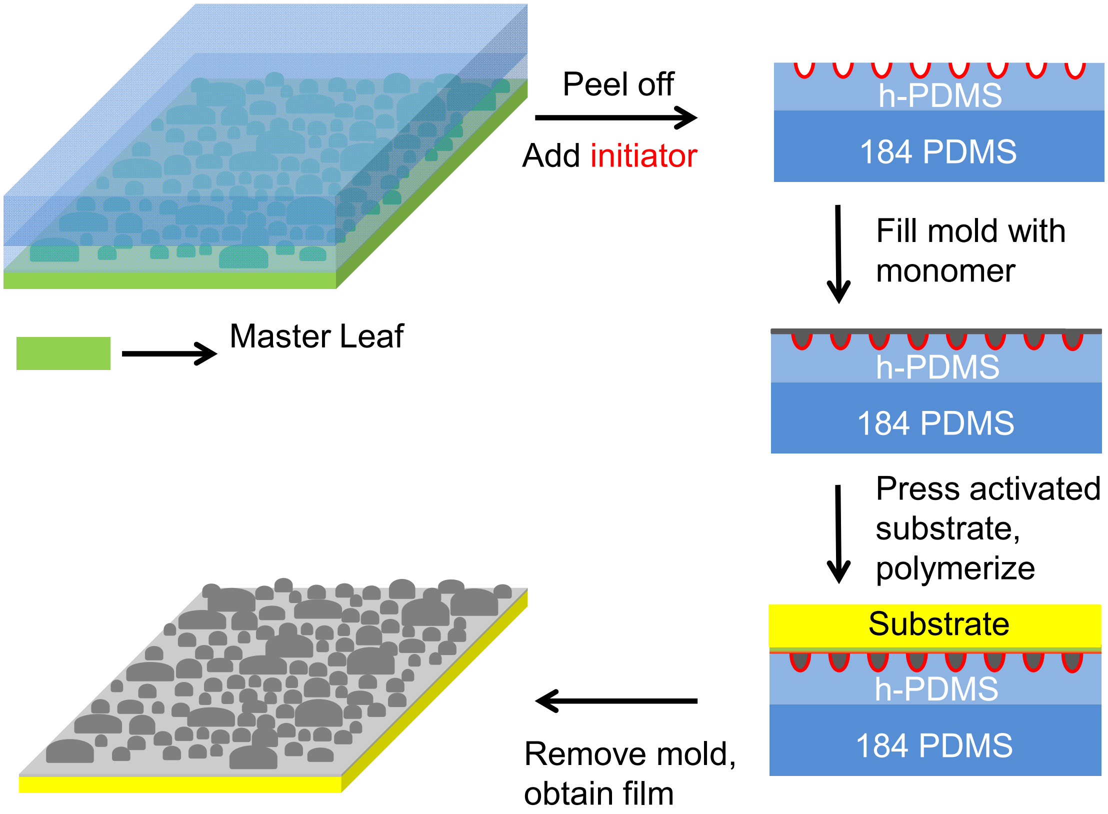

Scheme 7.1. The μMSIP process used to produce microtextured pNBF8 films that reproduce the surface topography of superhydrophobic leaves.

Figure 7.1 shows the morphological characteristics of the fixed *Trifolium repens* leaf and a pNBF8 film at different magnifications and angles of inclination. Figures 7.1a and 7.1b show a low magnification, tilted view of the fixed leaf and coating, respectively. The epidermal surface of the leaf displays a structured relief comprised of convex epidermal cells. Likewise, the topography of the pNBF8 film obtained by μMSIP shows a microrelief consisting of dome-shaped structures. In both images the relief appears densely packed over large areas without observable defects. Figures 7.1c and 7.1d show a top view, magnified image of the leaf and the resulting polymer coating, respectively. Figure 7.1c reveals elongated epidermal cells exhibiting, in some cases, a pointy-like top, and the stomata (pores on the epidermis of the leaf that control gas exchange), represented by the dark-colored structures appearing in between some of the epidermal cells. Remarkably, the polymer structures that dominate the surface of the coating (Figure 7.1d) exhibit similar shapes and sizes as compared to those present on the leaf. Quantitative measurements, performed by means of image analysis of Figures 7.1c and 7.1d, reveal that the average length and width of the larger surface structures on both the leaf and the coating are, within error, the same. For example, the length and width of the natural structures (epidermal cells) are 28 ± 3 and 19 ± 2 μm, respectively; those of the coating are 30 ± 3 and 20 ± 3 μm, respectively. Stomata features on the coating are on average 30 and 10% wider and lengthier than those on the leaf. Further comparison between the morphology of the leaf and that of the coating shows that the features on the coating appear to be connected at the base, whereas the boundaries of each epidermal cell on the leaf are well defined. This may be a consequence of the h-PDMS mix not being able to entirely penetrate through the space separating the epidermal structures. In general, the only structures that exhibit orientation on the leaf surface are those epidermal cells close to or that form the veins of the leaf; the rest are randomly oriented. In Figure 7.2c, the epidermal cells running diagonally from the bottom left to the top right, and those on the top left and bottom right are examples of the former and the latter, respectively. Polymer structures in Figure 7.2d do not show any orientation in particular as the imaged area of the coating is not near the veins. Figures 7.1e and 7.1f show zoomed-in tilted images of the leaf and coating, respectively. The images show a regular relief with connected features of varying height. Figure 7.1f shows that the tips of some structures have defects (holes), that I attribute to areas in the composite mold lacking a uniform layer of fluorinated silane that was employed to prevent adherence.

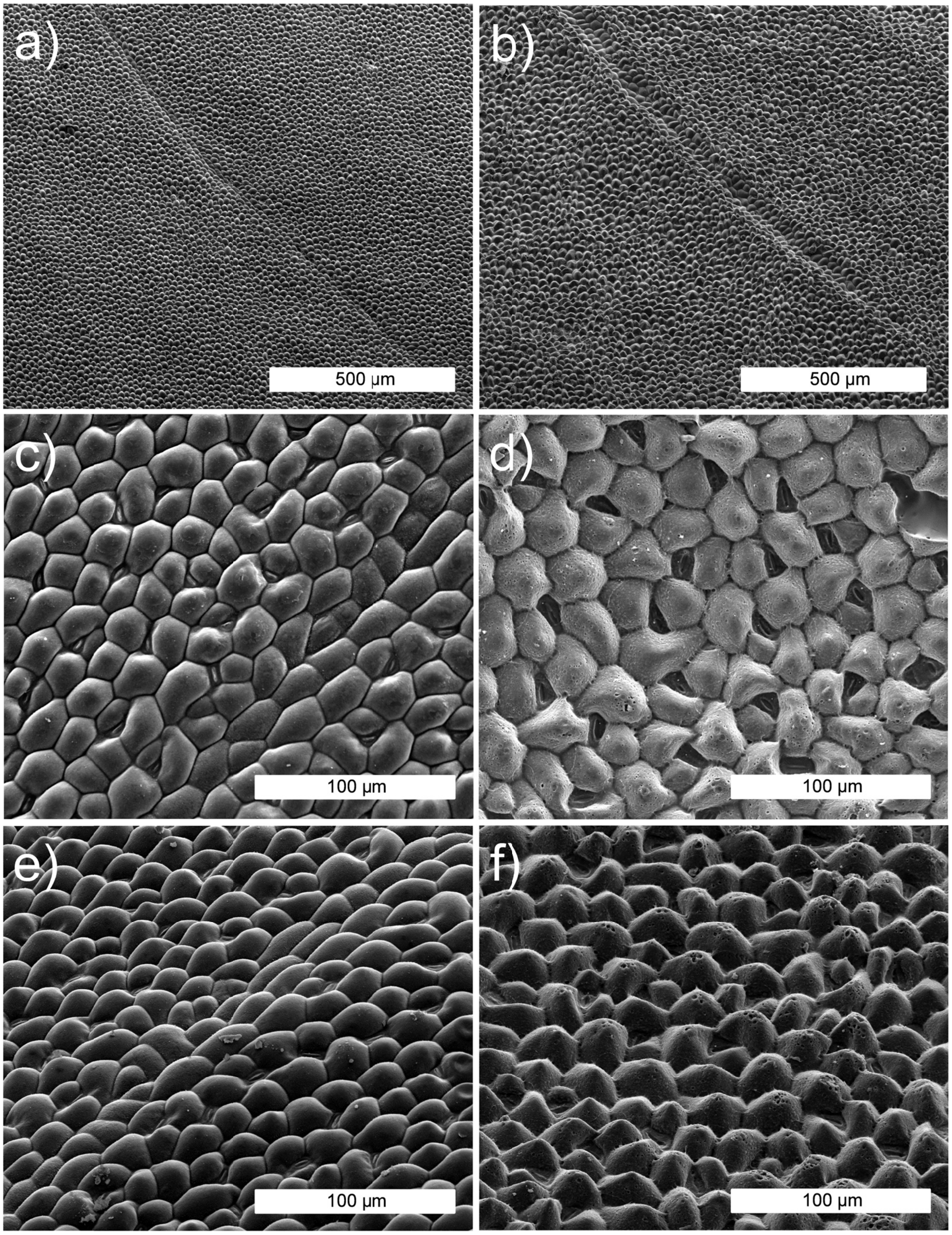

Figure 7.1. Scanning electron microscopy images showing the morphological characteristics of the adaxial surface of a fixed *Trifolium repens* leaf and its corresponding pNBF8 textured film. Tilted images (a, b, e, and f) were taken at 45° with respect to the surface parallel. The polymer coating was not produced from the leaf shown in a), c), and e).

Figure 7.2 shows the morphological characteristics of the *Aristolochia esperanzae* leaf and its corresponding pNBF8 coating at different magnifications and angles of inclination. By contrast to the epidermal relief of *Trifolium repens*, the individual epidermal cells present on the surface of the *Aristolochia esperanzae* leaf exhibit a more heterogeneous geometry (Figure 7.2a). The Y-shaped structure that appears in both Figures 7.2a and 7.2b (polymer coating) corresponds to a vein in the leaf. Figures 7.2c and 7.2d show a top view, magnified image of the leaf and the resulting polymer film, respectively. Figure 7.2c reveals epidermal cells exhibiting irregular, randomly oriented shapes. Interestingly, star-like features are formed when one sloped-end of several (usually six) epidermal cells come together. These shapes can be seen at the middle, bottom middle, top right, and top left of Figure 7.2c. These features also appear in the polymer coating, and can be discerned at the middle left and bottom right of Figure 7.2d. Although the surface structures present both on the leaf and the coating do not exhibit well-defined dimensions, a quantitative approximation of their length and width, done by image analysis of Figures 7.2c and 7.2d, reveals that these have similar ranges in both the leaf and the coating. For example, the scale of the length and width of the epidermal cells ranges from 36 to 57 and 15 to 33 μm, respectively; those of the coating range from 36 to 81 and 16 to 32 μm, respectively. Figure 7.2e shows a magnified image of the surface of the leaf and reveals that short epicuticular waxes (white hair-like structures) dominate the surface of some epidermal cells. The fact that some areas of the surface lack these structures may be explained as a consequence of the fixing and sputtering procedures. Reports by Neinhuis et al.,[19] show that epicuticular waxes are fragile structures that can be easily altered by external factors. By contrast to the fixed leaf, the surface of the features present on polymer coating (Figure 7.2f) has few, if any, of these structures. A plausible explanation for this is that during the separation of the composite mold from the leaf, the epicuticular waxes may become detached and remain embedded into the composite mold. Consequently, submicroscale recesses in the composite mold become clogged, preventing any growth of polymer inside them. A small percentage of these submicroscale features are not clogged as evidenced by some sporadic polymer growth atop features as shown in Figures 7.2d and 7.2f.

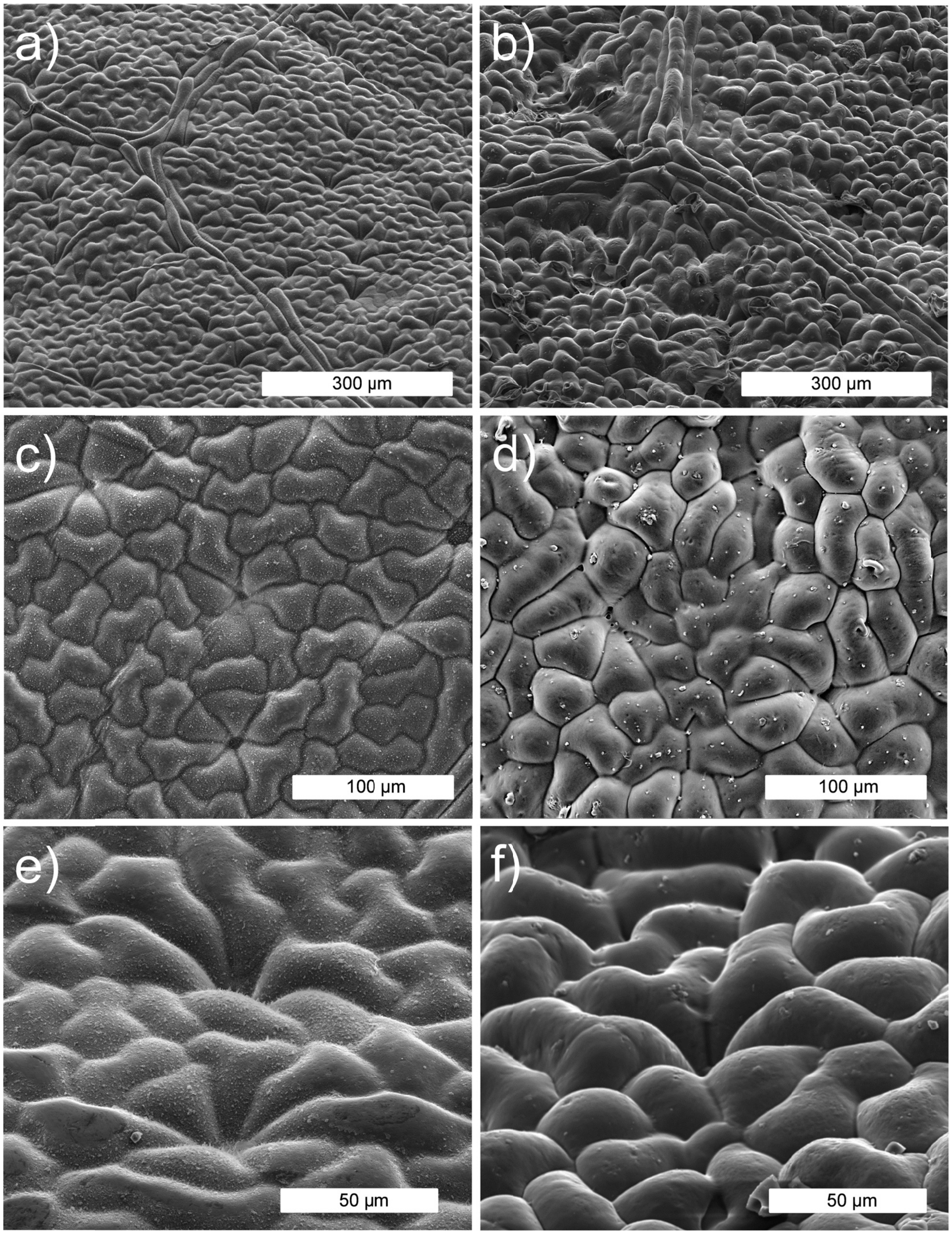

Figure 7.2. Scanning electron microscopy images showing the morphological characteristics of the adaxial surface of a fixed *Aristolochia esperanzae* leaf and its corresponding pNBF8 textured film. Tilted images (a, b, e, and f) were taken at 45° with respect to the surface parallel.

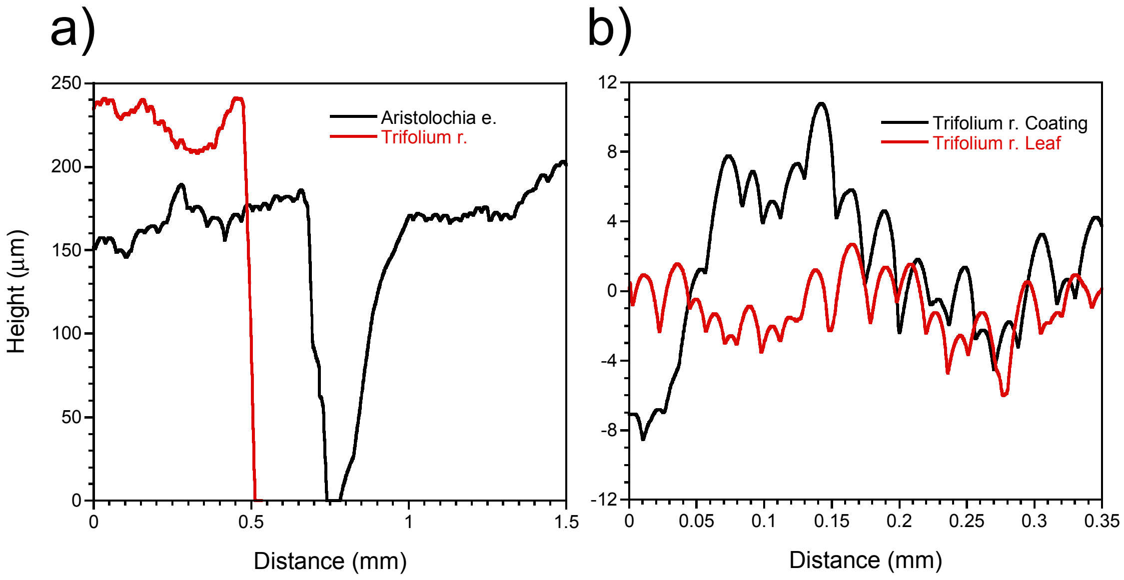

Figure 7.3. Profilometry line profiles of a) pNBF8 coatings reproducing the surface topography of fixed *Aristolochia esperanzae* and *Trifolium repens* leaves, b) *Trifolium repens* fixed leaf and pNBF8 coating. In a), after curing, the composite molds were cut smaller than their original size in order to discard the corresponding thickness of the leaf. Unlike the *Aristolochia esperanzae* line profile in a), which was measured in the middle of the coating, the line profile of the coating reproducing the *Trifolium repens* leaf in a) was measured at the edge of the film because the coating was too thick for the stylus tip of the profilometer to reach the bottom of the sample.

Figure 7.3a shows the line profiles obtained by profilometry of pNBF8 coatings formed by µMSIP. The figure reveals that the polymer coatings exhibiting the reproduced surface structures of the *Aristolochia esperanzae* and *Trifolium repens* leaves rest atop an underlying film ~150 to 180 and 210 to 240 µm thick, respectively. Such a remarkably thick coating does not correspond to the thickness of the leaves, as this thickness was eliminated by cutting the composite molds smaller than their original size. Instead, it corresponds to excess monomer added to the mold. In principle, this thickness is adjustable by controlling the amount of initial monomer in the mold. Measurements obtained from the line profile indicate that the films reproducing the surface topography of the *Aristolochia esperanzae* and *Trifolium repens* leaves exhibit in some parts of the surface, peak-to-valley heights as large as ~40 µm, and that the height of single features varies from 3 to 6 µm for each leaf. Figure 7.3b shows zoomed-in line profiles for the Trifolium repens leaf and a pNBF8 coating. Profilometry measurements show that the width and height of the epidermal cells on the surface of the leaf are 19.2 ± 6.2 and 2.7 ± 1 μm, respectively; those of the polymer features on the coating are 19.4 ± 5.6 and 2.9 ± 1 μm, respectively. The values for the width are in good agreement with those obtained from image analysis of Figure 7.1.

Table 7.1. Wetting properties of *Trifolium repens*, *Aristolochia esperanzae*, and their corresponding pNBF8 films.

	Leaf		Coating	
Sample	θ_A	θ_R	θ_A	θ_R
Trifolium repens	162° ± 3°	157° ± 3°	158° ± 2°	151° ± 4°
Aristolochia esperanzae	156° ± 5°	145° ± 5°	152° ± 2°	150° ± 2°

Table 7.1 summarizes the advancing (θ_A) and receding (θ_R) water contact angles for the *Trifolium repens* and *Aristolochia ezperanzae* leaves, and those of their corresponding polymer coatings. The *Trifolium repens* leaf exhibits higher advancing and receding contact angles than those exhibited by the *Aristolochia ezperanzae* leaf. The *Trifolium repen* meets the requirements to be considered as superhydrophobic, i.e., $\theta_A > 150°$ and hysteresis < 10°, whereas the *Aristolochia ezperanzae* leaf falls short of this definition (hysteresis = 11°), despite having a high θ_A angle. The polymer coatings formed by μMSIP also exhibit a low wettability towards water, as evidenced by the high θ_A and θ_R water contact angles that are, within the measured errors, the same as those of the leaf. Despite some differences between the leaf and coating (most notably, the absence of hair-like surface features for the reproduced coating of *Aristolochia esperanzae* and observable defects in the coating for *Trifolium repens*), these results indicate that μMSIP enables the preparation of surface-bound polymer coatings exhibiting sufficient microscopic roughness to achieve the superhydrophobic wetting state. This level of performance may be explained from a chemical composition perspective: the fluorinated nature of the coating, with its

lower surface energy than a hydrocarbon, compensates for the lack of perfection in the reproduction.

Figure 7.4. Photograph of a dime (left), an *Aristolochia ezperanzae* leaf (middle), and corresponding pNBF8 coating of the leaf (right).

Figure 7.4 shows a macroscale image of a dime, shown as a reference for size, and an *Aristolochia ezperanzae* leaf along with its corresponding replicating pNBF8 coating. Remarkably, μMSIP enables the resulting polymer coating to capture not only the microscale morphology of the leaf, but also the large-scale topographical details, e.g., the veins, as evidence by the lines running across the surface of the coating.

Conclusions

In this Chapter, I have demonstrated that μMSIP is a versatile and fast route to fabricate textured coatings that reproduce the surface topography of superhydrophobic leaves onto solid supports. Overall, the resulting surface morphology of the polymer coatings is in good agreement with that of the reproduced leaves as evidenced by SEM and corresponding quantitative image analysis. Profilometry measurements showed that the polymer micromorphological relief rests upon a thick, robust coating whose thickness may be controlled, in principle, by the amount of monomer added to the mold. Contact angle measurements on the resulting pNBF8 coatings confirmed the achievement of a superhydrophobic wetting behavior and the influence of a combination of chemical composition and micro-roughness on wettability (*Aristolochia ezperanzae* case). This proof-of-concept work opens the door to the possibility of exploring and reproducing a great number of superhydrophobic leaves and other biologically optimized surfaces available in nature.

References

(1) Thickett, S. C.; Neto, C.; Harris, A. T. Biomimetic Surface Coatings for Atmospheric Water Capture Prepared by Dewetting of Polymer Films. *Advanced Materials* **2011,** 23, 3718 - 3722.

(2) Zhiwu, H.; Junqiu, Z.; Chao, G.; Li, W.; Ren, L. Erosion Resistance of Bionic Functional Surfaces Inspired from Desert Scorpions. *Langmuir* **2011,** 28, 2914-2921.

(3) Noone, C. J.; Torrilhon, M.; Mitsos, A. Heliostat Field Optimization: A New Computationally Efficient Model and Biomimetic Layout. *Solar Energy* **2012,** 86, 792-803.

(4) Wong, T.-S.; Kang, S. H.; Tang, S. K. Y.; Smythe, E. J.; Hatton, B. D.; Grinthal, A.; Aizenberg, J. Bioinspired Self-Repairing Slippery Surfaces with Pressure-Stable Omniphobicity. *Nature* **2011,** 477, 443-447.

(5) Bhushan, B. Bioinspired Structured Surfaces. *Langmuir* **2012,** 28, 1698-1714.

(6) Furstner, R.; Barthlott, W.; Neinhuis, C.; Walzel, P. Wetting and Self-Cleaning Properties of Artificial Superhydrophobic Surfaces. *Langmuir* **2005,** 21, 956-961.

(7) Sun, M. H.; Luo, C. X.; Xu, L. P.; Ji, H.; Qi, O. Y.; Yu, D. P.; Chen, Y. Artificial Lotus Leaf by Nanocasting. *Langmuir* **2005,** 21, 8978-8981.

(8) Roach, P.; Shirtcliffe, N. J.; Newton, M. I. Progess in Superhydrophobic Surface Development. *Soft Matter* **2008,** 4, 224-240.

(9) Lee, S.-M.; Lee, H. S.; Kim, D. S.; Kwon, T. H. Fabrication of Hydrophobic Films Replicated from Plant Leaves in Nature. *Surface and Coatings Technology* **2006,** 201, 553-559.

(10) Lee, Y.; Park, S. H.; Kim, K. B.; Lee, J. K. Fabrication of Hierarchical Structures on a Polymer Surface to Mimic Natural Superhydrophobic Surfaces. *Advanced Materials* **2007,** 19, 2330-2335.

(11) Hsu, S.-H.; Sigmund, W. M. Artificial Hairy Surfaces with a Nearly Perfect Hydrophobic Response. *Langmuir* **2010,** 26, 1504-1506.

(12) Faulkner, C. J.; Fischer, R. E.; Jennings, G. K. Surface-Initiated Polymerization of 5-(Perfluoro-n-alkyl)norbornenes from Gold Substrates. *Macromolecules* **2010,** 43, 1203-1209.

(13) Jennings, G. K.; Brantley, E. L. Physicochemical Properties of Surface-Initiated Polymer Films in the Modification and Processing of Materials. *Adv. Mater.* **2004,** 16, 1983-1994.

(14) Wu, D.; Wang, J.-N.; Wu, S.-Z.; Chen, Q.-D.; Zhao, S.; Zhang, H.; Sun, H.-B.; Jiang, L. Three-Level Biomimetic Rice-Leaf Surfaces with Controllable Anisotropic Sliding. *Adv. Funct. Mater.* **2011,** 21, 2927 - 2932.

(15) Wu, Z.; Xu, Q.; Wang, J.; Ma, J. Preparation of Large Area Double-walled Carbon Nanotube Macro-films with Self-cleaning Properties. *Journal of Materials Science & Technology* **2009,** 26, 20-26.

(16) He, M.; Wang, J.; Li, H.; Jin, X.; Wang, J.; Liu, B.; Song, Y. Super-Hydrophobic Film Retards Frost Formation. *Soft Matter* **2010,** 6, 2396-2399.

(17) Rothstein, J. P. Slip on Superhydrophobic Surfaces. *Annual Review of Fluid Mechanics* **2010,** 42, 89-109.

(18) Barthlott, W.; Schimmel, T.; Wiersch, S.; Koch, K.; Brede, M.; Barczewski, M.; Walheim, S.; Weis, A.; Kaltenmaier, A.; Leder, A.; Bohn, H. F. The Salvinia Paradox: Superhydrophobic Surfaces with Hydrophilic Pins for Air Retention Under Water. *Advanced Materials* **2010,** 22, 2325-2328.

(19) Neinhuis, C.; Barthlott, W. Characterization and Distribution of Water-Repellent, Self-Cleaning Plant Surfaces. *Ann. Bot.* **1997,** 79, 667-677.

CHAPTER VIII

CONCLUSIONS AND FUTURE WORK

Conclusions

The results presented in this thesis demonstrate that the surface-initiated ring-opening polymerization (SI-ROMP) of 5-(perfluoro-n-alkyl)norbornenes is a versatile route to produce novel materials and biomimetic coatings. This work capitalizes on the advantages and characteristics of SI-ROMP and on the polymerization kinetics of this particular class of partially fluorinated monomers to explore applications that have remained mostly untapped by other techniques for surface-initiated polymerization.

Results in Chapter IV demonstrated the first application of SI-ROMP to prepare uniquely layered membranes in which fluorocarbon-containing polymer films (pNBF6) can be grown within, throughout, and between nanoporous architectures. The regulation of the polymerization time and the sulfonation levels of the polymer backbone influence the wettability and transport of simple ions through the membrane, respectively. Accordingly, longer polymerization times result in composite fluorocarbon membranes that exhibit resistance against the transport of ions on the order of 1×10^7 Ω•cm^2, as measured by electrochemical impedance spectroscopy (EIS). The assessment of the surface properties of the membranes with water and hexadecane contact angle measurements show that their surface is both highly hydrophobic and oleophobic, consistent with the low critical surface energy exhibited by pNBF6 films whose surface is dominated by perfluoromethyl groups. EIS measurements also show that ion transport through the composite membrane is substantially enhanced after sulfonation. Moreover, the fluorinated character of the pNBF6 film renders the membrane more selective toward ions with similar chemical properties. A remarkable finding is that when the pNBF6 film is grown between two chemically bound nanoporous substrates, its growth resembles the motion of a forklift to separate the substrates at an average velocity of ~2 nm/s. This ability has the potential to be exploited for the separation of surfaces to targeted nanoscale dimensions.

In Chapter V, I introduced a macroinitiation-based approach to produce protective, partially fluorinated coatings, derived from 5-(perfluoro-n-alkyl)norbornenes, with enhanced thicknesses and barrier properties. In this section, I demonstrated that a PHEMA-based macroinititiation process enhances the polymerization rate and promotes greater film thicknesses. Derivatization of the hydroxyl functional groups present in PHEMA via post-polymerization reactions enables the immobilization of a higher number of initiator molecules, e.g., at least 30-times more than a monolayer initiation. The length of the fluorocarbon side chain, monomer concentration, and temperature have marked effects on the polymerization kinetics and thickness of the resulting pNBFn films. In general, longer side chains, higher concentrations, and higher temperatures promote faster polymerization rates and thicker films. The macroinitiation approach herein used enables fine tuning of the thickness and wetting properties of pNBFn films by adjusting any of the variables described above. Results show that the macroinitiated polymerizations performed at higher temperatures produce dense, rough coatings that are highly hydrophobic (advancing water contact angle = 165°) and oleophobic (hexadecane contact angle = 94°). Remarkably, this macroinitiation approach yields thicknesses from 4 – 12 μm in as little as 15 min. In addition, EIS characterization reveals that the films exhibit exceptional barrier properties against ion transport, e.g., resistance > 10 $G\Omega \cdot cm^2$ and capacitance = 2×10^{-10} $F \cdot cm^{-2}$. In general, the exceptional polymerization kinetics and resistance against ion transport exhibited by these macroinitiated pNBFn films are among the fastest/highest ever reported for SIP films.

In Chapter VI, I reported an innovative and versatile process termed μMSIP to provide surface-bound, partially fluorinated polymer films, with a homogeneous array of microscale surface features by combining soft lithography and surface-initiated polymerization techniques. In this Chapter, I demonstrated that μMSIP enables the formation of polymer films exhibiting either high-relief (pyramids) or recessed topographies (inverted pyramids). μMSIP is flexible and versatile in the sense that multiple process variables, e.g., initiation approach, polymerization time, temperature, or addition of initiator to the mold, may be manipulated to tune the heights (monomer conversion) of the reproduced features from the full height of the master down to ~10% of that height. SEM images show that the resulting films are uniform in quality and exhibit homogeneous surface structures across large areas. AFM measurements reveal a high level of uniformity in terms of feature footprint and height. Furthermore, μMSIP facilitates the preparation of generational textured films.

In Chapter VII, I extended μMSIP for the fabrication of polymer coatings that reproduce the surface topography of natures's superhydrophic surfaces onto solid supports. Image analysis of SEM images shows that the dimensions and shapes of the surface features of the final polymer coating are quantitatively similar to those of the reproduced leaves. Profilometry reveals that the textured surface of the coating sits atop a thick, robust polymer layer with step heights varying from 150 to 240 μm, and whose height may be tuned by the amount of monomer added to the mold. The high contact angle values (>150°) and low hysteresis (<10°) exhibited by the coatings evidence that μMSIP enables the preparation of coatings exhibiting sufficient microscopic roughness to achieve the superhydrophobic wetting state.

Future Work

The results demonstrated in this thesis: (1) the fabrication and characterization of novel partially fluorinated/inorganic composites by employing SI-ROMP within nanoporous architectures to create membranes with tunable wettability and ion transport; (2) the amplification of the SIP of partially fluorinated polymer films to fabricate specialty coatings that yield thicknesses from 4 – 12 µm in as little as 15 min of polymerization and exhibit resistance against ion transport in excess of 10 $G\Omega\bullet cm^2$; (3) the fabrication of microscale surface features with height modulation and (4) the reproduction of the complex surface topographies of superhydrophobic natural surfaces onto solid supports; open new research avenues that may lead to interesting outcomes. Below are suggestions of topics that could be addressed in the near term and examples of applications (long term) that may further benefit from SI-ROMP and to which µMSIP may be extended.

Short Term

In general, the family of partially fluorinated monomers (pNBFn) studied in this thesis exhibits fast polymerization kinetics. Results in Chapter V show that the longer the fluorocarbon side chain of the monomer, the faster its polymerization. However, the exact mechanism of how a longer side chain promotes faster kinetics is not clear and is worthy of further investigation. Therefore, performing a mechanistic study, coupled with molecular simulations, of the polymerization of these monomers should help elucidate such an effect. SEM characterization of the films grown in Chapter V reveals that the surface of these films is dominated by spherical- and hemisphere-like structures, which in some cases, may exhibit diameters as large as 25 µm. This sort of feature does not grow when the monomer is polymerized in pure form (Chapters VI and VII), suggesting that the solvent (dichloromethane) may have an effect on how these monomers react to form such structures. Exploring the possible formation of micelles or some other type of larger aggregates in the monomer solution and their interaction with the initiator-modified substrate may help explain such a phenomenon.

In connection with Chapters VI and VII, one could study the polymerization kinetics of other norbornenyl-derived or cyclic olefin monomers, as was done with the NBFn family in Chapter V, to explore the feasibility of using them in μMSIP, and therefore, provide textured polymer films with a wider range on chemical compositions. The area of the h-PDMS molds used in Chapters VI and VII was ~1 cm^2. Extending μMSIP to larger areas is a subsequent step that should be followed in order to improve the technique. In the case of reproducing large structures, such as those found on the natural surfaces tested herein, the deposition of the initiator species and the monomer into a mold exhibiting a larger area could become challenging if done manually, given the fast kinetics of the polymerization. Therefore, one could investigate the possibility of using a spray-assisted deposition method that would allow covering larger areas in shorter times. In Chapter VII, SEM characterization of the *Aristolochia esperanzae* leaf showed that the surface of the leaf is dominated by both micro- and nanoscale features. Although μMSIP was able to capture the microscale relief of the leaf, as revealed by SEM characterization of the final polymer coating, the nanoscale topography was almost absent. Overall, the epicuticular waxes that comprise the nanoscale topography of leaves are fragile and can be easily damaged by external factors.[1] Therefore, an inherent extension of this work would be to improve the stability of the epicuticular waxes, especially upon detachment from the composite mold, such that these do not become embedded in the mold. To this end, one could explore the possibility of adding an extra layer of fluorocarbon-containing silane on top of the existing tetraethoxysilane. An exciting opportunity to test the versatility of μMSIP would be to reproduce the topography of leaves exhibiting anisotropic surfaces, such as that the rice leaf.[2] This would allow the fabrication of textured surfaces with directional wetting and could have a great impact on applications such as fluidic control and water-directional transportation.[2]

Long Term

SI-ROMP of Ionic Liquids for Membrane Applications

The performance and stability of composite materials in gas separation applications dictate the success or viability of membranes in an industrial setting.[3] Accordingly, researchers are constantly searching for new materials to improve the flux and selectivity of membranes. Recently, room-temperature ionic liquids (RTILs) have shown promising results as constituents of composite membranes for the separation of carbon dioxide (CO_2) from light gases such as nitrogen (N_2) and methane (CH_4).[4] RTILs, namely imidazolium-based ones, exhibit physicochemical properties that make them ideal candidates to be used in membrane-based gas separations. These properties include ultralow vapor pressure, low melting temperatures, thermal stability, and "green" character.[5] These materials have been mainly used in a membrane configuration known as supported ionic liquid membrane, in which the RTIL is "infused" in the porous structure of a polymeric membrane via a vacuum-assisted procedure.[6] The use of such composite membranes is limited to a transmembrane pressure differential of 1 – 2 atm.[3] Higher operation pressures, as those found in large-scale industrial gas separations, would "blowout" the RTIL, therefore, undermining the performance of the composite membrane.[3] In Chapter IV, I demonstrated that SI-ROMP could be used to grow surface-bound pNBF6 films within and throughout nanoporous architectures. Consequently, one could examine the possibility of synthesizing norbornenyl-based ionic liquids that could undergo SI-ROMP. This approach may provide RTIL-based composite membranes with the mechanical integrity and stability required for industrial gas separations. Furthermore, one could investigate the effect of different RTIL composition or polymer architecture on the degree of permeability and selectivity.

Extend μMSIP to the Fabrication of Superoleophobic Films

In recent years, an increasing amount of research has focused on creating not only superhydrophobic but also superoleophobic surfaces.[7-11] Investigations on this topic have shown that surfaces exhibiting a combination of low critical surface tension and topographical structures with re-entrant surface curvature may resist wetting of liquids with low surfaces tension, such as alkanes (octane or decane).[7] Realization of such surfaces could have a great impact on applications such as stain-free textiles[9,10] and chemical shielding.[11] In this thesis, I have shown that one can fine-tune the growth of partially fluorinated monomers to produce films with critical surface tension as low as 9 mN/m[12] (Chapter V), and as an extension of the reproduction process described in Chapters VI and VII, one could explore the possibility of creating surface-bound superoleophobic films by using μMSIP to reproduce the surface topography of substrates exhibiting surface features with re-entrant surface curvature. For example, one could deposit a monolayer or multilayer of polystyrene spheres to provide the desired re-entrant curvature onto a substrate and use soft lithography to create an elastomeric mold with recessed round features that can be subsequently used in a μMSIP process. The use of polystyrene spheres is advantageous because these are readily available and are produced in different sizes. This approach would enable fundamental studies on how different geometric parameters, such as height and diameter of the features and the separation distance among them, may affect the wetting of oils on these surfaces.

References

(1) Neinhuis, C.; Barthlott, W. Characterization and Distribution of Water-Repellent, Self-Cleaning Plant Surfaces. *Ann. Bot.* **1997,** 79, 667-677.

(2) Wu, D.; Wang, J.-N.; Wu, S.-Z.; Chen, Q.-D.; Zhao, S.; Zhang, H.; Sun, H.-B.; Jiang, L. Three-Level Biomimetic Rice-Leaf Surfaces with Controllable Anisotropic Sliding. *Adv. Funct. Mater.* **2011,** 21, 2927 - 2932.

(3) Carlisle, T. K.; Wiesenauer, E. F.; Nicodemus, G. D.; Gin, D. L.; Noble, R. D. Ideal CO2/Light Gas Separation Performance of Poly(vinylimidazolium) Membranes and Poly(vinylimidazolium)-Ionic Liquid Composite Films. *Industrial & Engineering Chemistry Research* **2012,** 52, 1023-1032.

(4) Bara, J. E.; Lessmann, S.; Gabriel, C. J.; Hatakeyama, E. S.; Noble, R. D.; Gin, D. L. Synthesis and Performance of Polymerizable Room-Temperature Ionic Liquids as Gas Separation Membranes. *Industrial & Engineering Chemistry Research* **2007,** 46, 5397-5404.

(5) Weingärtner, H. Understanding Ionic Liquids at the Molecular Level: Facts, Problems, and Controversies. *Angewandte Chemie International Edition* **2008,** 47, 654 - 670.

(6) Neves, L. A.; Crespo, J. G.; Coelhoso, I. M. Gas Permeation Studies in Supported Ionic Liquid Membranes. *Journal of Membrane Science* **2010,** 357, 160-170.

(7) Tuteja, A.; Choi, W.; Ma, M.; Mabry, J. M.; Mazzella, S. A.; Rutledge, G. C.; McKinley, G. H.; Cohen, R. E. Designing Superoleophobic Surfaces. *Science* **2007,** 318, 1618-1622.

(8) Tuteja, A.; Choi, W.; Mabry, J. M.; McKinley, G. H.; Cohen, R. E. Robust Omniphobic Surfaces. *Proceedings of the National Academy of Sciences of the United States of America* **2008,** 105, 18200-18205.

(9) Leng, B.; Shao, Z.; de With, G.; Ming, W. Superoleophobic Cotton Textiles. *Langmuir* **2009,** 25, 2456-2460.

(10) Artus, G. R. J.; Zimmermann, J.; Reifler, F. A.; Brewer, S. A.; Seeger, S. A Superoleophobic Textile Repellent Towards Impacting Drops of Alkanes. *Applied Surface Science* **2012,** 258, 3835-3840.

(11) Pan, S.; Kota, A. K.; Mabry, J. M.; Tuteja, A. Superomniphobic Surfaces for Effective Chemical Shielding. *Journal of the American Chemical Society* **2013,** 135, 578-581.

(12) Faulkner, C. J.; Fischer, R. E.; Jennings, G. K. Surface-Initiated Polymerization of 5-(Perfluoro-n-alkyl)norbornenes from Gold Substrates. *Macromolecules* **2010,** 43, 1203-1209.

APPENDIX A

SUPPLEMENTARY INFORMATION FOR CHAPTER V

X-ray Photoelectron Spectroscopy (XPS) Data

Table A.1 compares the calculated atomic composition and percentages of C 1s bonding states to those obtained experimentally. The estimated values for the acid halide attachment, summarized in Table 5.2, represent the potential number of bonding sites for the Ru-based initiator. Exposure of the PHEMA films to the di-acid halide solution may lead to three results, e.g., unreacted hydroxyl groups, and hydroxyl groups forming either one or two ester bonds. To determine the calculated values shown in Table A.1, a composition balance and a fit of the experimental XPS data, namely, the C-C percentage and Cl atomic composition, of each possible outcome was performed. Calculated and experimental values are in good agreement.

Table A.1. Comparison of theoretical and experimentally determined carbon bonding state percentages and atomic composition.

Sample: PHEMA, NBDAC	C–C	C–O	O=C–O	At% C	At% O	At% Cl
Calculation	56.8	25.2	18.0	69.5	30.1	0.4
Experimental	56.8	24.7	18.5	68.3	31.3	0.4

Initiator Footprint

I estimated the projected molecular area of the initiator using the crystallographic data reported by Love et al. and Matlab software.[1] Results from our approximation indicate that the projected molecular area of the Ru catalyst, not including the tricyclohexylphosphine ligand nor the phenyl ring, is ~ 83 Å^2•molecule^{-1}, which is comparable to the molecular areas reported for other Ru containing complexes.[2]

Wetting Properties

Table A.2. Wetting properties of the pNBFn films prepared in a 0.2 and 1 M monomer solutions, after 15 min of polymerization at 21 °C

		Monolayer		Macroinitiator	
Concentration (M)	θ_A (deg)	pNBF6	pNBF8	pNBF6	pNBF8
0.2	Water	123 ± 2	127 ± 1	130 ± 2	127 ± 1
	HD	73 ± 1	79 ± 1	77 ± 2	78 ± 2
1	Water	132 ± 1	131 ± 1	143 ± 4	146 ± 2
	HD	79 ± 1	83 ± 2	84 ± 2	85 ± 5

The surface energy of the gold substrates changes as it undergoes each modification step in the polymerization process, as evidenced by the change in the advancing water contact angle. Clean, bare gold samples, under ambient conditions, exhibit average advancing water contact angles of ~ 60°.[3] The formation of the ATRP-initiator SAM onto the surface increases the water θ_A to ~ 75°, which is in fair agreement with that reported for a bromine-terminated monolayer.[4] Upon growth of PHEMA, the surface energy moderately increases, as evidenced by a reduction in the water θ_A, e.g., ~ 66°. This change in surface energy may be attributed to the presence of the polar hydroxyl groups in PHEMA. The increase in the water θ_A (~ 81°) after the acylation process is consistent with the presence of hydrocarbon molecules (norbornenyl groups) in the outermost surface of the PHEMA films. Generally, smooth semifluorinated films, in which the outermost portion of their surface is dominated by $-CF_3$ groups, exhibit θ_A (water) > 113° and θ_A

(HD) > 75°.[5] After polymerization, the wetting properties of the modified gold substrates changed dramatically, as evidenced by a surge in both water and HD advancing contact angles, from much lower values for the monolayer (water = 22°, HD < 15°) and macroinitiator (water = 66°, HD < 15°).

Figure A.1 shows the effects of monomer concentration and macroinitiation on the time-dependence of pNBF8 film thickness, as measured by profilometry. Table A.3 summarizes the film growth and termination rate constants for different NBF8 concentrations.

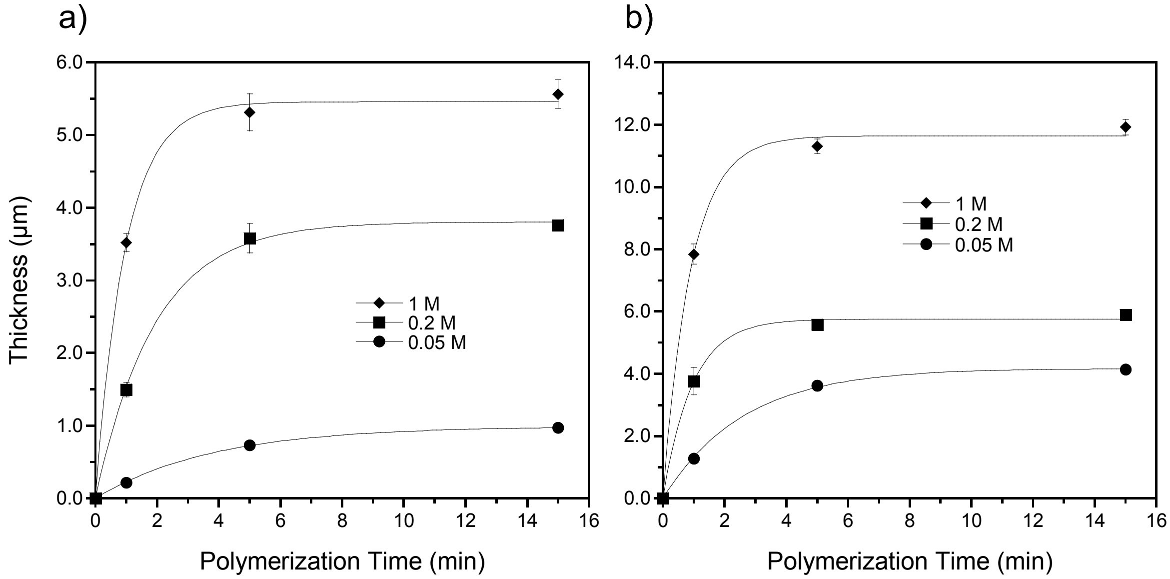

Figure A.1. Monomer concentration effects on film thickness for a) a monolayer initiation and b) macroinitiation. The data points represent thickness measurements for pNBF8 films grown in 0.05, 0.2, and 1 M monomer solutions. For the macroinitiator case, an average thickness for PHEMA of 280 nm was subtracted from the measured thickness. Solid curves represent fits of the data using equation 3.

Table A.3. Film growth and termination rate constants for films prepared from NBF8 at three different concentrations. Values are presented along with their standard errors.

	Monolayer		Macroinitiator	
Concent. (M)	K (m•s^{-1})	k_t (s^{-1})	K (m•s^{-1})	k_t (s^{-1})
0.05	$2.7 \times 10^{-7} \pm 6.6 \times 10^{-9}$	$0.0043 \pm 1.3 \times 10^{-4}$	$1.7 \times 10^{-6} \pm 7.1 \times 10^{-8}$	$0.0064 \pm 3.2 \times 10^{-4}$
0.2	$5.2 \times 10^{-7} \pm 2.5 \times 10^{-8}$	$0.0086 \pm 4.7 \times 10^{-4}$	$1.6 \times 10^{-6} \pm 1.1 \times 10^{-7}$	$0.0176 \pm 1.3 \times 10^{-3}$
1	$2.9 \times 10^{-7} \pm 1.7 \times 10^{-8}$	$0.0171 \pm 1.0 \times 10^{-3}$	$6.8 \times 10^{-7} \pm 4.7 \times 10^{-8}$	$0.0185 \pm 1.3 \times 10^{-3}$

References

(1) Love, J. A.; Sanford, M. S.; Day, M. W.; Grubbs, R. H. Synthesis, Structure, and Activity of Enhanced Initiators for Olefin Metathesis. *J. Am. Chem. Soc.* **2003,** 125, 10103-10109.

(2) Mingotaud, A.-F.; Krämer, M.; Mingotaud, C. Catalytic Surfactants for Ring-Opening Metathesis Polymerization and Ring-Closing Metathesis in Non-Degassed Micellar Solutions. *Journal of Molecular Catalysis A: Chemical* **2007,** 263, 39-47.

(3) Bain, C. D.; Troughton, E. B.; Tao, Y. T.; Evall, J.; Whitesides, G. M.; Nuzzo, R. G. Formation of Monolayer Films by the Spontaneous Assembly of Organic Thiols from Solution onto Gold. *J. Am. Chem. Soc.* **1989,** 111, 321-335.

(4) Laibinis, P. E.; Palmer, B. J.; Lee, S. W.; Jennings, G. K. . In *Thin Films*; Academic Press: New York, **1998**; Vol. 24.

(5) Fukushima, H.; Seki, S.; Nishikawa, T.; Takiguchi, H.; Tamada, K.; Abe, K.; Colorado, R.; Graupe, M.; Shmakova, O. E.; Lee, T. R. Microstructure, Wettability, and Thermal Stability of Semifluorinated Self-Assembled Monolayers (SAMs) on Gold. *J. Phys. Chem. B* **2000,** 104, 7417-7423.

APPENDIX B

COMPLEMENTARY INFORMATION FOR CHAPTER VI

Atomic Force Microscopy (AFM) Measurements

Table B.1. Summary of the atomic force microscopy characterization results for the structures shown in Figures 6.2e and 6.4c.

	DFEAs			Klarite®		
	Master	Mold	Film	Master	Mold	Film
Height (μm)	1.86 ± 0.03	1.73 ± 0.02	1.05 ± 0.02	0.99 ± 0.01	1.09 ± 0.04	0.69 ± 0.01
Width (μm)	4.05 ± 0.09	4.06 ± 0.13	4.16 ± 0.14	1.80 ± 0.02	1.72 ± 0.02	1.94 ± 0.03
Pitch[a] (μm)	4.57 ± 0.09	4.45 ± 0.08	4.66 ± 0.12	2.30 ± 0.03	2.13 ± 0.03	2.32 ± 0.02

[a] Pitch refers to the distance between peaks.